Příloha: Autorovy odborné publikace

Tato příloha je součásti diplomové práce Bc. Lukáše Petery z roku 2020 s názvem:

Důsledky éry velkého bombardováni pro chemickou a prebiotickou evoluci raného Marsu a Země

V této příloze jsou uvedeny autorovy odborné publikace.

Tato příloha není součástí tištěné práce a je dostupná pouze v elektronické verzi.

Tato příloha byla nahrána do systémového rozhraní SIS.

Seznam přiložených publikací:

M. Ferus *et al.*, "Elemental composition, mineralogy and orbital parameters of the Porangaba meteorite," *Icarus*, vol. 341, p. 113670, 2020.

A. Pastorek *et al.*, "Prebiotic synthesis at impact craters: the role of Fe-clays and iron meteorites," *Chem. Commun.*, vol. 55, no. 71, pp. 10563–10566, 2019.

M. Ferus *et al.*, "Main spectral features of meteors studied using a terawatt-class high-power laser," *Astron. Astrophys.*, vol. 630, p. A127, 2019.

M. Ferus *et al.*, "Prebiotic synthesis initiated in formaldehyde by laser plasma simulating high-velocity impacts," *Astron. Astrophys.*, vol. 626, p. A52, 2019.

Icarus 341 (2020) 113670

Contents lists available at ScienceDirect

Icarus

journal homepage: www.elsevier.com/locate/icarus

Elemental composition, mineralogy and orbital parameters of the Porangaba meteorite

Martin Ferus [a,1], Lukáš Petera [a,b,1], Jakub Koukal [a,c,1], Libor Lenža [a,c,1], Barbora Drtinová [d], Jakub Haloda [e,f], Dalibor Matýsek [g], Adam Pastorek [a,d], Vojtěch Laitl [a,m], Renato Cassio Poltronieri [i], Marcelo Wagner Domingues [h], Gabriel Gonçalves [h], Rodrigo del Olmo Sato [i], Antonín Knížek [a,l], Petr Kubelík [a,j], Anna Křivková [a,d], Jiří Srba [c], Carlos Augusto di Pietro [h], Milan Bouša [a], Tomáš Vaculovič [k], Svatopluk Civiš [a,*]

[a] J. Heyrovský Institute of Physical Chemistry, Czech Academy of Sciences, Dolejškova 3, CZ18223 Prague 8, Czech Republic
[b] Charles University in Prague, Faculty of Science, Hlavova 2030/8, CZ12843 Prague 2, Czech Republic
[c] Valašské Meziříčí Observatory, Vsetínská 78, CZ75701 Valašské Meziříčí, Czech Republic.
[d] Faculty of Nuclear Sciences and Physical Engineering, Czech Technical University in Prague, Břehová 78/7, 115 19 Prague 1, Czech Republic
[e] Czech Geological Survey, Klárov 131/3, CZ 118 21 Prague 1, Czech Republic
[f] Oxford Instruments Nanotechnology Tools Ltd., Velvarská 1649/13, CZ16000, Prague 6, Czech Republic
[g] VŠB-Technical University of Ostrava, Department of Geological Engineering, 17. listopadu, 15/2172, CZ708 33 Ostrava - Poruba, Czech Republic
[h] BRAMON, BRAzilian Meteor Observation Network, Brazil
[i] Sociedade Brasileira de Meteorítica, R. Felipe Schmidt 735, Andar 4 Apt 401, Centro, Florianopolis, SC, CEP 88010-002, Brazil
[j] Institute of Physics, Czech Academy of Sciences, Department of Radiation and Chemical, Physics, Na Slovance 2, CZ18221 Prague 8, Czech Republic
[k] Masaryk University, Faculty of Science, Department of Chemistry, Kamenice 5, 62500 Brno, Czech Republic
[l] Charles University in Prague, Faculty of Science, Department of Physical and Macromolecular Chemistry, Hlavova 2030/8, CZ12843 Prague 2, Czech Republic
[m] University of Chemistry and Technology Prague, Faculty of Chemical Engineering B, Technická 5, CZ16628 Prague 6 Dejvice, Czech Republic

ARTICLE INFO

Keywords:
LIBS
EDS
Porangaba

ABSTRACT

The main objective of this study is to provide data on the bulk elemental composition, mineralogy and the possible origin of the Porangaba meteorite, whose fall was observed at 17:35 UT on 9 January 2015 on several sites of the state of São Paulo in Brazil. The surface of the meteorite was mapped by Scanning Electron Microscopy (SEM) and optical microscopy. The mineralogy and the bulk elemental composition of the meteorite were studied using Energy-Dispersive and Wavelength-Dispersive X-ray Spectroscopy (EDS/WDS) together with Electron Back Scatter Diffraction (EBSD). The bulk elemental composition was also independently analysed by Atomic Absorption Spectrometry (AAS), Inductively Coupled Plasma Mass Spectrometry (ICP-MS), Laser Ablation ICP MS (LA ICP-MS) and Calibration-Free Laser-Induced Breakdown Spectroscopy (CF-LIBS). Based on the available visual camera records of the Porangaba meteorite fall, its orbit was tentatively calculated, and possible candidates for the source bodies in the Solar system were proposed. We also present a laboratory simulation of a Porangaba-like (L4 Ordinary Chondrite) meteor emission spectra. These can be used as benchmark spectra for the identification of meteor rock types through their comparison with meteor spectra recorded by high-speed video-cameras equipped with simple grating spectrographs.

1. Introduction

Complex analyses of meteors and meteorites play a key role in understanding the geology and history of rocky bodies, such as asteroids, comets, planets and moons, in the Solar system and beyond (Afanasiev et al., 2007; Siraj and Loeb, 2019). Physical and chemical characterization of meteorites and meteors together with the knowledge of their trajectories or their origin in the Solar system provides information about the formation and subsequent evolution of the source body and ultimately about the history of Solar system itself.

* Corresponding author.
E-mail address: svatopluk.civis@jh-inst.cas.cz (S. Civiš).
[1] Contribution of all the first four authors is equal.

https://doi.org/10.1016/j.icarus.2020.113670
Received 5 September 2018; Received in revised form 17 January 2020; Accepted 27 January 2020
Available online 28 January 2020

The most detailed and reliable data are obtained by direct analysis of the chemical composition, mineralogy and petrology of meteorites. These data are especially valuable if the meteoroid trajectory during descent is recorded as well, because then, the meteoroid's source region can be determined. This is actually one of the major goals of current planetary science research (Drouard et al., 2018). However, as much as 80% of the observed meteoroid falls are not paired with a corresponding meteorite found on the Earth (Drouard et al., 2018). There are over 1000 known cases of observed falls, but the precise orbital trajectory has been calculated only for about 30 of them (Gounelle et al., 2006), "List of meteorites with a complete 'lineage'", 2019). The first meteorite with known orbital parameters and mineralogy was meteorite Příbram (7th of April 1959, near Příbram, Czech Republic (Ceplecha, 1961)). Other known cases are for instance the Košice meteorite, Slovakia (Ozdin et al., 2015), (Horňáčková et al., 2014), the famous reconstruction of the Orgueil meteorite trajectory from historical records (Gounelle et al., 2006), the Lost City meteorite in Oklahoma, USA (McCrosky et al., 1971; Gritsevich, 2008), Innisfree in Canada, Neuschwanstein in Germany, Peekskill in New York state, USA (Brown et al., 1994), Morávka in Czech Republic (Borovicka et al., 2003), Park Forest in Illinois, USA, (Brown et al., 2004) and Chelyabinsk in Russia (Borovička et al., 2013).

The limiting factors of the survival of meteoroids during their descent to the Earth's surface can be calculated (see e.g. (Collins et al., 2005)). Given the nature of bodies entering the atmosphere, most meteoroids do not survive and it is therefore impossible to study their samples in laboratory. A potentially applicable method of overcoming this problem is classification based on the spectroscopy of ablation plasma formed around the meteoroid body by collisions with air molecules during its fall. This ablation melts the meteoroid surface, evaporates the body and forms a high temperature shock region in front of the meteoroid body. Emission spectra of the meteoroid plasma store basic information about their elemental composition. Such knowledge allows the classification of the object. Together with descent geometry, spectroscopy enables the recalculation of the meteoroid atmospheric path, its orbit and eventually the determination of its source region in the Solar system. However, the reliability of this method is still subject to discussion (Drouard et al., 2018), (Ferus et al., 2018), (Ferus et al., 2017) (Koukal et al., 2016), (Jenniskens, 2007), (Borovicka, 1993), (Madiedo et al., 2013).

Classical study of real meteorite samples, therefore, remains the only established method and publications focused on detailed analysis of rare specimens of meteorites with known atmospheric paths are highly important. In our study, we explore the bulk elemental composition, mineralogy and the possible source of the famous Porangaba meteorite. The mineralogy and the bulk elemental composition of the meteorite was studied and a surface mineral map was obtained using Energy-Dispersive and Wavelength-Dispersive X-ray Spectroscopy (EDS/WDS) together with Electron Backscatter Diffraction (EBSD). The bulk elemental composition was independently determined by Atomic Absorption Spectrometry (AAS), Inductively Coupled Plasma Mass Spectrometry (ICP-MS), Laser Ablation ICP MS (LA ICP-MS) and Calibration-Free Laser-Induced Breakdown Spectroscopy (CF-LIBS). Based on visual camera records of the Porangaba meteorite fall and using UFOOrbit software (SonotaCo, 2009), its orbit was tentatively calculated and possible candidates of source bodies in the Solar system are proposed here. Simulation of the Porangaba-like (L4 ordinary chondrite) meteor is also provided. This should serve for classification purposes by comparison with records by high-speed video-cameras equipped with simple grating spectrographs.

1.1. History of Porangaba fall

Porangaba (Grossman, 2015) was a very bright daytime bolide that was observed at approximately 17:35 UT on 9 January 2015, in many areas of the state of São Paulo in Brazil. Carlos Augusto di Pietro (BRAzilian Meteor Observation Network, hereafter BRAMON) and Rodrigo del Olmo Sato (Sociedade Brasileira de Meteorítica) calculated the trajectory and the possible rubble field based on two photos of the dust trails from the cities of Lençóis Paulista (Fig. 1, panel A), and Tatuí (Fig. 1, panel B), as well as from video recording from a security camera (Lençóis Paulista). The first piece of this meteorite was found on the same day at S23.159° W48.181°, 6.4 km west-northwest of Porangaba, São Paulo, Brazil. The meteorite had a diameter of 8 cm and weighed 450 g (Fig. 1, Panel C and D, detail in Panel E).

Using these calculations, the second meteorite was found by Julio Caravalho da Silva buried in a small impact crater, which was approximately 10 cm wide and 25 cm deep. Renato Cassio Poltronieri (BRAMON) and M.E. Zucolotto explored the calculated impact area on 18 January. The field location was actually very close to the area calculated by C.A. di Pietro and R. del Olmo Sato. A small fragment was removed and was studied at Museu Nacional in Rio de Janeiro (Grossman, 2015).

A second meteorite search expedition was undertaken between 30 January and 1 February. The expedition was organised by a group of BRAMON members. They found a third, heavier meteorite weighing 520 g on 10 January 2015 (Fig. 1, Panel F). This meteorite was cut into five parts. Subsequently, a specimen of this meteorite weighing 26.7 g was sent to Czechia for analysis. In the current study, we report the results of the analysis of this specimen based on a combination of several different techniques.

2. Materials and methods

2.1. Instrumentation

The 26.7 g Porangaba meteorite specimen was cut in two pieces (Fig. 2). The part denoted as A (Panel A1-A2, Fig. 2) was selected for mineralogical study, which was done at the Czech Geological Survey. The surface of the meteorite was mapped and photographed by Scanning Electron Microscopy (SEM) and optical microscopy. The mineralogy and the bulk elemental composition of the meteorite were determined by EDS/WDS together with EBSD. While EDS is faster, it is less accurate. WDS is slower but provides higher resolution and thus accuracy. In this case, WDS was used mainly for analysis of trace elements. EBSD was used for the determination of different mineral phases in the studied sample. All four techniques mentioned above (SEM, EDS/WDS and EBSD) ultimately provide a mineral phase distribution map of part of the studied meteorite specimen (Fig. 5).

Part B (Panel B1-B2, Fig. 2) of the Porangaba sample was studied by a variety of techniques. Due to the high sample heterogeneity, several techniques were combined to obtain more accurate results, namely AAS, ICP-MS, LA ICP-MS and CF-LIBS. The CF-LIBS study was performed at the department of spectroscopy at the J. Heyrovský Institute of Physical Chemistry. CF-LIBS with optical detection of the emitted laser induced plasma (Ciucci et al., 1999), (Tognoni et al., 2010) is limited to local analysis. This method does not represent a standard technique for the exploration of meteorite composition. However, it has been already employed in several studies (Cousin et al., 2012; De Giacomo, 2011; Dell'Aglio et al., 2010, 2014; Ferus et al., 2018; Hornackova et al., 2014; Lasue et al., 2012; Ozdin et al., 2015; Senesi, 2014; Thompson et al., 2006). Local microanalysis of major, minor and trace elements in the meteorite sample was performed by LA-ICP-MS on the same specimen, which was done at the Department of Chemistry at the Faculty of Science at the Masaryk University.

Finally, this specimen was partially crushed (Panel C, Fig. 2) and used for ICP-MS and AAS analyses. The ICP-MS was performed in the same laboratory on a 0.5 g of decomposed sample. The AAS was conducted at the Department of Nuclear Chemistry at the Faculty of Nuclear Sciences and Physical Engineering, Czech Technical University in Prague.

2.1.1. Electron microscopy and microanalysis

Part A of the Porangaba sample (Panel A1 – A2, Fig. 2.) was polished

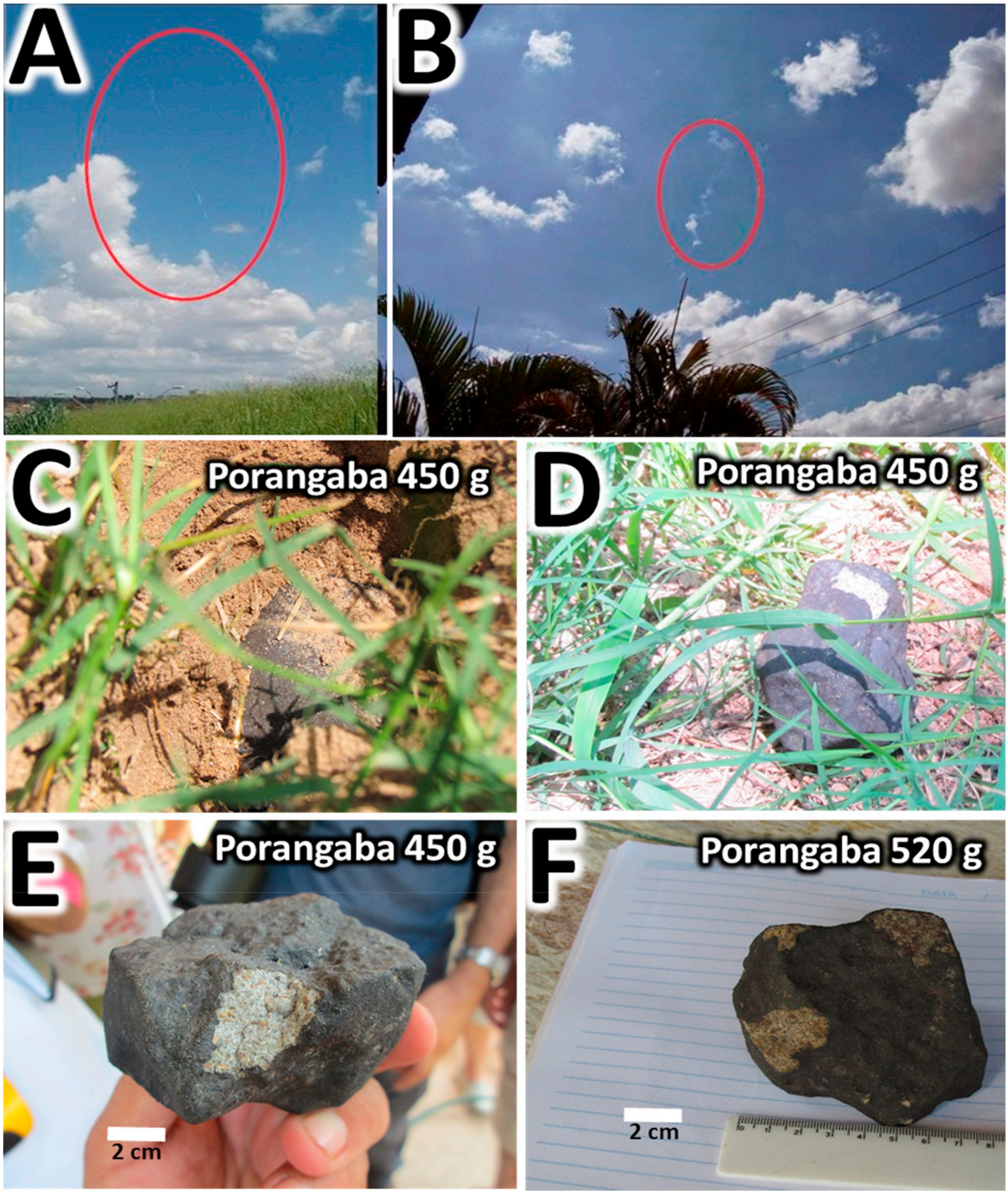

Fig. 1. Panel A shows a photograph of the persistent trail of the Porangaba bolide as photographed from the city of Lençóis Paulista. The persistent trail of the Porangaba bolide as photographed from the city of Tatuí is shown in the panel B. Two large pieces, 450 g and 520 g, discovered close together in impact area, are depicted in the panels C – F.

and subsequently coated with a 30-nm-thick conductive layer of carbon.

A TESCAN MIRA 3GMU (Czech Geological Survey in Prague, Czech Republic) SEM, was used for all the microanalytical studies and for the collection of backscattered electron images and elemental distribution maps. The mineral composition was determined with an Oxford Instruments AZtec Energy Automated analytical system with an X-ray energy dispersive spectrometer equipped with a Silicon drift detector (SDD) X-Max^N 80 Premium (EDS) and an X-ray wavelength dispersive detector Wave 700 (WDS). Both analytical systems installed on the SEM were used for simultaneous EDS/WDS analyses. The analyses were performed at an accelerating voltage of 15 kV, a 20 nA beam current, a 0.090 μm beam size and XPP matrix correction procedures. The acquisition of live measurements for the analysis of the major elements using EDS occurred every 60 s with an output count rate 110 kcps. The time steps for the measurements of the minor and trace elements using the WDS system were 20 or 30 s. To avoid Na and K ion migration during the analysis of glass and feldspar, the beam diameter was increased to 5 μm. For the simultaneous EDS/WDS analysis, a combination of natural and

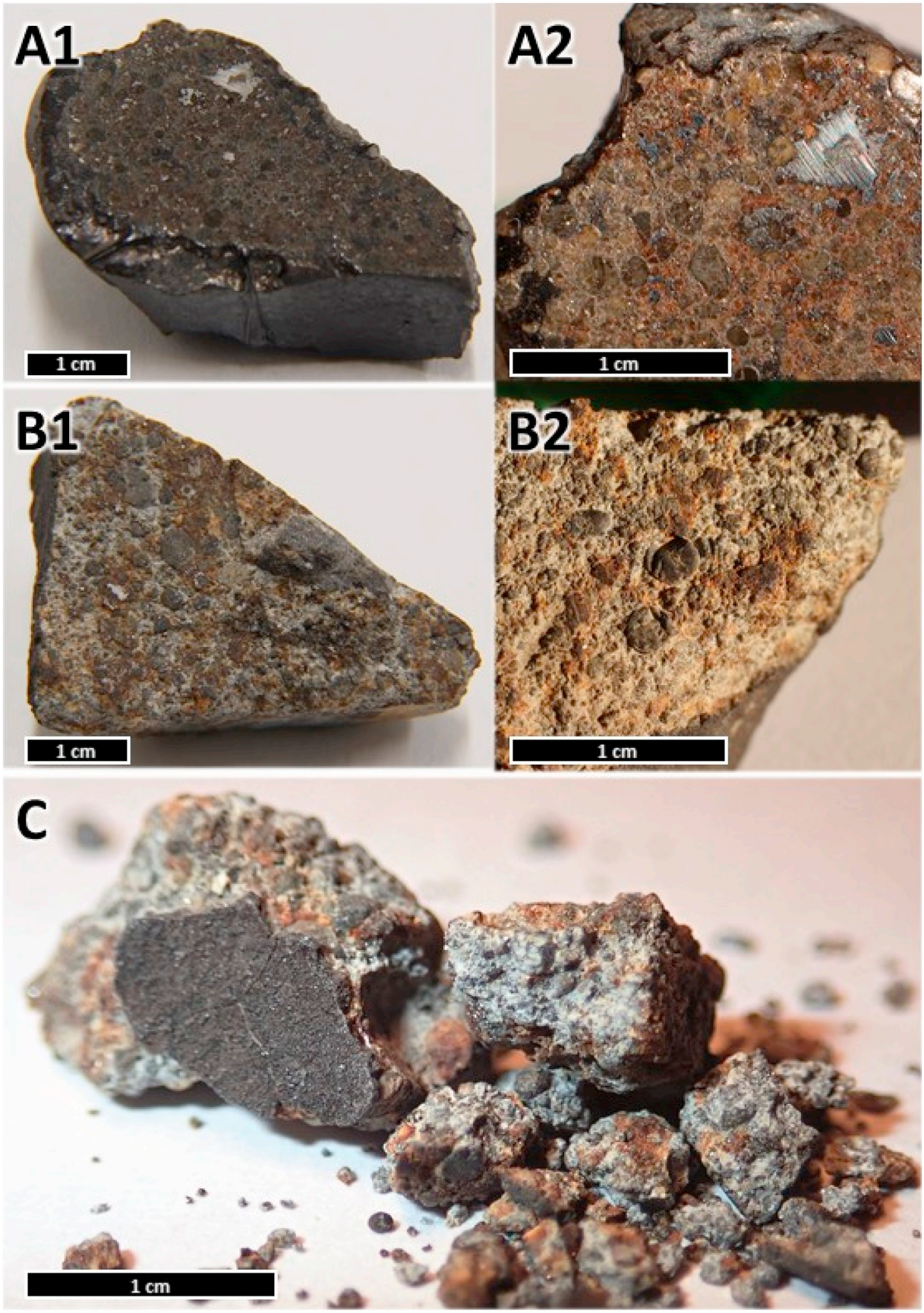

Fig. 2. Photography of our specimen of Porangaba meteorite used for analysis in this study. Panel A1 shows part A of our specimen, which was used for the SEM, EDS/WDS and EBSD analysis. Panel A2 shows a more detailed view of part A. Panel B1 shows part B of our specimen, which was used for CF-LIBS and LA-ICP-MS analysis and panel B2 shows a more detailed view of part B. Panel C shows crushed part B, which was used for ICP-MS and AAS analysis.

synthetic standards was used for the standardisation and calibration procedures.

SEM images and elemental EDS/WDS distribution maps were generated with an accelerating voltage of 15 kV and a 2–10 nA range of the beam current. AZtec Energy Automated software was used to collect multiple wide-range elemental distribution maps covering several randomly selected areas of the meteorite surface. Each elemental distribution map was collected with a resolution of 512 × 512 pixels with a pixel size of 1 μm, where each pixel represents a measurement point from the X-ray spectrum. All the collected X-ray elemental distribution maps were processed using dedicated analytical procedures (TrueMap and Pulse Pile-Up Correction) implemented within the AZtec Energy software to solve the peak overlaps using deconvolution and background subtraction. Sets of elemental distribution maps covering entire regions of the studied section were merged into one dataset for future processing. The subsequent processing of the elemental distribution datasets allows us to study the mineral and chemical characteristics of the samples across the whole thick section on a microscale. The mineral modes and average chemical compositions of the minerals that were present were determined using this dataset and the AZtec PhaseMap software module.

The integrated EBSD was performed by Oxford Instruments AZtec HKL Automated and Nordlys Nano detector, which was installed on the scanning electron microscope mentioned above and was used to confirm the microstructural characteristics of the studied minerals. The analytical parameters used included a 15 mm working distance, 20 kV accelerating voltage and 3.5 nA beam current.

2.1.2. LIBS

The specimen B of sample of the Porangaba meteorite was taken and, without any additional preparation, irradiated by a 10Hz pulsed nanosecond ArF laser (λ = 193 nm with a laser pulse width of 12 ns, frequency of 10 Hz, 1 mm^2 laser ablation spot and output energy of 180 mJ) in an ambient atmosphere. Before each measurement, the surface spot was cleaned by 5 laser pulses. The emission signal from the plasma was collimated and analysed using Echelle high resolution spectrograph (ESA 4000, LLA Instruments GmbH, Germany). The spectrograph allows for the simultaneous measurements of complex spectra in the range 200–780 nm with an effective resolution ranging from 0.005 nm (at 200 nm) to 0.019 nm (at 780 nm). All the atomic spectra recorded by Echelle spectrograph were calibrated against mercury lines. In our measurements, the spectrograph was set to trigger a 12ns laser pulse, a measurement delay of 4 μs was used, and the gate was opened for 5 μs for a total accumulation of 30 LIDB spectra. The low-resolution spectrum was simultaneously recorded by QHI astronomical camera equipped with 1/1000 mm holographic grating. The resulting resolution of the image was 0.4 nm/px. Elemental composition was calculated by CF method, as described in detail the Supplementary Data to the paper.

2.1.3. ICP-MS and LA ICP-MS

Local microanalysis of major, minor and trace elements in the meteorite sample was performed by LA-ICP-MS. Laser ablation was performed at 35 points. The setup consists of laser ablation system LSX-213 G+ (Teledyne, USA) and quadrupole ICP-MS Agilent 7900 (Agilent Technologies, Japan). The ablation system is equipped with a Nd:YAG laser emitting radiation with the wavelength of 213 nm. The sample is placed in an ablation cell (Supercell®, New Wave, USA) where the interaction of the laser radiation with the sample occurs. The ablated material is transported by a carrier gas (helium) with a flow rate 1.0 l/min into ICP-MS. The sample gas (argon) with flow rate 0.6 l/min is admixed to the carrier gas flow behind the ablation cell.

The determination of the overall elemental content in the meteorite sample was done by ICP-MS (Agilent 7900). A 0.5 g was leached in 5 ml of aqua regia and then transferred to 50 ml of deionized water. The leaching was done in triplicates. Before the ICP-MS analysis, the sample was diluted by factor of a 100.

ICP-MS parameters (gas flow rates, sampling depth, electrostatic lenses' voltages of the MS) were optimized in respect to maximize the S/N ratio and counts ratio of ThO^+/Th^+ and U^+/Th^+ lower than 0.2 and 1.1%, respectively. All LA-ICP-MS measurements were done in a single hole drilling mode with laser spot diameter of 100 μm, laser fluence of 7,5 J/cm^2 and repetition rate 10 Hz. For quantification purposes, the certified reference material NIST 610 was used. All measurements were normalized to the total oxide content.

2.1.4. AAS

The contents of Fe, Ni, Co, Mg, Al, Na, Ca, K, Mn, Cr and Ti in part B (Fig. 2, Panel C) were determined by AAS.

After crushing 9 g of the solid sample in an agate mortar, a magnetic (2.47 g) and a non-magnetic fractions (6.25 g) (Haramura et al., 1983; Van Der Auwera et al., 1998; Welten et al., 2011) were separated by a filter paper coated magnet. Both fractions were acid dissolved using distilled, ultra-pure reagents. Throughout the whole procedure, all weights were corrected for moisture content by drying the solid to constant weight at 105 °C.

The magnetic fraction was purified from silicates using HCl and concentrated HF treatment (Welten et al., 2011), while the weight of the sample was reduced from 0.7 g to 0.25 g. An aliquot weighing 0.1 g was then dissolved in 1:2 HNO_3/HCl and slowly evaporated. The residue was dissolved in HNO_3 and transferred to demineralized water and a volumetric flask (9.7% of the sample undissolved). Non-magnetic fraction (0.5 g) was exposed to a concentrated HF/HCl mixture in an open acid digestion and consequently treated with HNO_3 (Van Der Auwera et al., 1998). 22.2% of the sample remained undissolved.

The determination was carried out on the Spectr AA - 240 FS instrument (Varian) with the evaluation program in the PROMPT mode (maximum sample measurement time 10 s). Standards were prepared from certified calibration solutions Astasol (Analytika, s.r.o.). Fe, Na, and K were determined in the air-acetylene flame, other elements in the nitrous oxide-acetylene flame. To suppress ionization in the case of Na, K, and Ca, cesium chloride solution was added to give a final concentration of 1000 mg/L of cesium in all solutions including the blank. Correction for non-specific absorption was performed. The measurement was done with a maximum error of ±3%.

2.2. Calculation of the trajectory

For calculation of the Porangaba bolide trajectory, only a low-quality security camera video of the bolide and two photographs of the atmospheric smoke trail visible after the bolide event were available. Detailed description of the calculations together with in-depth results is provided in Supplementary Data to the paper. The bolide event security camera video was used to determine the angular velocity of the body. Due to the high field distortion in combination with the event position in the upper right corner of the camera field, determining the beginning and end points of the track with sufficient accuracy was not possible.

3. Results

3.1. Petrography and mineral composition

The Porangaba meteorite has been found shortly after the observed fall, and its very fresh nature is reflected in the absence of widespread weathering with the exception of weak veins on the surface of the fusion crust. These observed weathering features indicate a weathering grade of W0, according to the Wlotzka classification (Wlotzka, 1993). The structure of the specimen was significantly brecciated and rock fragments, including chondrules, were only slightly cemented. The relatively poor quality of the polished surface, the presence crumbling, relief etc., corresponds to a considerable sample incoherence. Furthermore, the specimen appears to be a heterogeneous mixture of fragments of different materials.

It was found that the main component of the sample is represented by fragments of enstatitic and rarely even forsteritic particles and isolated chondrules with a high proportion of forsteritic olivine in the matrix. The meteorite shows clearly visible and sharply defined chondrules and a fine-grained matrix (Fig. 3).

Chondrule sizes vary from approximately 0.4 mm to 5 mm and they have a very complicated and unstable internal structure. The chondrules consist mainly of olivine ($Fa_{21–25}$) mean $Fa_{23.6}$, with percent mean deviation (PMD) - FeO 2.9%, $n = 44$; and low-Ca pyroxene ($Fs_{17–23}Wo_{0.7–1.2}$) mean $Fs_{20.0}$ $Wo_{0.96}$, Fs PMD 5.5%, Wo PMD 11.3%, $n = 52$. Alkali-bearing glasses exhibit a wide range of chemical compositions. Most of the secondary feldspar grains are <2 μm in size, but some are larger.

The matrix is probably composed mainly of plagioclases and small fragments or even crystals of pyroxene. Moreover, irregularly bounded grains formed by Fe—Ni metal alloy were found in the matrix, too. It is clearly two-component and consists of a remission of α-(Fe, Ni) i.e. kamacite (usually about $Fe_{95}Ni_5$) and γ-(Fe, Ni) i.e. taenite (around $Fe_{0.6}Ni_{0.3}$). It was also found usually round grains, consisting of troilite (Stoichiometric FeS). Troilite quite often merges with the metal component. Furthermore, chromium spinelide grains were found to be quite rare in the matrix. This is, when converted to the contents of end members, made up of about 75% chromite component. In addition, an admixture of hercynitine and magnesiochromite components (both up to about 10 mol%) was found in spinelide. Chromites also contain slightly increased proportions of TiO_2 around 2% (approx. 2.5 mol% of ulvospinel component).

Recrystallization of the fine-grained matrix is visible in the thin section (Fig. 3).

Remission of plagioclase and Mg—Fe silicate components (enstatite) in chondrules and matrix, was frequently observed. While enstatite forms idiomorphic to hypidiomorphic crystals, the feldspar mass (alumosilicate Na—Ca) is clearly non-crystalline and contains many unidentifiable inclusions of submicrometric sizes.

Our investigations based on SEM and EDS/WDS measurements of average olivine and average low-Ca pyroxene composition show that these two minerals have composition of $Fa_{23.6}$ and $Fs_{20.0}$ $Wo_{0.96}$, respectively. This implies that the Porangaba meteorite should be classified as an ordinary chondrite L (Fig. 4).

The absence of visible plagioclase grains suggest that the Porangaba meteorite is a petrologic type 4. Orthopyroxene (Fe enstatite) produces hypidiomorphic to xenomorphic grains and is found in both breccia and some chondrules. In addition to orthopyroxene, the sample also contains clinopyroxene diopside composition. This produces isolated crystals in the feldspar mass matrix of the sample and occasionally increases in the orthopyroxene grains.

Olivine and pyroxene in this L4 lithology show weak shock features, represented by the undulate extinction of olivine and orthopyroxene grains and the presence of irregular fractures corresponding to the shock stage S2, i.e., very weak impact shock metamorphism (5–10 GPa) (Stöffler et al., 1991). The EBSD method did not confirm the presence of plagioclase-maskelynite conversion typical for higher shock stages.

Detailed composition of olivine and low-Ca pyroxene in comparison to several previous published L4 chondrites is shown in Tables 1.a and 1.b.

The mineral modes obtained by the AZtec Phase Map Analysis were recalculated into % weight and are presented in Table S7. The distributions of the mineral phases and textures of the studied meteorite are shown in Fig. 5.

Both Tables 1.a and 1.b show very reasonable agreement between the mineralogy of the Porangaba and other meteorites classified as type L4. Particular very small deviations from other specimens presented in these tables can be found for cases of rare metal oxides such as TiO_2 and Al_2O_3. On the other hand, the analysis of olivine exhibits a very good agreement with the typical composition of L4 representatives shown in the table. However, as shown in the following chapter, the bulk composition of Porangaba represents an interesting case of a meteorite exhibiting Fe/Mg ratios between those of L and H type of ordinary chondrites.

3.2. Bulk elemental composition

The bulk elemental composition of the Porangaba meteorite was first determined by SEM and EDS/WDS (MA) analysis. However, the studied meteorite surface exhibits significant heterogeneity (see Fig. 5), so another four analytical techniques were used for comparative

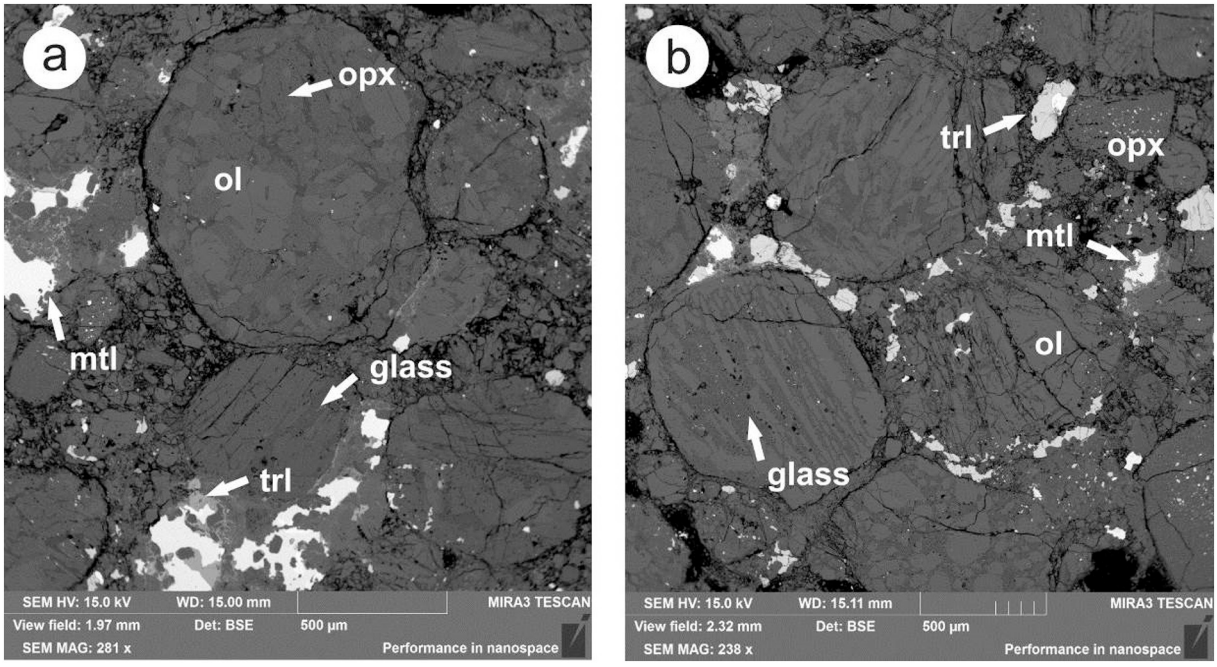

Fig. 3. Backscattered electron images representing the texture of the Porangaba L4 ordinary chondrite include sharply defined chondrules and fine-grained matrices. Minerals: ol-olivine, opx-orthopyroxene, mtl-metals (kamacite-taenite), trl-troilite, and glass-glass.

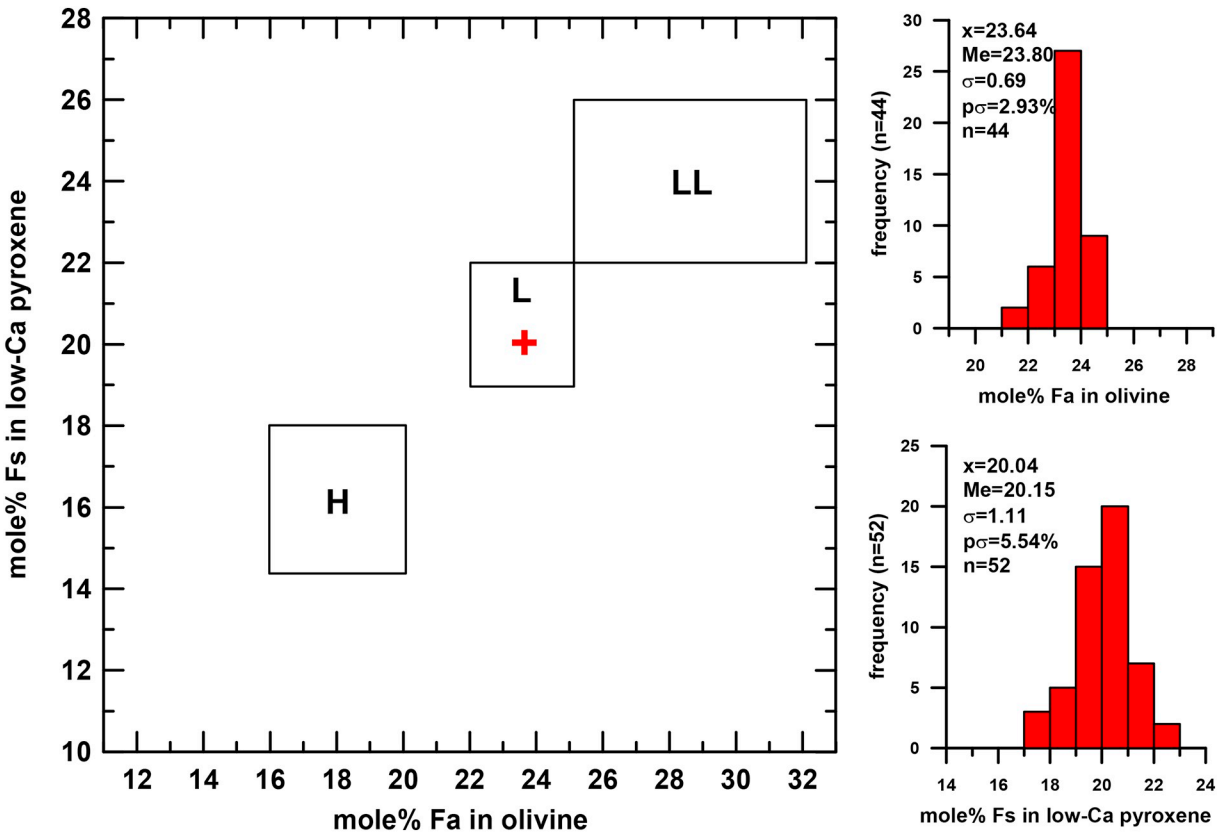

Fig. 4. Classification scheme of the L4 Porangaba ordinary chondrite based on the molar olivine (fayalitic content) and low-Ca pyroxene (ferrosilite content) composition. H, L, and LL indicate typical ranges for H, L, and LL ordinary chondrites compiled from (Brearley and Jones, 1998). Fa-fayalite, Fs-ferrosilite, x-average composition, Me-median, σ-mean deviation, ps-percent mean deviation, and n-number of point analysis are also shown.

Table 1.a
Average electron microprobe analyses of olivine for Porangaba (this study) and a group of selected L4 meteorites (Dunn et al., 2010).

Average electron microprobe analyses of olivine					
L4 Ordinary chondrites	Porangaba	Atarra	Bald Mountain	Rio Negro	Rupota
SiO_2	38.33	38.2	38.2	38.3	38.1
Cr_2O_3	0.00	0.11	0.09	0.03	<0.03
FeO	21.89	21.4	21.3	22.5	22.4
MnO	0.47	0.46	0.46	0.46	0.46
MgO	39.31	39.7	40.1	38.9	38.8
CaO	0.00	0.03	<0.03	0.04	0.05
Total	100	99.9	100.1	100.3	99.9
Cations based on 4 oxygens					
Si	1.00	0.99	0.99	1.00	1.00
Cr	0.00	0.00	0.00	0.00	0.00
Fe	0.48	0.46	0.46	0.49	0.49
Mn	0.01	0.01	0.01	0.01	0.01
Mg	1.52	1.54	1.55	1.51	1.51
Ca	0.00	0.00	0.00	0.00	0.00
Total	3.1	3.1	3.1	3.00	3.00
Fe/Mn	48.0	46.2	46.2	46.2	48.9
Fe/Mg	0.32	0.30	0.30	0.30	0.32
Fa	23.6	23.2	22.9	24.5	24.5

Table 1.b
Average electron microprobe analyses of low-Ca pyroxene for Porangaba (this study) and a group of selected L4 meteorites (Dunn et al., 2010).

Average electron microprobe analyses of low-Ca pyroxene					
L4 Ordinary chondrites	Porangaba	Atarra	Bald Mountain	Rio Negro	Rupota
SiO_2	55.32	55.6	55.5	55.4	55.4
TiO_2	0.08	0.14	0.13	0.15	0.18
Al_2O_3	0.06	0.16	0.18	0.36	0.23
Cr_2O_3	0.20	0.15	0.19	0.40	0.21
FeO	13.7	13.2	13.0	13.4	13.4
MnO	0.48	0.45	0.49	0.46	0.46
MgO	29.51	29.9	29.8	29.4	29.0
CaO	0.64	0.41	0.80	0.7	1.02
Na_2O	0	0.03	<0.03	0.05	0.03
Total	99.99	100.0	100.1	100.2	99.9
Cations based on 6 oxygens					
Si	1.98	1.98	1.98	1.98	1.98
Ti	0.00	0.00	0.00	0.00	0.00
Al	0.00	0.01	0.01	0.02	0.01
Cr	0.01	0.00	0.01	0.01	0.01
Fe	0.41	0.39	0.39	0.40	0.40
Mn	0.01	0.01	0.01	0.01	0.01
Mg	1.57	1.59	1.59	1.56	1.55
Ca	0.02	0.02	0.03	0.03	0.04
Na	0.00	0.00	0.00	0.00	0.00
Total	4.01	4.01	4.01	4.01	4.01
Fe/Mn	27.3	28.9	26.3	29.2	29.2
Fe/Mg	0.26	0.25	0.24	0.26	0.26
Fs	20.0	20.2	19.9	20.6	20.7
Wo	0.96	0.8	1.5	1.3	2.0

determination of the bulk elemental composition. They were CF-LIBS, LA-ICP-MS, ICP-MS and AAS. Comparison of the results obtained by each method mentioned above is summarized in Table 2.

The classification of the Porangaba meteorite specimen into the relevant chemical group was based on the value of the Fe/Mg ratio, which was previously published for a wide range of meteorites (Nittler et al., 2004). The authors of this study state that ordinary chondrites

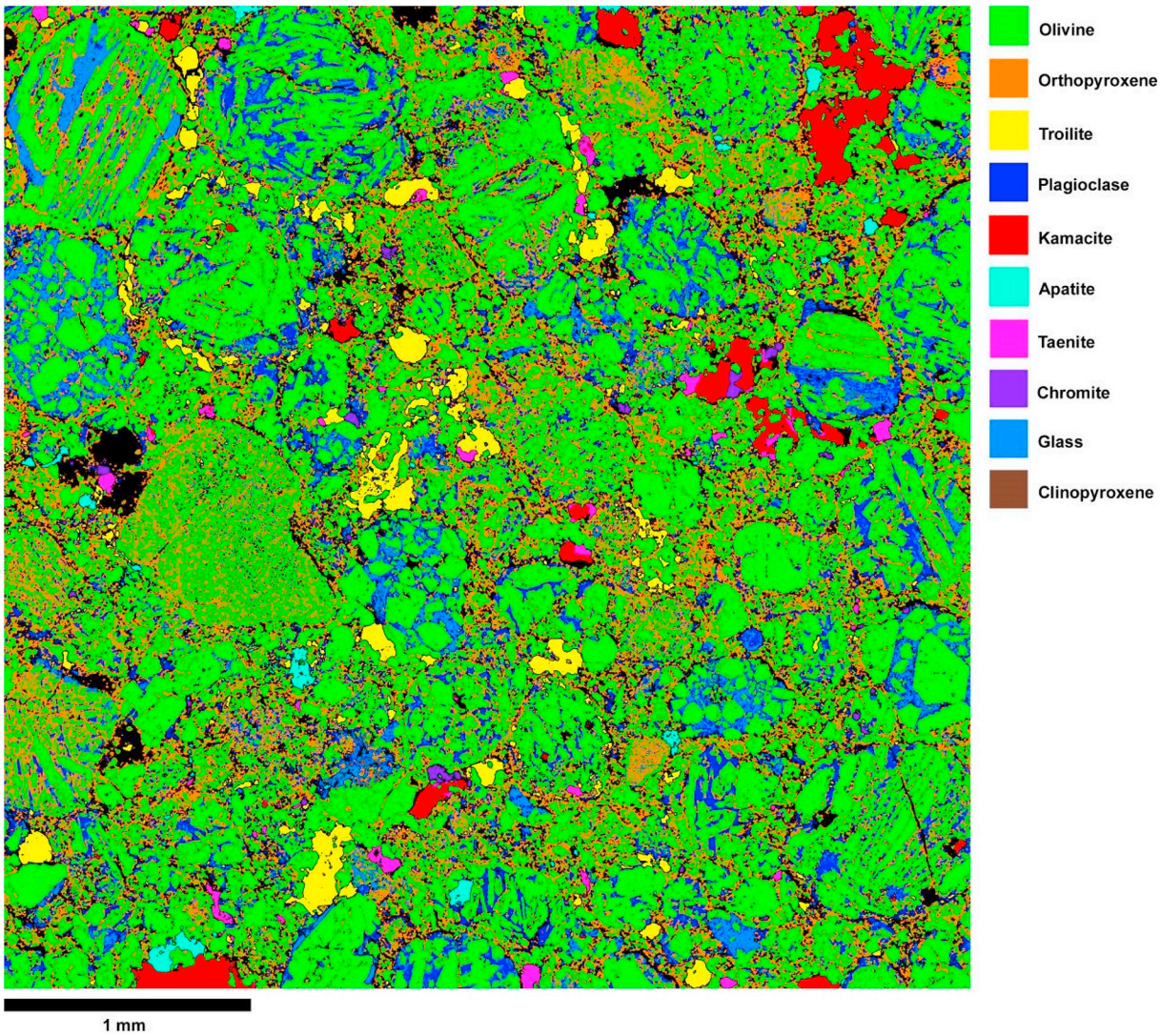

Fig. 5. Phase distribution map of part of the studied thick section of the L4 Porangaba ordinary chondrite showing the distribution of the main rock-forming minerals and meteorite textures. The modal abundances of the minerals are as follows: olivine 43.8 wt%, orthopyroxene 25.6 wt%, clinopyroxene 2.8 wt%, plagioclase 4.5 wt %, kamacite 5.9 wt%, taenite 2.2 wt%, troilite 7.5 wt%, chromite 0.3 wt%, apatite 0.6 wt%, glass 6.5 wt%, and other minerals 0.3 wt%.

exhibit a trend of decreasing magnesium content with an increasing iron content in the order LL → L → H → EH. The range of the Fe/Mg values typical for LL, L and H chondrites together with the Porangaba value are depicted in Fig. 6. The Porangaba specimen exhibits Fe/Mg ratio ranging from 1.936 (estimated by ICP-MS) to 1.337 (estimated by LA-ICP-MS). It is clearly visible that all the results are not in good agreement with values typical for L-chondrites. We believe that it is because of large heterogeneity of the specimen.

3.3. Trajectory and probable origin of the meteoroid

The Porangaba sporadic bolide was a very slow meteor; its geocentric velocity before entering the Earth's gravitational field was 12.6 ± 2.1 km/s (without the effect of deceleration) with the geocentric radiant RA = 316.5 ± 7.5° (right ascension), DEC = 10.6 ± 1.4° (declination). Due to the methodology of orbit computation, the deceleration was not involved in the calculations. Large uncertainties exist in the heliocentric

Table 2
Comparison of ratios of selected chemical elements and magnesium analysed by various methods.

Weight ratio of elements [wt%/wt%]	L type ordinary chondrites [wt%] (Drouard et al., 2018)	Elemental analysis ICP-MS [wt%]	Elemental analysis AAS [wt%]	Minerals analysed (MA) [wt%]	Elemental analysis CF-LIBS [wt%]	Elemental analysis LA-ICP-MS [wt%]
Fe/Mg	1.44	1.936	1.705	1.682	1.942	1.337
Si/Mg	1.24	–	–	1.235	0.620	1.989
Al/Mg	0.08	0.007	0.082	0.111	0.127	0.149
Ca/Mg	0.09	0.012	0.062	0.061	0.172	0.176
Na/Mg	0.05	0.016	0.066	0.069	0.018	0.120
Cr/Mg	0.03	0.001	0.002	0.021	0.042	0.029
Ni/Mg	0.08	0.146	0.291	0.050	0.043	0.107
Co/Mg	0.004	0.005	0.031	0.009	–	0.005
Ti/Mg		0.002	0.000	0.004	0.052	0.005

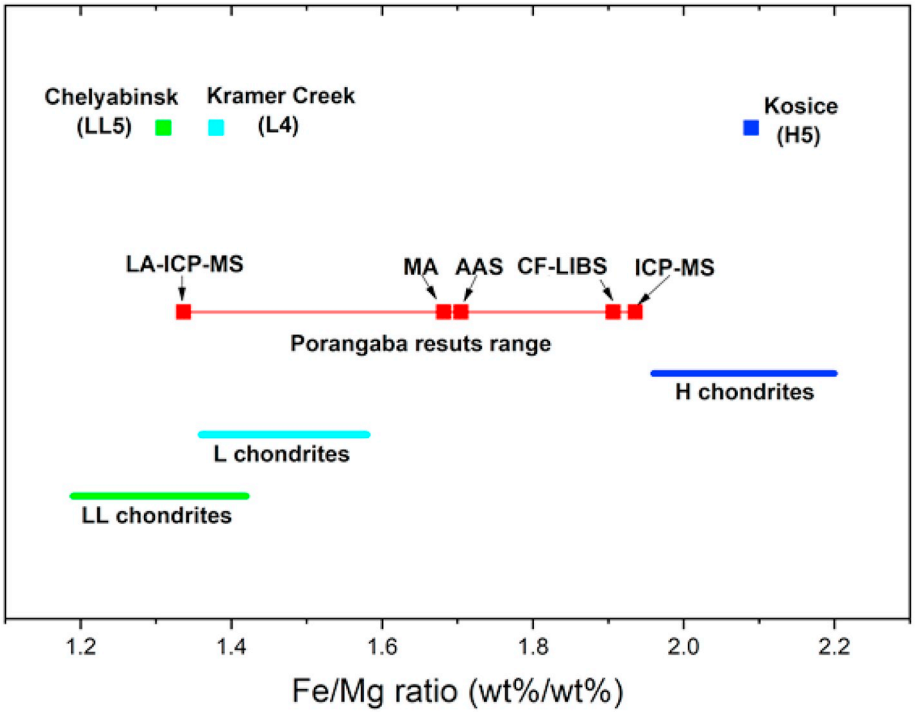

Fig. 6. Comparison of the Fe/Mg ratio values of each H, L and LL (Nittler et al., 2004) ordinary chondrite chemical group together with results of each analysis (LA-ICP-MS, MA, CF-LIBS, AAS and ICP-MS). The results range from 1.337 (LA-ICP-MS) to 1.936 (ICP-MS). For reference, values of the Fe/Mg ratio of another three meteorites: Kosice (H5) (Ozdin et al., 2015), Kramer Creek (L4) (Gibson et al., 1977) and Chelyabinsk (LL5) (Galimov et al., 2013) are depicted.

orbital elements, as do uncertainties of the geocentric radiant position and geocentric velocity, which are caused by the input data presented in this work (Tables 1.a–3).

In order to calculate the atmospheric path of the bolide and orbit of the meteoroid in the Solar System, photographs of the trail from Lençóis Paulista and Tatuí were used. The calculated values are shown in the Table 3 and the details are provided in the Section S1 of the Supplementary Data to the paper. The projection of the beginning of the visible atmospheric path, depicted schematically in Fig. 7, was located at the coordinates S23.009° W48.186° near the village of Pirambóia, São Paulo, Brazil. The height of the bolide at this time was 49.7 ± 4.2 km above the Earth's surface. The end of the projection of the visible atmospheric path was located at S23.163° W48.157°, which is near the city of Porangaba. The height of the bolide at this time was 19.0 ± 1.8 km above the Earth's surface. The absolute magnitude of the Porangaba bolide was not calculated and neither was an estimate of the body's initial mass before entering the Earth's atmosphere. In any case, the body entered the Earth's atmosphere at a high zenith angle of 60.5° and its terminal height was very low (<20 km above the Earth's surface).

The estimated projection of the derived Porangaba orbits in the Solar System is depicted in Fig. 8. It shows that the Porangaba initial body probably comes from the outer side of the Main asteroid belt (Table 4 & 5).

Table 3
Heliocentric orbital elements (J2000.0) of Porangaba, calculated using the software UFOOrbit (SonotaCo, 2009).

Semimajor axis	A	2.54 ± 1.10 AU
Eccentricity	E	0.64 ± 0.11
Perihelion distance	Q	0.91 ± 0.05 AU
Aphelion distance	Q	4.17 ± 2.20 AU
Argument of perihelion	ω	142.8 ± 6.7°
Longitude of ascending node	Ω	288.921 ± 0.001°
Inclination	I	8.6 ± 3.2°
Orbital period	P	4.04 ± 2.91 y
Heliocentric velocity	v_h	38.1 ± 1.4 km/s

3.4. Simulation of Porangaba meteor spectra

In addition to the laboratory CF-LIBS analytical technique, emission spectroscopy can also contribute to the analysis of the chemical composition of meteors (Berezhnoy and Borovicka, 2010; Borovicka et al., 1999; Borovička and Betlem, 1997; Jenniskens, 2007; Madiedo et al., 2013). In our previous study, we published a Calibration Free analysis of Perseid and Leonid meteors (Ferus et al., 2018). Porangaba was not recorded on a spectrographic camera, regarding the future potential of meteor spectroscopy, the application of Calibration Free calculations and the experimental approaches employing laser ablation for meteor spectra simulation, however, we briefly discuss in this section the simulated meteor spectra of this interesting specimen.

If a body disintegrates and none of its fragments are found as meteorites, the spectrum becomes the only record of its chemical composition. In such case, spectroscopic techniques play an important role. However, the current state of art in this field is not optimistic. There are only two cases of parallel record of both meteor spectra and an existence of a sample of the corresponding meteorite: Žďár nad Sázavou (9 December 2014) and Neuschwanstein (4 April 2002) (Ferus, 2015). Comparisons of their spectroscopic analyses together with reference measurements using LIBS and other laboratory methods have not been published for either meteor.

In the case of Porangaba, we calculated synthetic spectra based on the concentrations obtained from the elemental analysis. These are shown in Fig. 9, panels A and B. The synthetic spectra were generated by summing the Voigt spectral line profiles with the emission intensities calculated from the available spectroscopic data from the National Institute of Standards and Technology (NIST) website database (A. Kramida et al., 2019). The ratio of the neutral atoms to ions (singly- and doubly-charged ions were included) was calculated using an iterative method of Saha's equations solution (Zaghloul, 2004). The code used for the simulation includes also a simple radiative transfer model (a homogeneous plasma block of changeable size) which is able to partially correct the emission intensities for the self-absorption.

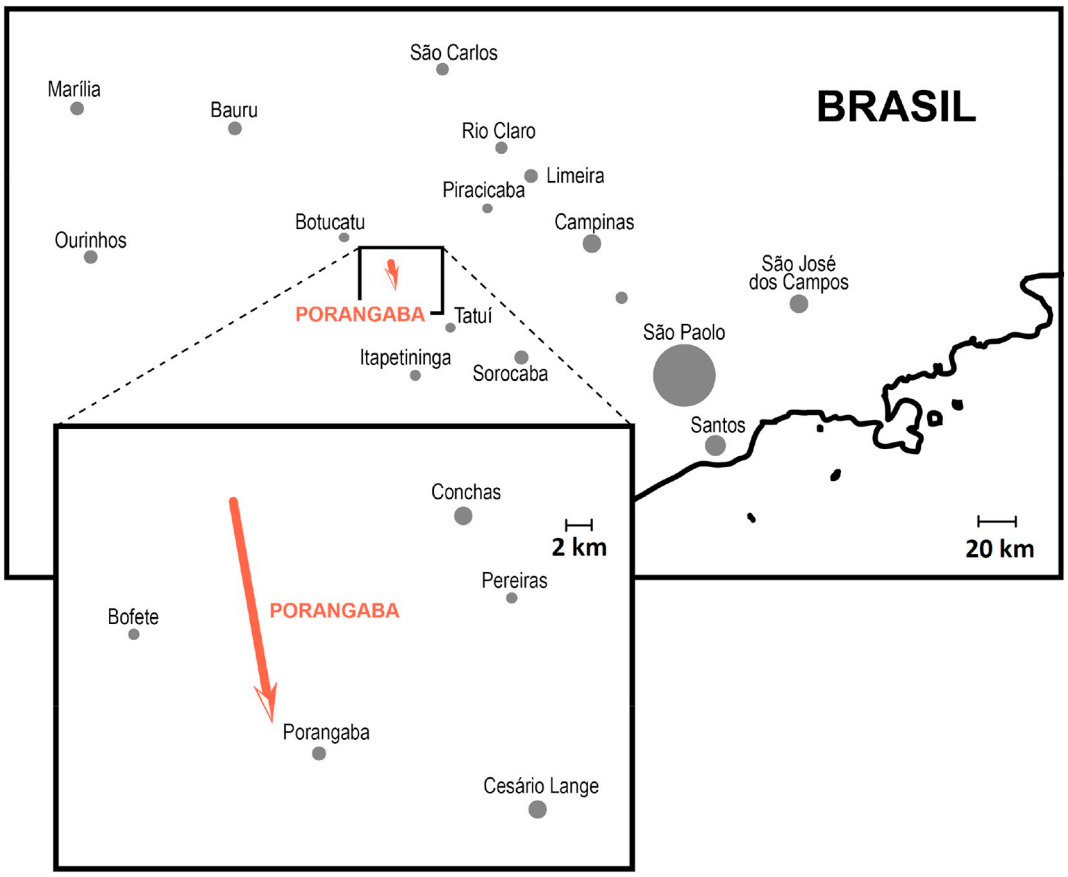

Fig. 7. Projection of the Porangaba atmospheric path over the Earth's surface.

We calculated two types of the synthetic spectra. The first (Fig. 9, panel B) is the simulation of the laboratory ablation experiment. In this case, the input parameters were set according to the experimental ones. The plasma temperature was set to 8258 K, according to the temperature estimated using the Saha-Boltzmann plot in Fig. S11 of the Supplementary Data section. The plasma pressure was set to 1 atm. For the radiative transfer model a block of plasma 3 mm on each side was used. The two spectra in panel B were computed from the same data and with the same parameters; they only differ by the chosen instrumental function. One of them has a low resolution (corresponding to the meteor spectrographic camera resolution) and the other has a higher resolution, corresponding to the high-resolution spectra obtained in laboratory measurements by the Echelle spectrograph.

The second type of the synthetic spectra (Fig. 9, panel A) simulates the radiation which would be emitted during the impact of the studied body into the atmosphere. The real observed spectra of meteor plasma contain two components corresponding to two different temperatures, usually around 5000 K and 10,000 K (Borovicka, 1993). For this reason, we have calculated three synthetic spectra using different temperatures: 5000 K is used for the "cold" part of the meteor plasma and 10,000 K and 12,000 K are used for the second "hot" component. It is assumed that this component comes from a very hot area near the front of the meteor and its temperature varies. To simulate the conditions in the meteoric plasma we set the plasma pressure and the size of the radiative transfer model block to 100 Pa and 1 m, respectively. The resulting three-component synthetic spectrum is shown in Fig. 9, panel A. Finally, panel C shows two experimental emission spectra of Porangaba from the ablation point C1.

As can be seen in the Fig. 9, the synthetic spectra (panel B) and the ablation spectrum of Porangaba (panel C) are in reasonable agreement. However, in some narrow spectral regions (e.g., near 422.5 nm), small differences between theoretical simulation and experimental data can be noticed. They are caused mainly by the self-absorption effect in the nonhomogeneous ablation plasma which cannot be simulated by the used radiative transfer model only valid for homogeneous environments. Another effect which make classical quantitative interpretation inaccurate is the matrix effect. However, the presented technique of calibration free calculation reduces these effects by careful selection of the spectral lines used for the analysis and is able to calculate the elemental ratios from real observed spectra with sufficient precision.

4. Discussion

The Porangaba meteorite specimen represents a fresh L4 type chondrite material originating from a small meteoroid with an expected diameter of tens of centimetres (Collins et al., 2005).

The undulatory extinction of olivine and orthopyroxene grains and the presence of irregular fractures in the part A of our specimen (Fig. 2; Panel A1-A2) (estimated by SEM, EDS/WDS and EBSD) correspond to its very weak shock stage S2 (Stöffler et al., 1991). This fact implies that the Porangaba parent body must have been exposed to shock pressure 5–10 GPa and has undergone a post-shock temperature increase from 20 to 50 °C. The lack of significant weathering also signifies that the material mostly retains its original composition in interplanetary space.

The heterogeneous brecciated structure of the meteorite, as described above, could imply that the Porangaba meteorite originates from body with a rubble-pile structure, where the parent body was probably collisionally disrupted and gravitationally reassembled together with another different geochemical and petrological types of meteoroids. For example, the composition of the Morávka (Borovicka et al., 2003) meteorite was determined as a mixture of H5 and H6 ordinary chondrites. Yet another example is the Itokawa asteroid, which

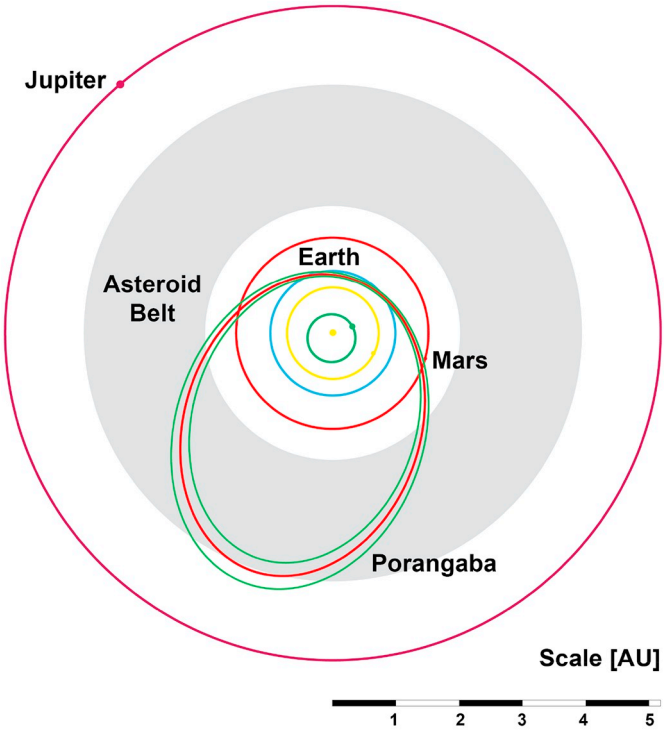

Fig. 8. Projection of the derived Porangaba orbits in the Solar System. The mean orbit is shown in red, while the green orbits represent those based on combinations of the Porangaba orbital element errors. The latter appear in the following order (from the smallest semi-major axis, in the parenthesis number of the solution): *q*-*e*- (6), *e*- (4), *q* + *e*- (8), *q*- (2), mean orbit (1), *q* + (3). The boundaries of the main asteroid belt are depicted - inner, middle and outer (marked in gray), defined by asteroid orbits with average eccentricity in a given part of the main-belt. (For interpretation of the references to colour in this figure legend, the reader is referred to the web version of this article.)

Table 4
Geocentric radiant, geocentric velocity of Porangaba, calculated using the software (SonotaCo, 2009).

Geocentric velocity	v_g	12.6 ± 2.1 km/s
Radiant right ascension	*RA*	316.5 ± 7.5°
Radiant declination	*DEC*	10.6 ± 1.4°

Table 5
The atmospheric path parameters of Porangaba calculated using the software UFOOrbit (SonotaCo, 2009).

Beginning latitude of the atmospheric path projection	LAT_B	−23.009 ± 0,021°
Beginning longitude of the atmospheric path projection	LON_B	−48.186 ± 0.029°
Beginning height of the atmospheric path projection	H_B	49.7 ± 4.2 km
Terminal latitude of the atmospheric path projection	LAT_E	−23.163 ± 0.013°
Terminal longitude of the atmospheric path projection	LON_E	−48.157 ± 0.024°
Terminal height of the atmospheric path projection	H_E	19.0 ± 1.8 km

was examined by Hayabusa spacecraft in December 2005 and which is considered a rubble-pile structured body, too (Abe et al., 2006).

The bulk elemental composition results of each analysis (depicted in Table 2) are quite different to each other and none of them quite fit to the L chondrite group. Especially in the case of the Fe/Mg ratio, which was chosen for the classification of the meteorite specimen to an appropriate geochemical group, there is a significant variance, which makes it difficult to classify the meteorite specimen into one group correctly. The Fe/Mg results of individual analyses are 1.37 (LA-ICP-MS), 1.682 (MA), 1.806 (CF-LIBS), 1.707 (AAS) and 1.936 (ICP-MS). The typical range of Fe/Mg for L chondrite group is 1.38–1.52 (Nittler et al., 2004). The graphic demonstration of ranges of Fe/Mg ratios for LL, L and H chemical group together with the average value of the Porangaba meteorite and other three meteorites are depicted in Fig. 6. It is clearly visible that none of these results agree with the L group. The MA, CF-LIBS, AAS and ICP-MS results lie between the values for L and H groups. In the case of LA-ICP-MS value of Fe/Mg even corresponds to the LL group. On the other hand, it is clearly visible that the Fe/Mg ratio of Chelyabinsk LL5 meteorite (Galimov et al., 2013), Kramer Creek L4 meteorite (Gibson et al., 1977) and Košice meteorite H5 (Ozdin et al., 2015) perfectly fit to their respective groups. However, the content of fayalite in olivine ($Fa_{23.6}$) and the content of ferrosilite ($Fs_{17–23}$) and wolastonite ($Wo_{0.96}$) in low-Ca pyroxene (obtained by SEM EDS/WDS, Fig. 4.) show that Porangaba meteorite specimen perfectly corresponds to the L group (Brearley and Jones, 1998). Nevertheless, classification based on the analysis of olivine and low-Ca pyroxene takes into consideration only the composition of these two minerals, but not the others, such as the abundance of Fe—Ni metal grains, which, according to the results of previously published analysis accessible on (Mindat.org 2016) and the Meteoritical Bulletin Database (Grossman 2015) state that Fe—Ni grains occupy ~6% of the area of the Porangaba meteorite. We note that except SEM EDS/WDS, all the methods are destructive (although ablation techniques evaporate a very small amount of the sample) and therefore the sample has been further divided in several pieces analysed by techniques mentioned above.

Considering the very limited accuracy of calculations based on the very poor-quality data, we provide only tentative orbital parameters and list of several bodies (Table S2 in Supplementary Information section) with close orbital elements. Nevertheless, given the short list of meteorites with documented elemental compositions, mineralogies and sources in the Solar System, we still believe that even such raw data can be valuable, because the knowledge of the distribution of different types of asteroids in the Solar system according to their chemical composition could give us important information about the formation and evolution of our Solar system. This distribution has been studied for many years and it is still not exactly clear. Some studies (DeMeo and Carry 2013; Gradie and Tedesco., 1982) have shown the existence of a global compositional heliocentric gradient in the asteroid main belt. For example, S-type asteroids dominate in the inner part and C-types in the outer part of the main asteroid belt. Furthermore, the oxidation level of bodies generally increases with the heliocentric distance i.e. oxidised asteroids have typically larger heliocentric distances than reduced asteroids.

Careful analysis and retrograde calculation of the mean orbital elements of the potential Porangaba parent body are described in detail in the Supplementary Data (Section S1, particularly S1.3.). On the basis of this analysis, we can conclude that the body exhibits a resonance with Jupiter orbital trajectory in a ratio 3:1 and 4:1. These resonances are in good agreement with the Kirkwood gaps (See Table S3 and (Minton and Malhotra 2009)).

The calculations are introduced in detail in the Chapter S1.1. The estimated orbital trajectory is depicted in Fig. 8. In this computation, the heliocentric distance of Porangaba was determined to be 2.54 ± 1.10 AU. Based on the Tisserand's parameter of the meteor orbit ($T_j = 3.414$), we assume that the parent body of the Porangaba meteorite is probably an unknown object from the main asteroid belt. A summary of potential parent bodies of the Porangaba meteorite is given in the Supplementary Data (Table S2). One of the probable parent bodies is asteroid 1998 SU27, classified as a transient Sq type. The spectrum of this object has already been measured. However, we should note that the accuracy of this determination is strictly limited by the very scarce knowledge of the meteor descent parameters. In general, based on the facts above, we can state that it is a body exhibiting orbital resonance 3:1 with respect to Jupiter and it belongs to the group Q or O based on the SMASSII

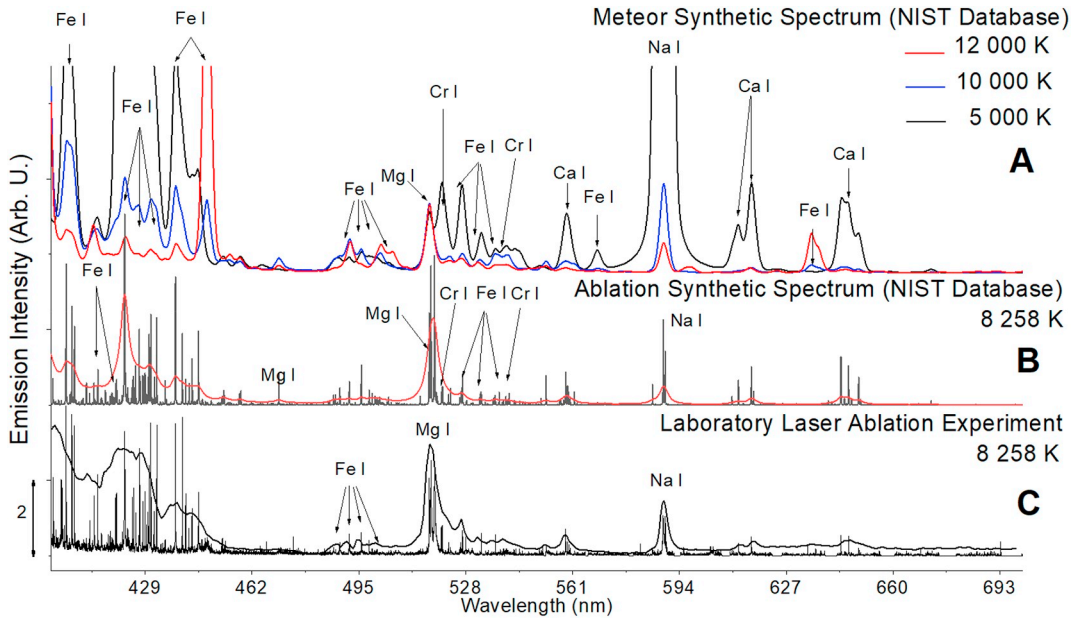

Fig. 9. Panel A shows a simulation of the Porangaba meteor spectra calculated using three temperature components (12,000 K, 10000 K and 5000 K) and NIST Database (A. Kramida et al., 2019). Panel B shows a simulation of the Porangaba ablation spectra (B, calculated using one temperature component, 8258 K. This temperature was determined from the LIBS analysis using the Saha-Boltzmann plane plot). The spectra were calculated in both high- and low- resolutions. Panel C shows experimental laboratory data recorded using a high-resolution spectrograph and a low-resolution spectral camera (the same as the camera used for real meteor spectra observation).

taxonomy.

Orbital trajectories in these resonances are generally unstable in longer time horizons and the perihelion is moving from the orbits outside the trajectory of the Earth to the inner part of the Solar System. Such movement also means that the bodies reach a collisional course with Earth. The perihelion is moved to the space between Earth and Sun and the aphelion can be usually found in the main asteroid belt. In the current literature we can find that by a comparison of the reflectance spectra, albedo and colour characteristics using the SMASSII taxonomy (Bus and Binzel 2002) with types of bodies in the main asteroid belt, ordinary chondrites type L and LL, such as Porangaba, are very close to Q-type of asteroids.

5. Conclusions

The Porangaba meteorite specimen represents a fresh chondritic material with a very heterogeneous brecciated character. The specimen appears to be a heterogeneous mixture of fragments of different materials.

Based on the molar olivine ($Fa_{23.6}$) and low-Ca pyroxene (Fs_{17-23}, $Wo_{0.96}$) composition obtained by SEM EDS/WDS, the Porangaba can be classified as an L chondrite. However, the Fe/Mg ratio obtained by five independent techniques, shows something different. In the case of MA, CF-LIBS, AAS and ICP-MS analysis, the Fe/Mg ratio lies in between values typical for L and H chondrites. In the case of LA-ICP-MS analysis, the meteorite specimen even appears to be an LL chondrite. This wide range of Fe/Mg ratio is probably due to variations of FeNi metal in studied specimen. Based on these results and based on the specimen very heterogeneous structure, we believe that the Porangaba meteorite probably originates from a body with rubble-pile structure.

Our calculations (however based on very rough data from several photos and security cameras) indicate that the parent body of Porangaba meteoroid is an unknown object on the outer edge of the main asteroid belt exhibiting orbital resonance 3:1 with respect to the Jupiter.

We also provide a laboratory simulation of meteor spectra emissions that can be used for at least qualitative comparison with spectra from sporadic meteors with similar composition to the Porangaba (L4 Ordinary Chondrite) recorded by high-speed video-cameras equipped with simple grating spectrographs.

Despite the unsatisfactory number of meteorites with known major properties and orbits in the Solar system, in comparison to the total number of observed falls, we believe that with constantly improving observing techniques, the number of these information-rich meteorites will increase rapidly over time and that the Porangaba meteorite is now becoming one of them. Ultimately, the greater the number of these meteorites will be, step by step, the amazing story of the Solar system will become more and more uncovered.

Acknowledgements

The research has been supported by the programme of Regional Cooperation between the Regions and the Institutes of the Czech Academy of Sciences in 2017 (projects no.: R200401721 and R200401521), in 2018 and 2019 (projects no.: R200401721 and R200401801) and ERDF/ESF “Advanced Applied Sciences” (No. CZ.02.1.01/0.0/0.0/16_019/0000778). Support of the Czech Science Foundation within the project reg. no. 18-27653S is acknowledged.

Appendix A. Supplementary data

Supplementary data to this article can be found online at https://doi.org/10.1016/j.icarus.2020.113670.

References

Abe, S., Mukai, T., Hirata, N., Barnouin-jha, O.S., Cheng, A.F., Demura, H., Gaskell, R.W., Hashimoto, T., Hiraoka, K., Honda, T., Kubota, T., Matsuoka, M., Mizuno, T., 2006. Mass and local topography measurements of Itokawa by Hayabusa, 75, 1344–1347.

Afanasiev, V.L., Kalenichenko, V.V., Karachentsev, I.D., 2007. Detection of an Intergalactic Meteor Particle with the 6-M Telescope. https://doi.org/10.1134/s1990341307040013.

Berezhnoy, A.A., Borovicka, J., 2010. Formation of molecules in bright meteors. Icarus 210, 150–157. https://doi.org/10.1016/j.icarus.2010.06.036.

Borovicka, J., 1993. A fireball spectrum analysis. Astron. Astrophys. 279, 627–645.

Borovička, J., Betlem, H., 1997. Spectral analysis of two Perseid meteors. Planet. Space Sci. 45, 563–575. https://doi.org/10.1016/S0032-0633(97)00024-X.

Borovicka, J., Stork, R., Bocek, J., 1999. First results from video spectroscopy of 1998 Leonid meteors. Meteorit. {&} Planet. Sci. 34, 987–994.
Borovicka, J., Spurny, P., Kalenda, P., Tagliaferri, E., 2003. The Moravka meteorite fall: 1. Description of the events and determination of the fireball trajectory and orbit from video records. Meteorit. Planet. Sci. 38, 975–987. https://doi.org/10.1111/j.1945-5100.2003.tb00293.x.
Borovička, J., Spurný, P., Brown, P., Wiegert, P., Kalenda, P., Clark, D., Shrbený, L., 2013. The trajectory, structure and origin of the Chelyabinsk asteroidal impactor. Nature 503, 235–237.
Brearley, A.J., Jones, R.H., 1998. Chondritic meteorites. Planet. Mater. 3.
Brown, P., Ceplecha, Z., Hawkes, R.L., Wetherill, G., Beech, M., Mossman, K., 1994. The orbit and atmospheric trajectory of the Peekskill meteorite from video records. Nature 367, 624–626. https://doi.org/10.1038/367624a0.
Brown, P., Pack, D., Edwards, W.N., ReVelle, D.O., Yoo, B.B., Spalding, R.E., Tagliaferri, E., 2004. The orbit, atmospheric dynamics, and initial mass of the park Forest meteorite. Meteorit. Planet. Sci. 39, 1781–1796. https://doi.org/10.1111/j.1945-5100.2004.tb00075.x.
Bus, S.J., Binzel, R.P., 2002. Phase II of the small main-belt asteroid spectroscopic survey: a feature-based taxonomy. Icarus 158, 146–177.
Ceplecha, Z., 1961. Multiple fall of Pribram meteorites photographed. 1. Double-station photographs of the fireball and their relations to the found meteorites. Bull. Astron. Institutes Czechoslov. 12, 21.
Ciucci, A., Corsi, M., Palleschi, V., Rastelli, S., Salvetti, A., Tognoni, E., 1999. New procedure for quantitative elemental analysis by laser-induced plasma spectroscopy. Appl. Spectrosc. 53, 960–964. https://doi.org/10.1366/0003702991947612.
Collins, G.S., Melosh, H.J., Marcus, R.A., 2005. Earth impact effects program: a web-based computer program for calculating the regional environmental consequences of a meteoroid impact on Earth. Meteorit. Planet. Sci. 40, 817–840. https://doi.org/10.1111/j.1945-5100.2005.tb00157.x.
Cousin, A., Sautter, V., Fabre, C., Maurice, S., Wiens, R.C., 2012. Textural and modal analyses of picritic basalts with ChemCam laser-induced breakdown spectroscopy. J. Geophys. Res. 117 https://doi.org/10.1029/2012JE004132.
De Giacomo, A., 2011. A novel approach to elemental analysis by laser induced breakdown spectroscopy based on direct correlation between the electron impact excitation cross section and the optical emission intensity. Spectrochim. ACTA PART B-ATOMIC Spectrosc. 66, 661–670. https://doi.org/10.1016/j.sab.2011.09.003.
Dell'Aglio, M., De Giacomo, A., Gaudiuso, R., De Pascale, O., Senesi, G.S., Longo, S., 2010. Laser induced breakdown spectroscopy applications to meteorites: chemical analysis and composition profiles. Geochim. Cosmochim. Acta 74, 7329–7339. https://doi.org/10.1016/j.gca.2010.09.018.
Dell'Aglio, M., De Giacomo, A., Gaudiuso, R., De Pascale, O., Longo, S., 2014. Laser induced breakdown spectroscopy of meteorites as a probe of the early solar system. Spectrochim. ACTA PART B-ATOMIC Spectrosc. 101, 68–75. https://doi.org/10.1016/j.sab.2014.07.011.
DeMeo, F.E., Carry, B., 2013. The taxonomic distribution of asteroids from multi-filter all-sky photometric surveys. Icarus 226, 723–741. https://doi.org/10.1016/j.icarus.2013.06.027.
Drouard, A., Vernazza, P., Loehle, S., Gattacceca, J., Vaubaillon, J., Zanda, B., Birlan, M., Bouley, S., Colas, F., Eberhart, M., Hermann, T., Jorda, L., Marmo, C., Meindl, A., Oefele, R., Zamkotsian, F., Zander, F., 2018. Probing the Use of Spectroscopy to Determine the Meteoritic Analogues of Meteors. https://doi.org/10.1051/0004-6361/201732225.
Dunn, T.L., McSween, H.Y., McCoy, T.J., Cressey, G., 2010. Analysis of ordinary chondrites using powder X-ray diffraction: 2. Applications to ordinary chondrite parent-body processes. Meteorit. Planet. Sci. 45, 139–160. https://doi.org/10.1111/j.1945-5100.2009.01012.x.
Ferus, M., 2015. Private Communication with Ing. Lenža and Dr. Borovička.
Ferus, M., Koukal, J., Lenza, L., Srba, J., Kubelik, P., Laitl, V., Zanozina, E.M., Vana, P., Kaiserova, T., Knizek, A., Civis, S., 2017. Recording and evaluation of high resolution optical meteor spectra and comparative laboratory measurements using laser ablation of solid meteorite specimens. In: International Conference on Transparent Optical Networks. https://doi.org/10.1109/ICTON.2017.8024864.
Ferus, M., Koukal, J., Lenža, L., Srba, J., Kubelík, P., Laitl, V., Zanozina, E.M., Váňa, P., Kaiserová, T., Knížek, A., Rimmer, P., Chatzitheodoridis, E., Civiš, S., 2018. Calibration-free quantitative elemental analysis of meteor plasma using reference laser-induced breakdown spectroscopy of meteorite samples. Astron. Astrophys. 610. https://doi.org/10.1051/0004-6361/201629950.
Galimov, E., Kolotov, V.P., Nazarov, M.A., Kostitsyn, Y.A., 2013. Analytical Results for the Material of the Chelyabinsk Meteorite. https://doi.org/10.1134/S0016702913070100.
Gibson, E.K., Lange, D.E., Keil, K., 1977. The Kramer Creek, Colorado Meteorite: A New L4 Chondrite, p. 12.
Gounelle, M., Spurny, P., Bland, P.A., 2006. The orbit and atmospheric trajectory of the Orgueil meteorite from historical records. Meteorit. Planet. Sci. 41, 135–150. https://doi.org/10.1111/j.1945-5100.2006.tb00198.x.
Gradie, J., Tedesco, E., 1982. Compositional structure of the asteroid belt. Science (80-.) 216, 1405–1407.
Gritsevich, M.I., 2008. The Pribram, Lost City, Innisfree, and Neuschwanstein falls: an analysis of the atmospheric trajectories. Sol. Syst. Res. 42, 372–390. https://doi.org/10.1134/S003809460805002X.
Grossman, J., 2015. Porangaba. Meteorit. Bull. Database.
Haramura, H., Kushiro, I., Yanai, K., 1983. Chemical composition of Antarctic meteorites. Mem. Natl. Inst. Polar Res. 30, 109–121.
Hornackova, M., Plavcan, J., Rakovsky, J., Porubcan, V., Ozdin, D., Veis, P., 2014. Calibration-free laser induced breakdown spectroscopy as an alternative method for found meteorite fragments analysis. Eur. Phys. JOURNAL-APPLIED Phys. 66 https://doi.org/10.1051/epjap/2014130465.
Horňáčková, M., Plavčan, J., Rakovský, J., Porubčan, V., Ozdín, D., Veis, P., 2014. Calibration-free laser induced breakdown spectroscopy as an alternative method for found meteorite fragments analysis. Eur. Phys. J. Appl. Phys. 66, 10702 https://doi.org/10.1051/epjap/2014130465.
Jenniskens, P., 2007. Quantitative meteor spectroscopy: elemental abundances. Adv. Sp. Res. 39, 491–512. https://doi.org/10.1016/j.asr.2007.03.040.
Koukal, J., Srba, J., Gorková, S., Lenža, L., Ferus, M., Civiš, S., Knížek, A., Kubelík, P., Kaiserová, T., Váňa, P., 2016. Meteors and meteorites spectra. In: Proc. IMC, pp. 1–6.
Kramida, A., Ralchenko, Yu., Reader, J., 2019. NIST Atomic Spectra Database (ver. 5.7).
Lasue, J., Wiens, R.C., Clegg, S.M., Vaniman, D.T., Joy, K.H., Humphries, S., Mezzacappa, A., Melikechi, N., McInroy, R.E., Bender, S., 2012. Remote laser-induced breakdown spectroscopy (LIBS) for lunar exploration. J. Geophys. Res. 117 https://doi.org/10.1029/2011JE003898.
List of meteorites with a complete "lineage" [WWW document]. In: Seznam meteoritů s rodokmenem Wikipedie - otevřená Encykl, 2019.
Madiedo, J.M., Trigo-Rodriguez, J.M., Konovalova, N., Williams, I.P., Castro-Tirado, A. J., Ortiz, J.L., Cabrera-Cano, J., 2013. The 2011 October Draconids outburst - II. Meteoroid chemical abundances from fireball spectroscopy. Mon. Not. R. Astron. Soc. 433, 571–580. https://doi.org/10.1093/mnras/stt748.
McCrosky, R.E., Posen, A., Schwartz, G., Shao, C.Y., 1971. Lost City meteorite - its recovery and a comparison with other fireballs. J. Geophys. Res. 76, 4090. https://doi.org/10.1029/JB076i017p04090.
Mindat.org, 2016. Porangaba meteorite, Porangaba, São Paulo, Brazil (WWW Document).
Minton, D.A., Malhotra, R., 2009. A record of planet migration in the main asteroid belt. Nature 457, 1109–1111. https://doi.org/10.1038/nature07778.
Nittler, L.R., McCoy, T.J., Clark, P.E., Murphy, M.E., Trobka, J.I., Jarosewich, E., 2004. Bulk element compositions of meteorites: a guide for interpreting remote-sensing geochemical measurements of planets and asteroids. Antarct. Meteor. Res. 233–253.
Ozdin, D., Plavcan, J., Hornackova, M., Uher, P., Porubcan, V., Veis, P., Rakovsky, J., Toth, J., Konecny, P., Svoren, J., 2015. Mineralogy, petrography, geochemistry, and classification of the Kosice meteorite. Meteorit. {&} Planet. Sci. 50, 864–879. https://doi.org/10.1111/maps.12405.
Senesi, G.S., 2014. Laser-Induced Breakdown Spectroscopy (LIBS) applied to terrestrial and extraterrestrial analogue geomaterials with emphasis to minerals and rocks. EARTH-SCIENCE Rev 139, 231–267. https://doi.org/10.1016/j.earscirev.2014.09.008.
Siraj, A., Loeb, A., 2019. Discovery of a Meteor of Interstellar Origin.
SonotaCo, A., 2009. Meteor shower catalog based on video observations in 2007–2008. WGN J. Int. Meteor Organ 37, 55–62.
Stöffler, D., Keil, K., Scot, E.R.D., 1991. Shock Metamorphism of Ordinary Chondrites, p. 55.
Thompson, J.R., Wiens, R.C., Barefield, J.E., Vaniman, D.T., Newsom, H.E., Clegg, S.M., 2006. Remote laser-induced breakdown spectroscopy analyses of Dar al Gani 476 and Zagami Martian meteorites. J. Geophys. Res. 111 https://doi.org/10.1029/2005JE002578.
Tognoni, E., Cristoforetti, G., Legnaioli, S., Palleschi, V., 2010. Review calibration free laser- induced breakdown spectroscopy: state of the art. Spectrochim. Acta Part B At. Spectrosc. 65, 1–14.
Van Der Auwera, J., Bologne, G., Roelandts, I., Duchesne, J.C., 1998. Inductively coupled plasma-mass spectrometric (ICP-MS) analysis of silicate rocks and minerals. Geol. Belg. 1, 49–53.
Welten, K.C., Caffee, M.W., Hillegonds, D.J., Coy, T.J.M., Masarik, J., 2011. Cosmogenic radionuclides in L5 and LL5 chondrites from Queen Alexandra Range, Antarctica: Identification of a large L/LL5 chondrite shower with a preatmospheric mass of approximately 50 , 000 kg 198, 177–198. doi:https://doi.org/10.1111/j.1945-5100.2010.01142.x
Wlotzka, F., 1993. A Weathering Scale for the Ordinary Chondrites. Meteoritics 28, 460.
Zaghloul, M.R., 2004. Reduced formulation and efficient algorithm for the determination of equilibrium composition and partition functions of ideal and nonideal complex plasma mixtures. Phys. Rev. E 69, 26702. https://doi.org/10.1103/PhysRevE.69.026702.

ChemComm
Chemical Communications

Accepted Manuscript

This article can be cited before page numbers have been issued, to do this please use: A. Pastorek, J. Hrncirova, L. Jankovic, L. Nejdl, S. Civiš, O. Ivanek, V. Shestivska, A. Knížek, P. Kubelík, J. Sponer, L. Petera, A. Krivkova, G. Cassone, M. Vaculovicova, J. Šponer and M. Ferus, *Chem. Commun.*, 2019, DOI: 10.1039/C9CC04627E.

This is an Accepted Manuscript, which has been through the Royal Society of Chemistry peer review process and has been accepted for publication.

Accepted Manuscripts are published online shortly after acceptance, before technical editing, formatting and proof reading. Using this free service, authors can make their results available to the community, in citable form, before we publish the edited article. We will replace this Accepted Manuscript with the edited and formatted Advance Article as soon as it is available.

You can find more information about Accepted Manuscripts in the Information for Authors.

Please note that technical editing may introduce minor changes to the text and/or graphics, which may alter content. The journal's standard Terms & Conditions and the Ethical guidelines still apply. In no event shall the Royal Society of Chemistry be held responsible for any errors or omissions in this Accepted Manuscript or any consequences arising from the use of any information it contains.

ROYAL SOCIETY OF CHEMISTRY

rsc.li/chemcomm

View Article Online
DOI: 10.1039/C9CC04627E

COMMUNICATION

Prebiotic Synthesis at Impact Craters: the Role of Fe-Clays and Iron Meteorites

Received 00th January 20xx,
Accepted 00th January 20xx

DOI: 10.1039/x0xx00000x

Adam Pastorek,[a,b] Jana Hrnčířová,[a,c] Luboš Jankovič,[d] Lukáš Nejdl,[e] Svatopluk Civiš,[a] Ondřej Ivanek,[a] Violetta Shestivska,[a] Antonín Knížek,[a,c] Petr Kubelík,[a,f] Jiří Šponer,[g,h] Lukáš Petera,[a,c] Anna Křivková,[a,b] Giuseppe Cassone,[g] Markéta Vaculovičová,[e,†] Judit E. Šponer,[g,h†] and Martin Ferus[a,†]

Besides delivering plausible prebiotic feedstock molecules and high-energy initiators, extraterrestrial impacts could also affect the process of abiogenesis by altering the early Earth's geological environment in which primitive life was conceived. We show that iron-rich smectites formed by reprocessing of basalts due to the residual post-impact heat could induce the synthesis and accumulation of important prebiotic building blocks such as nucleobases, amino acids and urea.

Isotopic analysis and study of fossil microstructures tentatively suggest that emergence of life on our planet dates back to the first few hundred million years of Earth's history (i.e. 4.56 – 3.8 Gya) associated with a decrease of extraterrestrial impact activity.[1-3] This might suggest that chemical and physical processes connected to high energy density plasmas could serve as an important driving force of early chemical evolution.[4]

In our previous works we have shown that high-energy-density events could directly induce a unique radical chemistry that could challenge energetically unfavoured steps in the prebiotic synthesis.[5] Furthermore, impact activity could indirectly influence the direction of these synthetic processes through the enormous mechanical energy of the impacting extraterrestrial bodies. Heat liberated upon hitting the planetary surface could be comparable to that of volcanic activity. It could thus significantly re-shape the geological environment by inducing serpentinization of the surrounding basaltic rocks leading to the formation of iron containing clays.[6] So far, most of the prebiotic chemistry-related studies reported utilization of montmorillonite clays. However, recent works[7] suggest that formation of montmorillonites on the early Earth was likely preceded by that of iron-rich smectites. This indicates that the latter clays could be more relevant targets for prebiotic chemistry studies.

The synthetic potential of formamide as a prebiotic feedstock molecule is exemplified by a series of studies by the Saladino and Di Mauro groups.[8-10] Formamide may serve as an important intermediate in various other synthetic pathways as well.[11, 12] This amide is compatible with the ancient geochemistry of our planet[13] and its chemistry can be tuned by the addition of diverse minerals.[8] In particular, it has been demonstrated that rock serpentinization processes could be coupled with the formamide-based synthesis of a series of important compounds relevant to prebiotic chemistry.[14, 15] In our previous study we have found that •CN radicals created during extraterrestrial impacts, when reacting with the cold formamide environment, are able to trigger the formation of all four canonical RNA nucleobases in a one-pot chemistry.[5, 16] The yield of these reactions can be enhanced by clays.[5] In the current work we show that a post-impact formamide chemistry involving iron-rich smectites could follow this direct impact plasma-induced prebiotic synthesis. These processes could be enabled by the residual heat liberated in the impact event in the presence of a suitable catalytic material formed by alteration of basaltic rocks or iron-rich impact structures.

We have designed 10 different experiments (see Table 1) combining various clays (for description see the Electronic Supplementary Information), the Ni/Fe meteorite Campo del Cielo, and Fe_2O_3. A particular emphasis was put on the choice of the clay form. We have considered an Fe-smectite as well as Na- and H-form montmorillonites. The structure of the selected

[a] J. Heyrovský Institute of Physical Chemistry, Czech Academy of Sciences, Dolejškova 3, 182 23 Prague 8, Czech Republic
[b] Faculty of Nuclear Sciences and Physical Engineering, Czech Technical University in Prague, Břehová 78/7, 115 19 Prague 1, Czech Republic
[c] Charles University in Prague, Faculty of Science, Chemical Institute, Hlavova 2030/8, 128 00 Prague 2, Czech Republic
[d] Institute of Inorganic Chemistry, Slovak Academy of Sciences, Dúbravská cesta 9, 845 36 Bratislava 45, Slovak Republic
[e] ÚCB AF, Mendel University in Brno, Zemědělská 1, 613 00 Brno, Czech Republic
[f] Institute of Physics, Czech Academy of Sciences, Na Slovance 1999/2, 182 21 Prague 8, Czech Republic
[g] Institute of Biophysics of the Czech Academy of Sciences, Královopolská 135, 612 65 Brno, Czech Republic
[h] Regional Centre of Advanced Technologies and Materials, Palacky University, 17. listopadu, 771 46 Olomouc, Czech Republic.
† Corresponding authors. E-mails: martin.ferus@jh-inst.cas.cz (MF), marketa.vaculovicova@mendelu.cz (MV), judit@ncbr.muni.cz (JES)
Electronic Supplementary Information (ESI) available: detailed description of the experiments, characterization of the clays used, description of the analytical techniques used for detection of reaction products. See DOI: 10.1039/x0xx00000x

Fe-clay fundamentally differs from the two montmorillonites because it contains iron incorporated in octahedral framework positions, essentially substituting for Al atoms. Montmorillonites were chosen because prior to us most of the prebiotic chemistry experiments were mainly conducted with this smectite clay family.[17-20] In some of the experiments we have considered various mixtures of clays with the Ni/Fe meteorite and Fe_2O_3 powder in order to see the combined effect of terrestrial/extraterrestrial materials on the studied chemistry.‡

When treating 0.1 g of clay with 2 ml of formamide at 160 °C for 24 hours (see the Electronic Supplementary Information for details on the experimental setup) a wide palette of prebiotically relevant substances has been detected by GC-MS and capillary electrophoresis: all the canonical RNA nucleobases, as well as non-canonical nucleobases (like hypoxanthine and purine), the amino acid glycine, urea and guanidine (see Table 1). It is noteworthy to mention that among nucleobases Fe-containing catalysts particularly promote the synthesis of purine and adenine hinting at the operation of a massive HCN-based reaction channel. Further, Ni/Fe catalysts alone or to a lesser extent in combination with Fe_2O_3 seem to support the formation of cytosine and uracil. In contrast, the above two catalysts exert an inhibitory effect on thymine formation, whereas clays act in the opposite way. In all experiments HCN, ammonia, and CO were detected among the gas-phase reaction products.

As documented in preceding studies,[5, 18] clay minerals, in general, promote the synthesis of nucleobases. For example, the Na- and H-clays considered in this study lead to a 6-10 fold increase of purine formation as compared to the uncatalyzed case. For guanine, whose thermal synthesis is notoriously inefficient in the absence of catalysts (see experiment **1** in Table 1), catalysis by the Na-clay (see experiment **2** in Table 1) is even more apparent. In general, the catalytic effect of clays is most likely associated with their ability to concentrate the precursor molecules in the interlayer between the aluminosilicate platelets. Our new results point out that Fe-smectites are even better catalysts for nucleobase formation, whereas the overall catalytic effect of Ni/Fe meteorites or Fe_2O_3 on the synthesis of nucleobases is negligible. The latter catalysts, on the other hand, exhibit an unusually high activity at the formation of urea and guanidine, in line with previously reported results.[21] This is at variance with Fe-clays, which clearly inhibit formation of urea and guanidine.

Overall, the product compositions observed in the presence of various iron-containing materials seem to be determined by a subtle balance between three main competing reaction channels shown in Figure 1. As our new data (discussed above) and previous studies on formamide thermolysis[22, 23] illustrate, to a limited extent, these channels are also operational in the

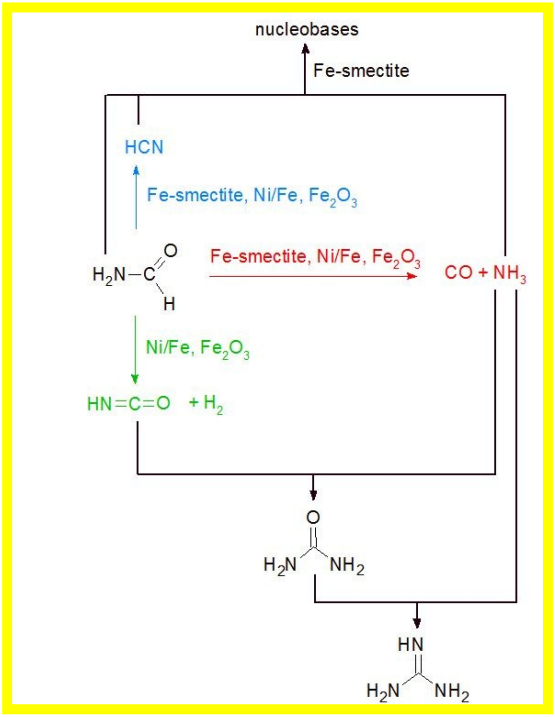

Figure 1. Reaction network of formamide treated at 160 °C for 24 hours in the presence of Fe-clay, Ni/Fe meteorite and Fe_2O_3. The three main dissociation channels (referred to in the text) leading to HCN, CO+NH_3 as well as to HNCO+H_2 are highlighted with blue, red and green colors, respectively.

Table 1: Product compositions after thermal treatment (160 °C, 24 hours) of formamide in presence of various clays, Ni/Fe meteoritic material, Fe_2O_3 and various mixtures thereof. For the gas-phase decomposition products (HCN, NH_3 and CO), we show % vol. as calculated based on the intensity of the absorption lines using calibration standards. Concentration of nucleobases, adenine (A), guanine (G), cytosine (C), thymine (T), uracil (U), purine (P), urea, hypoxanthine (H-X), guanidine (GN), and glycine is expressed in vol. ppm. Products were identified using Fourier transform high resolution infrared spectrometry (FTIR), gas chromatography mass spectrometry (GC-MS) and capillary electrophoresis (CE). Missing number means that the compound was not detected in the analysed sample.

Experiment	1 Formamide	2 Fe-Clay	3 Na-Clay	4 H-Clay	5 Fe-Clay + NiFe	6 Na-Clay + NiFe	7 H-Clay + NiFe	8 NiFe	9 Fe_2O_3	10 Fe_2O_3 + NiFe	Detection Method
HCN	3%	8%	1%	1%	8%	1%	3%	8%	10%	7%	FTIR
NH_3	63%	75%	69%	76%	74%	39%	68%	83%	76%	89%	FTIR
CO	34%	16%	30%	23%	17%	60%	29%	10%	14%	5%	FTIR
A	9	433	30	67	173	159	0.5	23	11	14	GC-MS, CE
G	0.6	11	17	10	7	3		0.2	0.4	0.1	GC-MS
C	10	0.2	16	5	5	12		60	20.0	80	GC-MS
T	19	45	50	51	2	72	56.6				CE
U	41	8	9.5	28	20	16		164		82	GC-MS, CE
P	338	4582	1930	3416	3391	1283	150	531	395	443	GC-MS, CE
H-X	10	56	13	12	21	4.0	2	28	17	15	GC-MS
GN	114		1	8	10		0.5	877	475	1052	GC-MS
Urea	>10000	517	2380	4100	9470	2950	255	25455	19366	20799	GC-MS
Glycine	1	1	0.5	3	0.6	0.3	0.6	2	2	3	GC-MS

View Article Online
DOI: 10.1039/C9CC04627E

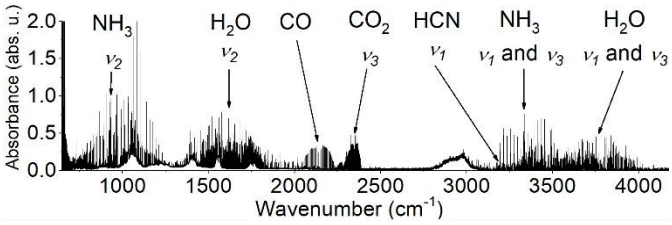

Figure 2. FTIR spectrum of the gas phase reaction products formed when heating formamide (160 °C, 24 hours) in the presence of an Fe-smectite.

absence of catalysts. Our new data suggest that all three iron-containing catalysts (i.e. Ni/Fe meteoritic materials, Fe_2O_3[§] and Fe-smectites) favour the dehydration of formamide to HCN[§§, 24] (blue reaction channel in Figure 1; see Table 1 and the gas-phase spectrum in Figure 2) as well as the parallel formation of NH_3 and CO (red reaction channel in Figure 1). The formidable amount of urea formed in experiments **8**, **9** and **10** (see Table 1) reveals that the third reaction channel, i.e., the dehydrogenation of formamide to HNCO (green reaction channel in Figure 1), is significant only with Ni/Fe meteorites and Fe_2O_3. Accordingly with the latter finding, literature data also support the fact that the Ni(111) surface may catalyse the decomposition of formamide to HNCO.[25] Fe-smectites, on the other hand, are more compatible with a subsequent HCN-related chemistry, which is illustrated by the accumulation of purine and other nucleobases in experiment **2** (see Table 1 and Figure 3).

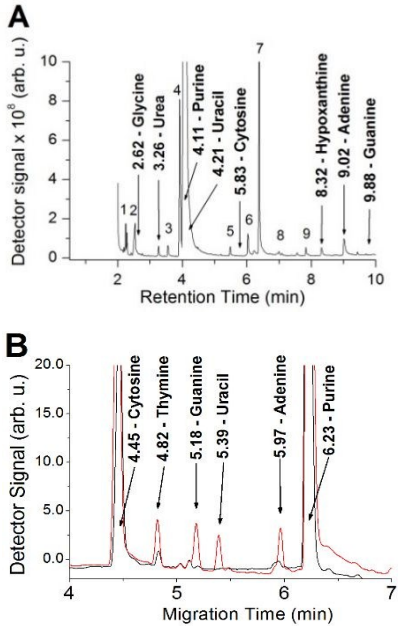

Figure 3. Detection of nucleobases, glycine and urea formed upon thermal treatment of formamide (160 °C, 24 hours) in the presence of Fe-smectites using GC-MS (panel A) and capillary electrophoresis (panel B). Red curve: standard, black curve: sample. For more analytical data see chapter SIV in the Electronic Supplementary Information. The numbered low intensity signals correspond to non-specific by-products of the derivatization reaction.

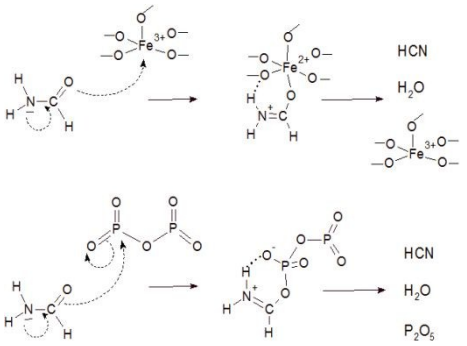

Figure 4. Suggested mechanism for the dehydration of formamide to HCN catalysed by Fe-defects present in the octahedral sheets of Fe-smectites (upper row) and P_2O_5 (lower row, based on Ref. [26]).

Remarkably, formation of nucleobases seems to be more compatible with Fe-smectites than with Na- or H-montmorillonites. Indeed, it has been suggested that the latter two clay forms were much less common in the Earth's crust by the time when life emerged on our planet.[7]

When mixing various forms of montmorillonites with Ni/Fe meteoritic materials, the product composition is determined by the competition of the three above-listed reaction channels. Thus, adding Ni/Fe-meteorites to Fe-montmorillonites clearly shifts the product composition towards urea. By contrast, the overall reactivity is nearly lost when mixing Ni/Fe-meteorites and H-form clays together, most likely because the H-form clays readily bind NH_3 and make the conversion of HNCO to urea impossible. Thus, whilst Ni/Fe meteoritic materials do not seem to directly participate in the synthetic processes leading to the first biological building blocks, they could be involved in the synthesis of guanidine, a prebiotically highly relevant condensing agent derived from urea (see the reaction scheme in Figure 1).

In general, iron-containing clays, Ni/Fe meteorites or Fe_2O_3 exhibited higher catalytic activity in the studied reactions than the iron-free clay forms. Our data clearly demonstrate that the direction of prebiotic synthetic processes is dependent on the binding mode of iron inside the catalytic material. Cationic iron incorporated in the octahedral sheets of Fe-smectites seems to be especially well-suited to catalyse prebiotic synthesis leading to nucleobases, which may be associated with the advantages arising when combining the rich chemistry of the Fe^{2+}/Fe^{3+} redox system[7] with the unique three-dimensional architecture of clay minerals. The latter enables Fe^{3+} centers incorporated in defects of Fe-smectites to behave as Lewis-acidic sites which, similar to P_2O_5[26] or other P-containing organocatalysts,[27] may catalyse the dehydration of formamide to HCN according to the tentative mechanism shown in Figure 4. The clay structure may then catalyse the subsequent reaction steps leading to nucleobase formation due to concentration of the key reactants, i.e. formamide, HCN and NH_3. While HCN does form

in comparable amounts also over Ni/Fe meteorites as well as over Fe_2O_3, due to the lack of the above-mentioned concentration effects, these catalysts fail to structurally support the chemistry required to synthesize more complex molecules than urea or guanidine.

Data presented above clearly suggest that impact reprocessing of the geological environment could finely tune the composition of the prebiotic broth: whilst Ni/Fe meteoritic materials and iron-oxides favour the formation of urea from formamide, Fe-smectites formed upon serpentinization of basaltic rocks[7] are better suited to catalyse an HCN-mediated formamide chemistry. Thus, the change of the geological milieu and the temporary availability of various energy sources could have determined the sequence of synthetic events in the early ages of our planet.

The robustness of a prebiotic synthetic scenario is highly dependent on the versatility of energy sources and reaction routes leading from the reactants to the products.[28] The current results provide a striking example for this variability through the synthesis of nucleobases. This process can be triggered by a radical chemistry[5] in an extraterrestrial impact event as well as by a simple thermal chemistry using impact-altered rocks containing Fe-smectites. Fe-smectites could have been widespread on the early Earth also from rock serpentinization driven by geothermal energy. All these findings point out the importance of mineral catalysis in a formamide-based abiogenesis on our planet.

Financial support from the Czech Science Foundation, grant reg. no. 17–05076S) and ERDF/ESF "Centre of Advanced Applied Sciences" (No. CZ.02.1.01/0.0/0.0/16019/0000778) is greatly acknowledged.

Conflicts of interest

There are no conflicts of interest to declare.

Notes and references

‡ Note that extraterrestrial impacts inevitably led to a massive mixing of terrestrial and extraterrestrial materials during the Late Heavy Bombardment period.

§ Note that metal-oxides are highly relevant to serpentinization processes as well. A recent study illustrates that silica metal-oxide vesicles formed in serpentinizing rocks possess unique catalytic properties and could contribute to the synthesis of a vast range of important prebiotic building blocks, such as nucleobases, amino acids and carboxylic acids.[15]

§§ Note that a popular industrial process used for HCN-synthesis from formamide also utilizes iron salts as a catalyst[24].

1. C. Koeberl, *Elements*, 2006, **2**, 211-216.
2. M. S. Dodd, D. Papineau, T. Grenne, J. F. Slack, M. Rittner, F. Pirajno, J. O'Neil and C. T. S. Little, *Nature*, 2017, **543**, 60.
3. E. A. Bell, P. Boehnke, T. M. Harrison and W. L. Mao, *Proc. Natl. Acad. Sci. U.S.A.*, 2015, **112**, 14518-14521.
4. J. D. Sutherland, *Angew. Chem. Int. Ed.*, 2016, **55**, 104-121.
5. M. Ferus, D. Nesvorný, J. Šponer, P. Kubelík, R. Michalčíková, V. Shestivská, J. E. Šponer and S. Civiš, *Proc. Natl. Acad. Sci. U.S.A.*, 2015, **112**, 657-662.
6. R. M. Hazen, D. A. Sverjensky, D. Azzolini, D. L. Bish, S. C. Elmore, L. Hinnov and R. E. Milliken, *Am. Mineral.*, 2013, **98**, 2007-2029.
7. A. Meunier, S. Petit, C. S. Cockell, A. El Albani and D. Beaufort, *Orig. Life Evol. Biosph.*, 2010, **40**, 253-272.
8. R. Saladino, G. Botta, S. Pino, G. Costanzo and E. Di Mauro, *Chem. Soc. Rev.*, 2012, **41**, 5526-5565.
9. R. Saladino, C. Crestini, F. Ciciriello, S. Pino, G. Costanzo and E. Di Mauro, *Res. Microbiol.*, 2009, **160**, 441-448.
10. R. Saladino, G. Botta, S. Pino, G. Costanzo and E. Di Mauro, *Biochimie*, 2012, **94**, 1451-1456.
11. M. Ferus, F. Pietrucci, A. M. Saitta, A. Knížek, P. Kubelík, O. Ivanek, V. Shestivska and S. Civiš, *Proc. Natl. Acad. Sci. U.S.A.*, 2017, **114**, 4306-4311.
12. M. Ferus, F. Pietrucci, A. M. Saitta, O. Ivanek, A. Kniížek, P. Kubelík, M. Krus, L. Juha, R. Dudzak, J. Dostál, A. Pastorek, L. Petera, J. Hrncirova, H. Saeidfirozeh, V. Shestivská, J. Sponer, J. E. Sponer, P. Rimmer, S. Civis and G. Cassone, *Astron. Astrophys.*, 2019, **626**, A52.
13. N. H. Sleep, *Astrobiology*, 2018, **18**, 1199-1219.
14. R. Saladino, E. Di Mauro and J. M. García-Ruiz, *Chem. Eur. J.*, 2019, **25**, 3181-3189.
15. B. M. Bizzarri, L. Botta, M. I. Pérez-Valverde, R. Saladino, E. Di Mauro and J. M. García-Ruiz, *Chem. Eur. J.*, 2018, **24**, 8126-8132.
16. M. Ferus, S. Civis, A. Mladek, J. Sponer, L. Juha and J. E. Sponer, *J. Am. Chem. Soc.*, 2012, **134**, 20788-20796.
17. J. P. Ferris, *Elements*, 2005, **1**, 145-149.
18. R. Saladino, C. Crestini, U. Ciambecchini, F. Ciciriello, G. Costanzo and E. Di Mauro, *ChemBioChem*, 2004, **5**, 1558-1566.
19. G. Ertem, *Orig. Life Evol. Biosph.*, 2004, **34**, 549-570.
20. L. O. B. Benetoli, H. de Santana, C. T. Zaia, B. V. and D. A. M. Zaia, *Monatsh. Chem.*, 2008, **139**, 753-761.
21. R. Saladino, G. Botta, M. Delfino and E. Di Mauro, *Chem. Eur. J.*, 2013, **19**, 16916-16922.
22. M. Ferus, R. Michalčíková, V. Shestivská, J. Šponer, J. E. Šponer and S. Civiš, *J. Phys. Chem. A*, 2014, **118**, 719-736.
23. F. Cataldo, G. Patanè and G. Compagnini, *J. Macromol. Sci. A*, 2009, **46**, 1039-1048.
24. K. Weissermel and H.-J. Arpe, *Industrial Organic Chemistry*, Wiley-VCH, Weinheim, 2003.
25. Q. Gao, W. Erley, D. Sander, H. Ibach and J. C. Hemminger, *J. Phys. Chem.*, 1991, **95**, 205-211.
26. D. B. Reisner and E. C. Horning, *Org. Synth.*, 1950, **30**, 22-23.
27. S. A. Shipilovskikh, V. Y. Vaganov, E. I. Denisova, A. E. Rubtsov and A. V. Malkov, *Org. Lett.*, 2018, **20**, 728-731.
28. A. Eschenmoser, *Orig. Life Evol. Biosph.*, 2007, **37**, 309-314.

A&A 626, A52 (2019)
https://doi.org/10.1051/0004-6361/201935435

Astronomy & Astrophysics

Prebiotic synthesis initiated in formaldehyde by laser plasma simulating high-velocity impacts

M. Ferus[1], F. Pietrucci[2], A. M. Saitta[2], O. Ivanek[1], A. Knizek[1,3], P. Kubelík[1,4], M. Krus[5], L. Juha[4,5], R. Dudzak[4,5], J. Dostál[4,5], A. Pastorek[1], L. Petera[1,3], J. Hrncirova[1,3], H. Saeidfirozeh[1], V. Shestivská[1], J. Sponer[6,7], J. E. Sponer[6,7], P. Rimmer[8,9], S. Civiš[1], and G. Cassone[6]

[1] J. Heyrovský Institute of Physical Chemistry, Academy of Sciences of the Czech Republic, Dolejškova 3, 18223 Prague 8, Czech Republic
[2] Sorbonne Université, Muséum National d'Histoire Naturelle, UMR CNRS 7590, Institut de Minéralogie, de Physique des Matériaux et de Cosmochimie, IMPMC, 75005 Paris, France
[3] Charles University in Prague, Faculty of Science, Department of Physical and Macromolecular Chemistry, Albertov 2030, 12840 Prague 2, Czech Republic
[4] Department of Radiation and Chemical Physics, Institute of Physics, Czech Academy of Sciences, Na Slovance 1999/2, 18221 Prague 8, Czech Republic
[5] Institute of Plasma Physics, Czech Academy of Sciences, Za Slovankou 1782/3, 182 00 Prague 8, Czech Republic
[6] Institute of Biophysics of the Czech Academy of Sciences, Královopolská 135, 61265 Brno, Czech Republic
e-mail: cassone@ibp.cz
[7] CEITEC – Central European Institute of Technology, Masaryk University, Campus Bohnice, Kamenice 5, 62500 Brno, Czech Republic
[8] University of Cambridge, Cavendish Astrophysics, J.J. Thomson Avenue, Cambridge CB3 0HE, UK
[9] Laboratory of Molecular Biology, Francis Crick Avenue, Cambridge CB2 OQH, UK

Received 8 March 2019 / Accepted 1 May 2019

ABSTRACT

Context. It is well known that hydrogen cyanide and formamide can universally be considered as key molecules in prebiotic synthesis. Despite the fact that formamide has been detected in interplanetary and interstellar environments, other prebiotic species are far more abundant, including, for example, formaldehyde. However, several results indicate that formamide can play the role of important intermediate as well as that of a feedstock molecule in chemical abiogenesis. Diverse recently proposed scenarios of the origins of the first biopolymers show that liquid formamide environments could have been crucial for the formation of nucleobases, nucleosides, and for phosphorylation reactions, which lead to nucleotides.
Aims. Here we report on a wide exploration of the formaldehyde reaction network under plasma conditions mimicking an asteroid descent in an Earth-like atmosphere and its impact.
Methods. Dielectric breakdown using a high-power kJ-class laser system (PALS – Prague Asterix Laser System) along with quantum mechanical, ab initio molecular dynamics, and enhanced sampling simulations have been employed in order to mimic an asteroid impact plasma.
Results. Being more abundant than formamide both in interstellar and interplanetary environments, during the era of early and late heavy bombardment of Earth and other planets, formaldehyde might have been delivered on asteroids to young planets. In the presence of nitrogen-bearing species, this molecule has been reprocessed under plasma conditions mimicking the local environment of an impacting body. We show that plasma reprocessing of formaldehyde leads to the formation of several radical and molecular species along with formamide.
Conclusion. All the canonical nucleobases, the simplest amino acid (i.e., glycine), and the sugar ribose, have been detected after treatment of formaldehyde and nitrogen gas with dielectric breakdown. Our results, supported by quantum mechanical and enhanced sampling simulations, show that formaldehyde – by producing inter alia formamide – may have had the role of starting substance in prebiotic synthesis.

Key words. astrochemistry – astrobiology – molecular processes – plasmas – meteorites, meteors, meteoroids

1. Introduction

The last decade has witnessed the effort made in elucidating the relevance of two parent compounds that have become crucial in the search for the origin of biologically relevant molecules in one-pot synthesis: hydrogen cyanide (HCN; Ferus et al. 2017a; Xu et al. 2017; Civis et al. 2017; Sutherland 2016, 2017; Powner & Sutherland 2011; Powner et al. 2011) and its hydration product, formamide ($HCONH_2$; Sponer et al. 2016; Ferus et al. 2015b, 2017b; Rotelli et al. 2016; Saladino et al. 2012a,b, 2015, 2016). The main sources of HCN are ascribed to the reprocessing of atmospheres degassed from impacting interplanetary matter (Kuwahara & Sugita 2015; Zahnle et al. 2010) by electric discharges, impact plasma (Ferus et al. 2017a), or – since young protostellar objects are rich in cyano-compounds (Oberg et al. 2015; Al-Edhari et al. 2017; Oberg 2016) – also by direct exogenous delivery of complex and volatile cyanides. Instead, formamide has been inter alia identified in

the interstellar environment (Adande et al. 2013; Raunier et al. 2004) including well-known objects, such as the young solar-type protostar IRAS 16293–2422 (Kahane et al. 2013) and the comet 67P/Churyumov-Gerasimenko (Goesmann et al. 2015). Under early Earth conditions, a plethora of chemical pathways directly heading toward the formamide synthesis have been identified. Among them, HCN hydrolysis in sea water (Saladino et al. 2012a), reprocessing of simple Miller reducing atmospheres, such as CH_4, NH_3, H_2O, H_2, (Miller 1953) and CO, CO_2, N_2, NH_3, H_2, H_2O (Abelson 1956), or HCHO and their various combinations (Rode 1999; Saitta & Saija 2014; Ferus et al. 2017b), or even ammonium-formate dehydratation (Sponer et al. 2016), and gamma irradiation of acetonitrile (Adam et al. 2018) hold a key place in the prebiotic chemistry realm.

The analysis of trace elements in a statistically significant number of ancient zircons shows a decreasing trend of the oxygen fugacity more than 3.6 Gyr ago, suggesting therefore that early conditions were reducing (Yang et al. 2014). This discovery is consistent with a scenario proposing terrestrial synthesis of biomolecules under reducing conditions created by specific substances possibly delivered by impacts of extraterrestrial bodies rich in refractory carbonaceous material (Yang et al. 2014; Hashimoto et al. 2007; Ferus et al. 2017a). Besides, explorations on impact degassing show that Earth's early atmosphere was indeed very reducing, rich in H_2 and/or CH_4, regardless of which meteoritic materials accreted independently of the chemical reactions controlling the molecular abundances of the atmosphere (Kuwahara & Sugita 2015; Sponer et al. 2016). However, according to our recent results, such conditions led to the synthesis of large amounts of HCN (Ferus et al. 2017a; Civis et al. 2016b). On the other hand, the quantitative extent of the reducing conditions of the environment is still uncertain and the exact composition of the reducing mixture remains unknown. The recent finding of a wide palette of organic substances (Martins 2011) and biomolecules in chondritic meteorites (Martins et al. 2008, 2015) supports the chemical panspermia hypothesis. Moreover, the environment on early Earth was certainly influenced by the delivery of a wide range of organic substances such as formamide, formaldehyde, and hydrogen cyanide. These compounds might also have played the role either of parent compounds or of intermediates in prebiotic processes (Ferus et al. 2017b; Civis et al. 2017).

In spite of the relevance of the chemistry arising from HCN or formamide (Cassone et al. 2018a; Ferus et al. 2018; Sponer et al. 2016), other plausible scenarios should be investigated in order to identify their likelihood, their potential role in exogenous or endogenous prebiotic synthesis, and their connection to already known mechanisms. As an example, the original simple "Miller molecules" (Miller 1953; Abelson 1956; Miyakawa et al. 2002) can be connected both with an HCN- and a formamide-based chemistry. A mixture of ammonia, carbon monoxide, and water produces formamide as a reactive intermediate in the synthesis of nucleobases and amino acids initiated with plasmas produced by laser radiation, electrical discharges, and very intense electric fields (Saitta & Saija 2014). Albeit a Miller reducing atmosphere containing methane, molecular nitrogen, and carbon monoxide provides similar palettes of nucleobases and glycine, its chemistry is exclusively related to HCN (Civis et al. 2017; Hoerst et al. 2012). In addition, the formation of amino acids in simple Miller mixtures is customarily explained by the Strecker synthesis (Strecker 1850, 1854; Cleaves 2008; Lazcano & Bada 2003; Schlesinger & Miller 1983) which is, in turn, connected with HCN and formaldehyde or also with a cyanamide-HCN chemistry (Parker et al. 2014).

In this study, we present the reaction network stemming from the plasma chemistry of formaldehyde, a plausible prebiotic precursor of amino acids and, more importantly, sugars (Cassone et al. 2018b; Strecker 1854; Fox & Windsor 1971; Cleaves 2008). The simplest aldehyde is highly relevant to the composition of the primordial environment on early Earth and it is typically far more abundant than formamide in several interstellar objects, as displayed in Table 1. Formaldehyde has also been identified as a sizable component of carbonaceous chondrites and cometary refractory material (Bernstein et al. 1995) and it represents a possible precursor of the sugar compounds discovered in C-meteorites (Cooper et al. 2001). According to the theory of RNA world (Gilbert 1986) nucleobases ribose and phosphate are the basic compounds for the formation of the first living structures as early (Bell et al. 2015; Mojzsis et al. 1996) as 4.28 Gyr ago (Dodd et al. 2017). In our previous study (Civis et al. 2016a; Ferus et al. 2008), we demonstrated that synthesis of ribose from formaldehyde can be initiated by asteroid impact plasma. In this study we focus on the one-pot synthesis of nucleobases starting with the reprocessing of formaldehyde upon nitrogen atmosphere in high-energy-density events – such as an asteroid or cometary impact in a planetary atmosphere – using the kJ-class laser system PALS (Prague Asterix Laser System; Jungwirth et al. 2001) delivering in this experiment a pulse energy of up to 150 J. In conjunction with quantum chemistry calculations and enhanced sampling simulations, here we answer fundamental questions on the formaldehyde plasma chemistry and the resulting formation of biologically relevant molecules.

2. Methods

Here we explore $HCHO + N_2$ plasma chemistry using a wide range of experimental (and computational) techniques. A solution of formaldehyde was irradiated upon a nitrogen atmosphere by a high-power laser. The resulting gas phase was analyzed using Fourier transform infrared (FTIR) absorption spectrometry, whilst the residua after evaporation of water under vacuum were analyzed by means of gas chromatography-mass detection (GC-MS) spectrometry. In order to monitor simple dissociation fragments of formaldehyde, we employed high-resolution time-resolved FTIR emission spectrometry and high-resolution optical emission spectrometry (OES). Again, the resulting stable discharge products trapped in liquid nitrogen were analyzed using FTIR absorption spectrometry. Finally, the formation of important products was investigated using advanced quantum chemical calculations and compared with experimental results. Details of all these procedures are described below.

2.1. Laser-produced plasma experiments

These experiments have been conducted using a glass irradiation cell equipped with a Pyrex window with a diameter of 10 cm, filled with 1 ml of formaldehyde solution in water (reagent grade, Sigma Aldrich) and 1 atm of inert nitrogen gas. The sample was subsequently transferred to PALS and irradiated by a sequence of 25 single laser pulses (a pulse duration of 350 ps, a wavelength of 1315.2 nm, an energy of 150 J) in the presence of a wide range of catalytic materials (neat formaldehyde solution in water, in the presence of montmorillonite clay, anatase titanium dioxide, and a sample of basaltic rock). The diameter of the laser beam behind the fourth amplifier was 15 cm.

Table 1. Column density N_{tot} expressed in cm^{-2} of formamide and formaldehyde in several interstellar objects and the Halle Bopp comet.

Object	H_2 (cm^{-2})	$HCONH_2$ N_{tot} (cm^{-2})	HCHO N_{tot} (cm^{-2})	HCHO/$HCONH_2$ ratio	Ref.
Orion KL Compact Ridge	1.00×10^{24}	4.70×10^{13}	4.10×10^{16}	872	a,b
NGC 7538 Bubble Nebula	1.00×10^{23}	4.80×10^{12}	2.00×10^{14}	42	a,c
G34.3 Nebula	5.00×10^{23}	1.20×10^{13}	1.30×10^{14}	11	a,d
W3(OH) Emission Nebula	1.00×10^{23}	3.30×10^{12}	1.66×10^{14}	50	a,e
DR21(OH) Cloud	1.00×10^{23}	1.10×10^{12}	4.00×10^{14}	364	a,f
SgrB2 N Cloud Core	3.00×10^{24}	1.70×10^{14}	1.60×10^{15}	9	a,g
W33A Protostar	2.00×10^{23}	1.00×10^{13}	4.00×10^{17}	40 000	a,h
Hale Bopp Comet	1.00×10^{19}	2.00×10^{15}	1.10×10^{17}	55	a,i

References. a: Adande et al. (2013), b: Mangum et al. (1990), c: Downes & Wilson (1974), d: Thompson et al. (1999), e: Cohen (1984), f: Forster et al. (1981), g: Halfen et al. (2006), h: Bernstein et al. (1995), i: Bockelee-Morvan et al. (2000).

One pulse was delivered every 25 min. The laser beam was focused using a CaF_2 lens to achieve an output intensity of approximately 10^{14}–10^{16} W cm^{-2}. The experiment mimics the high-density energy plasma in an asteroid impact (plasma temperature of 4500 K, shock wave, emission of energetic photons, especially UV and XUV radiation, and charged particles). FTIR inspection of the gaseous samples was performed using high-resolution Fourier transform infrared (HR-FTIR) spectra of the vapor phase. They were measured in a multipass White cell reaching an optical path of 35 m. The cell was interfaced to a sealable glass vacuum line used for the transfer of the gaseous and volatile phase from the irradiation cell. The spectrometer Bruker IFS 125 HR was subsequently evacuated and operated in the measurement mode from 650–5500 cm^{-1} using a HgCdTe nitrogen cooled detector and a KBr beamsplitter. Three hundred scans were acquired with 40 kHz scanning mirror speed with a resolution of 0.02 cm^{-1}. The measured interferograms were apodized with the Blackmann–Harris apodization function. The discharge products from the following experiments have been also analyzed using the same procedure after evaporation from the liquid nitrogen trap.

2.2. Discharge experiments

Discharge experiments have been conducted in a glow discharge emission cell for spectroscopic monitoring of unstable products using time-resolved spectroscopy. The principles of the method have been discussed in our previous papers (Ferus et al. 2011a,b; Civis et al. 2012a,b,c,d, 2013). Briefly, a mixture of formaldehyde vapors with nitrogen buffer gas was led to a positive column discharge tube equipped with CaF_2 windows. The emission spectra from discharge plasma in different gas mixtures were observed with the time-resolved Fourier transform high-resolution Bruker IFS 120 HR interferometer. The AC discharge was maintained by a high-voltage transistor switch HTS 81 (Behlke electronic GmbH, Frankfurt, Germany) applied between the stainless steel anode and the grounded cathode. The plasma was cooled by liquid water in the outer jacket of the cell. The voltage drop across the discharge was 1000 V, with a pulse width of 22 μs and 0.6 A peak-to-peak current. The scanner velocity of FTS was set to produce a 10 kHz He–Ne laser fringe frequency, which was used to trigger the discharge pulse. The recorded spectral range was 1800–4000 cm^{-1} with an optical filter, at an unapodized resolution of 0.02 cm^{-1}. Fifty scans were averaged to obtain a reasonable signal-to-noise ratio. The initial pressure was varied from 1 to 10.0 Torr. The detection of highly excited atomic, radical, or ionic products in the range of UV-Vis spectra was also covered by high-resolution emission spectroscopy. During the discharge process, an optical cable with a built-in mirror was used to record the emission from the discharge cell by the high-resolution UV–Vis spectrometer Echelle ESA 4000. Such an apparatus makes it possible to measure the emission spectra in the interval 200–800 nm, that is, from the middle ultraviolet range to the beginning of the near infrared region with spectral resolution ranging from 0.005 nm (200 nm) to 0.019 nm (780 nm).

2.3. Detection of biologically relevant organic molecules

Gas chromatography-mass detection spectrometry analysis of the non-volatile fraction of the products formed upon irradiation with a high-power laser was conducted after filtration of the liquid sample extracted from the irradiation cell. The filtrates were evaporated under vacuum inside a vial vessel and analyzed for the presence of nucleobases and glycine. The measurements were performed using an ITQ 1100 GC-Ion Trap MS system (ThermoScientific, USA), equipped with an Xcalibur MS Platform using a non-polar TG-SQC column (ThermoScientific, USA). The dried solid residue was derivatized for 120 min at 110°C in 240 μl of pyridine aprotic reaction solvent (99.9%, Sigma Aldrich) and N-(tert-butyldimethylsilyl)-N-methyl-trifluoroacetamide (99% MTBSTFA, CAS 77377-52-7, Sigma Aldrich) at a ratio of 3:1. After the derivatization process, 1 μl of derivative was injected into the nonpolar column TG–5MS of a Trace 1300 Series gas chromatograph equipped with a mass detector MS 1100 ion trap and analyzed using a temperature gradient 10°C min^{-1} in the range of 180–280°C. Chromatograms and mass spectra have been compared with standards of uracil (U), thymine (T), cytosine (C), adenine (A), guanine (G), urea, and glycine (GL).

2.4. Quantum chemical calculations, ab initio molecular dynamics, and enhanced sampling simulations

In this study, two chemical reactions were simulated by means of traditional quantum-based calculations as well as finite-temperature ab initio molecular dynamics (AIMD) coupled with enhanced sampling techniques. In particular, the following gas-phase reactions were investigated:

$$HCHO + HCN \rightarrow HOCH_2CN \quad (1)$$

$$HCHO + NH_3 \rightarrow HCONH_2 + H_2. \quad (2)$$

Static zero-kelvin calculations of the thermochemistry of these reactions were carried out with the Orca software package (Frank 2012). The following assumptions hold within these traditional quantum-based thermochemistry calculations: (1) the electronic state is orbitally nondegenerate; (2) there are no thermally accessible electronically excited states; (3) all vibrations are strictly harmonic. In this way, by employing the hybrid meta exchange and correlation functional PW6B95 (Zhao & Truhlar 2005), the different energetic and (approximate) entropic contributions characterizing those reactions have been determined at 300 K, 650 K, and 4500 K. Moreover, Grimme's D3 dispersion corrections (Grimme et al. 2010, 2011) with Becke–Johnson (BJ) damping have been taken into account, whereas a gaussian basis set of quadrupole zeta valence quality (def2-QZVP; Weigend & Ahlrichs 2005) has been chosen along with the def2/J auxiliary basis set (Weigend 2006).

With the aim of disclosing the reaction pathways and transition states (TSs) through a more accurate treatment

of the entropic contributions, also finite-temperature Born-Oppenheimer (BO) molecular dynamics (MD) simulations combined with enhanced-sampling metadynamics (MetD) techniques (Laio & Parrinello 2002; Pietrucci & Saitta 2015) have been performed. In such a way, estimates of the free energy barriers characterizing the investigated processes can be evaluated by more appropriately including the entropic contributions as well (Pietrucci 2017; Cassone et al. 2017a,b). AIMD simulations were carried out using the software suite CP2K (Hutter et al. 2014) in conjunction with PLUMED-2.3 (Tribello et al. 2014), a patch that allows for enhanced sampling calculations. Cubic simulation cells of sides equal to 9.9 Å were built in order to reproduce the gas-phase behavior of reactions (1) and (2) by employing typical atomic-based (gaussian) basis sets (i.e., TZVP). Goedecker–Teter–Hutter (GTH; Goedecker et al. 1996) pseudopotentials were adopted whereas exchange and correlation effects were handled by means of the BLYP functional (Becke 1988; Lee et al. 1988) along with Grimme's D3(BJ) dispersion corrections (Grimme et al. 2010, 2011) in MetD simulations. A time step equal to 0.5 fs was set. The temperature was controlled by means of the stochastic velocity rescaling method (Bussi et al. 2007) with a time constant equal to 2 fs. Parallel runs employing different heights of the bias were performed at 650 K for reactions (1) (see Fig. A.1 of the Supporting Information (SI) file) and (2). Once the most appropriate height of the applied bias was identified, three parallel simulations were executed, stopping them immediately after the occurrence of the reaction, in order to obtain from the final bias potential an estimate of the free-energy barriers along with their respective error bars as dispersion of the equivalent simulations (see, e.g., Fig. A.2). The dynamics of ions was simulated classically using the Verlet algorithm.

The MetD formalism here adopted employs the matrices of coordination numbers with the aim of defining a given molecular state, and exploits path-CV MetD (Branduardi et al. 2007; Pietrucci & Saitta 2015), based on two collective variables (CV), S and Z, on which the free-energy surface is constructed. The former variable represents the progress along the chemical transformation whereas the latter represents the distance from the predefined (idealized) pathway. In our case, however, only the reactants' and the products' reference structures have been employed to define the chemical path of each of the investigated reactions. This way, no prejudice on the chemical route undertaken by the systems is introduced. During the calculations, the following parameters have been adopted for the coordination function (see Eq. (3) of Pietrucci & Saitta 2015): $N = 6$, $M = 12$, $R^0_{SS'} = 1.8$ Å for $S, S' = \mathrm{O, C, N}$, 1.5 Å for $S = \mathrm{O, C, N}$, $S' = \mathrm{H}$, and 1.4 Å for $S = S' = \mathrm{H}$. In particular for reaction (1), the oxygen, the two carbon, and the nitrogen atoms have been selected in order to identify the reactants and the product states whereas, for reactions (2), the oxygen, the carbon, the nitrogen, and one hydrogen belonging to the formaldehyde molecule have been included for the coordination matrices. The parameter λ has been set such that $\lambda D(R_1, R_2) \sim 2.3$ (where R_1 and R_2 are the reference configurations) in order to obtain a smooth free energy landscape. The MetD potential was composed of gaussians with widths of $\sigma_s = 0.02$ and $\sigma_z = 0.10$, whereas different gaussian heights (i.e., equal to 2.4, 4.8, and 7.2 kcal mol^{-1}) deposed every 50 fs (i.e., every 100 MD steps) have been tested.

In order to characterize the TSs of the reactions, committor analysis (Bolhuis et al. 2002) has been performed. By choosing dozens of structures along reactive pathways that were considered as plausible candidates for being the TS of each 'reaction, 50 unbiased trajectories of 300 fs each, differing for the initial random velocities, were performed. We have identified a configuration as belonging to the TS ensemble when it is committed to the reactants or products basin with a probability of $50 \pm 5\%$.

3. Results and discussion

3.1. Simple products of formaldehyde decomposition

In order to describe the main decomposition channels of formaldehyde in the presence of nitrogen under plasma conditions, emission spectra of glow electric discharge have been recorded using OES by the high-resolution Echelle spectrograph and FTIR time-resolved spectrometer. Stable products were trapped in liquid nitrogen and, after their evaporation into a multipass cell, absorption spectra were measured using a high-resolution FTIR spectrometer. The OES and FTIR survey of HCHO decomposition products in electric discharge is depicted in Fig. 1 (panels A and B) whilst FTIR absorption spectra are shown in panel C.

Besides atomic emission lines of H–C–O–N, OES shows that the main dissociation product of formaldehyde in the presence of nitrogen is carbon monoxide. HCO radical, as the most probable primary decomposition product, was detected neither by OES nor by time-resolved FTIR. However, this decomposition channel of formaldehyde is well known and our results, as well as a survey of kinetics (Manion et al. 2015), show that under specific conditions of glow discharge plasma, HCO is naturally quickly decomposed into CO or, alternatively, reacts forming OH or CH. Moreover, as depicted in the scheme of the main formaldehyde decomposition pathways supplied in Fig. 2 (panel A), also other intermediates can be involved in the underlying reaction network. Using FTIR spectrometry, we have also detected CN and HCN-HNC as major products of the formaldehyde decomposition in presence of N_2. Both species can be clearly formed in radical chemistry, whereas the initiation step is likely the formaldehyde transformation into CH and its further collision with atomic nitrogen. Using absorption FTIR spectroscopy, strong bands of CO_2, C_2H_2, and NH_3 have also been recorded. In particular, HCN and NH_3 may play a crucial role in the further reprocessing of formaldehyde and its decomposition products into molecules that are relevant for the synthesis of the major building blocks of biomolecules, as discussed in detail in the following sections and depicted in Fig. 2 (panel B). Among the major channels of formaldehyde decomposition under plasma conditions in the presence of N_2, we mainly focused on the investigation of formamide formation and the synthesis of glycolonitrile. We selected three main mechanisms highlighted in Fig. 2 (panel A) in red arrows and marked R1 for glycolonitrile and R2 and R3 for formamide. The synthesis was investigated by means of an accurate laboratory simulation of the hypervelocity impact using terawatt-class high-power lasers.

3.2. Impact plasma reprocessing and formamide synthesis

As mentioned in the Introduction, formaldehyde represents a ubiquitous species in disparate environments in the Universe. In almost all of them, it is far more abundant than formamide, a well-known precursor of a wide range of biologically relevant molecules. We should mention that this molecule contains all the basic bio-macroelements and exhibits a reasonable stability and a good reactivity for prebiotic synthesis starting with its

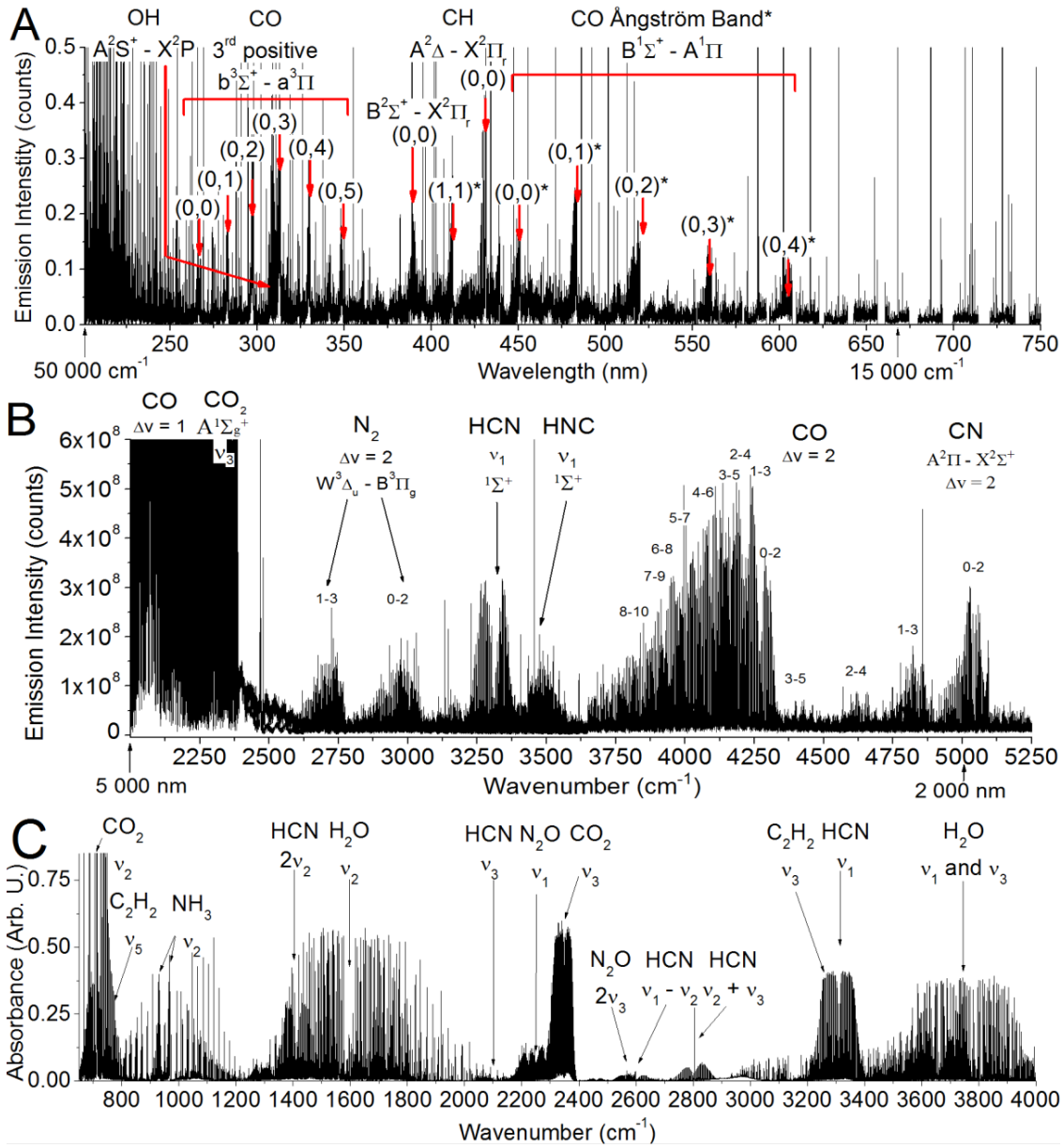

Fig. 1. Spectroscopic survey of HCHO + N_2 glow electric discharge plasma in spectral ranges of optical and near together with middle ultraviolet emission (*panel A*), shown in nanometer scale, and middle infrared emission (*panel B*), shown in cm^{-1} scale. In this figure, we show appropriate spectral units commonly used in each particular region; corresponding wavenumbers and wavelengths are also illustrated for both spectral ranges. Dominant molecular and radical emission bands belong to •OH, CO, •CH, •CN, N_2, CO_2, HCN, HNC species (Okabe 1970; Nemes et al. 2000; Camacho et al. 2008; Rothman et al. 2013; Civis et al. 2008, 2016b). Panel C depicts FTIR absorption spectra of discharge products trapped in the liquid nitrogen trap. Besides HCN and CO_2, NH_3, C_2H_2, H_2O, HCOOH, and N_2O molecules are additionally detected.

condensed-phase exposition to heat (Saladino et al. 2001, 2007), UV irradiation (Barks et al. 2010; Botta et al. 2017), electric discharges (Saitta & Saija 2014), radioactivity (Saladino et al. 2015, 2017; Ferus et al. 2015a), or asteroid impact shock waves (Ferus et al. 2012, 2015a). On the other hand, formaldehyde does not contain nitrogen and, for any further prebiotic synthesis, the nitrogen atom has to be included in the reaction chains. The situation is very similar to the synthesis based on hydrogen cyanide, where the lack of oxygen requires that the latter atom enters reactions of prebiotic synthesis, for example, through water molecules (e.g., Civis et al. 2017 and references therein). On early Earth, in principle, one might consider two major inorganic sources of nitrogen: molecular nitrogen N_2 and ammonia NH_3. In our study, we focus on the exploration of atmospheric N_2 reactivity, whereas as a plausible source of HCHO we shall consider exogenous delivery from comets or asteroids.

The impact of an extraterrestrial body rich in formaldehyde into atmospheres containing N_2 produces hot air glow plasma, ablation of the descending body, generation of shock waves, and considerable reprocessing of all chemical species. The descending body is surrounded by excited atomized gas and reactive radicals (Borovicka & Berezhnoy 2016; Berezhnoy & Borovicka 2010). Almost independently of the mass of the body, the spectra of meteors, bright heavy bolides and presumably also asteroids, exhibit temperatures ranging from 4000 to 6000 K, mainly depending on their velocity (Jenniskens et al. 2004). The typical value is T = 4500 K at a velocity of 25 km s^{-1}. The chemical consequences of such harsh

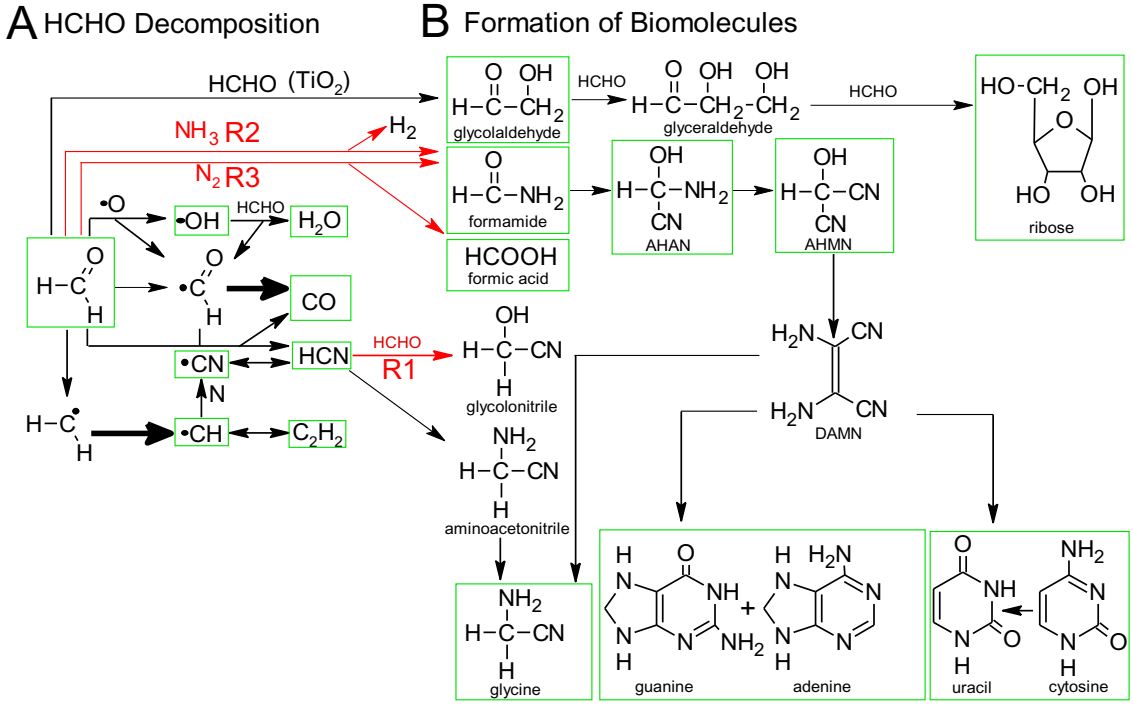

Fig. 2. *Panel A*: reprocessing of HCHO in plasma upon a nitrogen atmosphere. *Panel B*: further formation of basic substances of the RNA genetic code. Particular reactions indicated in *panel A* are listed in the database NIST (Manion et al. 2015) whereas formation of biomolecules is described in, for example, Menor-Salvan & Marin-Yaseli (2012).

and very specific conditions can be simulated under strictly controlled laboratory conditions only if we adopt several approaches and simplifications. The process of micrometeorite impact is usually simulated by supersonic guns, which do not allow the simulation of air glow plasma. Moreover, the typical velocity of projectiles fired by these systems reaches 10 km s^{-1}. This value, however, represents the lower limit of the velocities reached on orbital or collision trajectories of interplanetary matter. On the other hand, according to our explorations of laser plasma physical chemistry, high-power lasers are able to simulate air glow plasma very well. The typical excitation temperature of atomized gas in a fireball generated by the high-power iodine laser PALS, reaches 4500 K, a value close to that of the meteor plasma air glow. The laser pulse also generates considerable shock waves in the gaseous medium and the energy delivered in one 300-ps pulse reproduces the energy released by a small (about 1 m in diameter) impacting body. Moreover, this kind of experiment offers controlled laboratory conditions, a vacuum sealed reaction vessel, a fast survey of spectra, and the further exploration of solid residua for the possible presence of biologically relevant organic molecules after a series of laser-induced shocks.

After a sequence of 25 150-J-laser pulses (delivering a total energy of 3750 J), the gas phase over a formaldehyde-water solution upon nitrogen atmosphere was inspected by high-resolution FTIR spectrometry. Our analysis shows that HCHO is reprocessed into simple molecular products such as carbon monoxide, carbon dioxide, methanol, acetylene, and nitrous oxide. The corresponding absorption spectrum is shown in Fig. 3 (panel A). In comparison with the purely gaseous phase experiments conducted upon pulsed electric discharges conditions presented in the previous section, hydrogen cyanide was not detected. However, the present results suggest that the latter molecule must be formed as an intermediate in laser-produced plasma similarly to the scheme supplied in Fig. 2 (panel A). HCN should have been dissolved in the formaldehyde solution and should have reacted with glycolonitrile, as indicated in Fig. 2 (panel B). HCN is formed not only by the decomposition of formaldehyde, as suggested by the results emerging from pulsed electric discharge experiments, but together with a CN radical, which also plays a role in the formation as well as in the decomposition of all the products involved in the prebiotic chemical pathways shown in Fig. 2 (panel B). In the same panel, species indicated by green frames have been detected after laser pulse treatment of formaldehyde solutions in water upon a nitrogen atmosphere.

In the processes following the formaldehyde decomposition, we observed the formation of 2-amino-2-hydroxy-acetonitrile (AHAN) and 2-amino-2-hydroxy-malononitrile (AHMN; Ferus et al. 2012) detected as an important product of the reaction between formamide and CN-radical. These intermediates play a relevant role in the formation of all the canonical RNA nucleobases under high-energy-density conditions, as explained in detail in our previous papers (Ferus et al. 2012, 2015b) and as schematically depicted in Fig. 2 (panel B). In addition, formamide has also been identified among the reaction products of the formaldehyde decomposition. The absorption spectra of AHAN and AHMN are magnified in Fig. 3 (panel B). The absorption band of the formamide dimer, typically formed under laser plasma conditions (Ferus et al. 2012) from the formamide monomer, is depicted in Fig. 3 (panel C). Although several results have demonstrated that formamide exhibits a very strong tendency to form noncovalent (H-bound) dimers even in gas phase, our observations repeatedly show that formamide does not form dimers in the gas phase without exposition to laser spark, heat, or freezing by liquid nitrogen. Therefore, we expect that the observation of formamide in its dimer form proves – independently – that this molecule is a de novo product of the plasma chemistry taking place on surfaces exposed to the expanding laser plasma fireball. Finally, we stress here the importance of

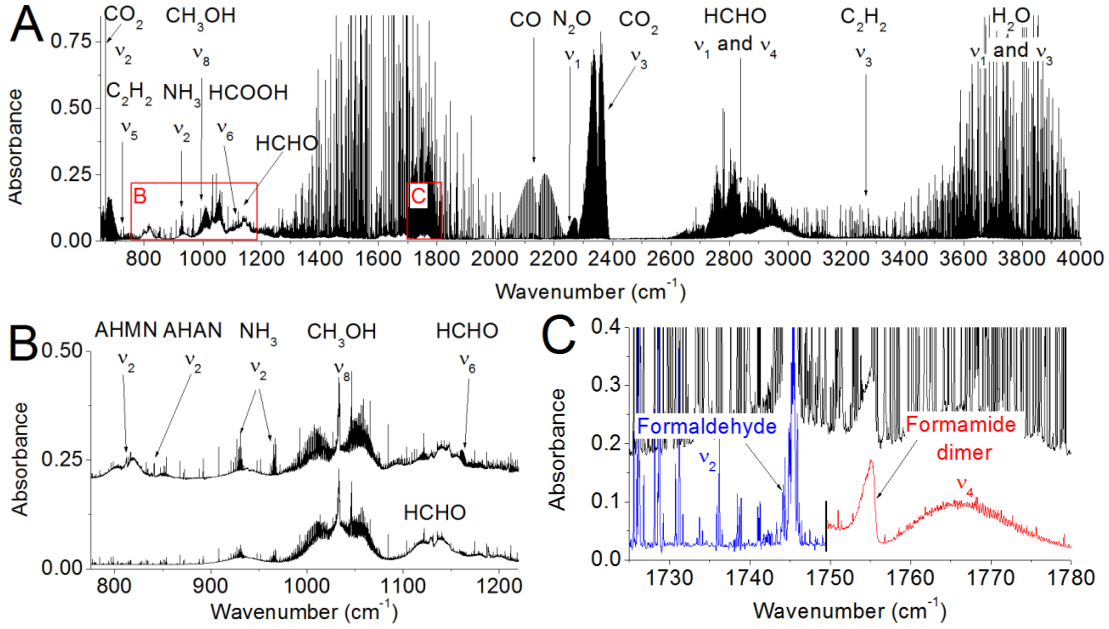

Fig. 3. *Panel A*: high-resolution FTIR absorption spectroscopy survey of formaldehyde treated in the presence of montmorillonite by the action of plasmas formed by laser-induced dielectric breakdown (LIDB). Rectangles B and C: spectral range of AHMN, AHAN, and formamide dimer vibration bands magnified in the *panels B and C*, respectively.

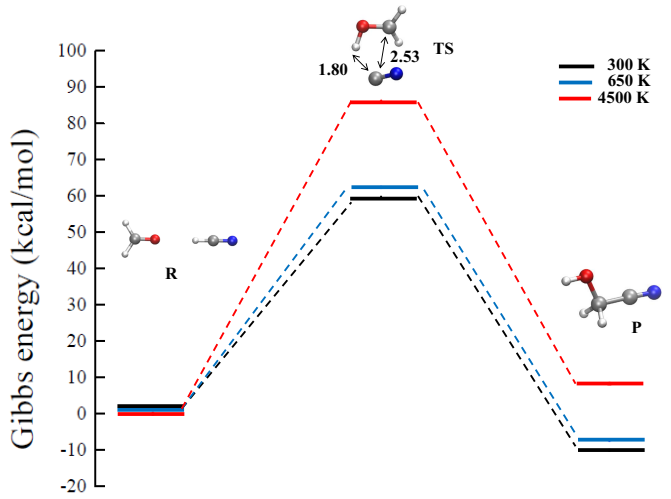

Fig. 4. Gibbs energy of reaction (1) determined through the hybrid meta exchange and correlation functional PW6B95 and Grimme's D3(BJ) dispersion corrections. Some distances (in Å) characterizing the TS are shown.

the role held by surfaces. In fact, in purely gas phase chemistry, we expect that the preferred formation of neat, simple molecular gases follows those depicted in the spectra shown in Figs. 1 and 3 (panel A), as described in Fig. 2 (panel A).

3.3. Chemistry network studied by quantum chemical calculations, ab initio molecular dynamics, and metadynamics simulations

3.3.1. Channel 1: HCHO + HCN → $HOCH_2CN$

In order to elucidate the energetics underlying the chemical conversion of formaldehyde and HCN into glycolonitrile ($HOCH_2CN$) (i.e., reaction (1)), static quantum-based techniques have been firstly employed. This way, the Gibbs energy of the reactants (R), the TS, and the product (P) of reaction (1) has been evaluated, as shown in Fig. 4. Although at standard (300 K) and moderately high temperatures (650 K) glycolonitrile is more stable than HCHO + HCN, at extreme temperature regimes (4500 K) a stability inversion between the reactants and the product has been observed. In fact, whereas the reactants are less stable than the product by 10.1 kcal mol^{-1} and 7.4 kcal mol^{-1} at 300 K and 650 K, respectively, they become more stable by 8.2 kcal mol^{-1} at 4500 K. Glycolonitrile, representing hence a reactive molecule at high temperature regimes, is indeed not detected during the experiments and is likely employed as a means for the further complexification of the sample. At the same time, a sizable decrease of the barrier height – rescaled by $k_B T$ – of reaction (1) has been recorded when the temperature increases. In fact, although an absolute Gibbs energy barrier of 59.8 kcal mol^{-1} and 62.3 kcal mol^{-1} characterizes the reaction at 300 K and 650 K, respectively, an energetic supply of 86.0 kcal mol^{-1} has to be invested in order to trigger the reaction at 4500 K. Once rescaled, these values indicate that the barrier height at 4500 K is ten times lower than that at 300 K, whereas the barrier at 650 K is two times lower than that at room temperature. On the other hand, these activation energies are mainly due to the fact that HCN is a weak acid and the TS is an energetically unfavored zwitterion. Incidentally, the plot of Fig. 4 is in qualitative agreement with the Hammond–Leffer postulate.

Albeit the electronic structure has been characterized by means of a recent hybrid meta exchange and correlation functional developed for thermochemistry and thermochemical kinetics (i.e., PW6B95; Zhao & Truhlar 2005 and in the presence of a properly large basis set, it is worth mentioning that drastic approximations (i.e., harmonic) on the entropic contribution may render questionable the temperature-induced Gibbs energy changes calculated by means of traditional static quantum chemistry calculations. Thus, additional simulations exploiting AIMD coupled with enhanced sampling techniques have been conducted.

Notwithstanding the differences in the two approaches, an attempt to compare the energy barriers and the TSs determined through traditional quantum chemical calculations and recently

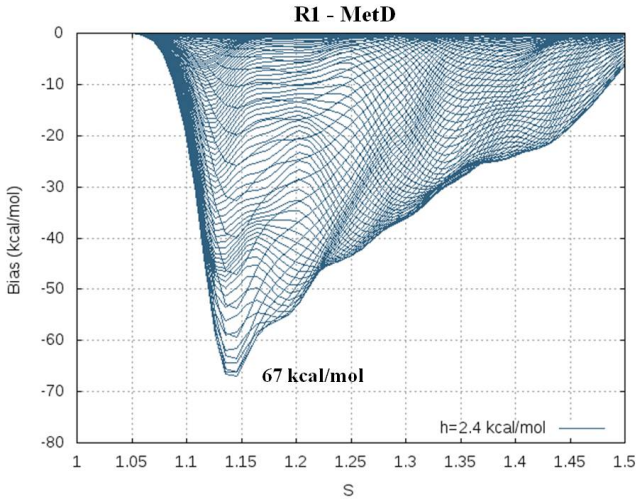

Fig. 5. Metadynamics (MetD) bias, in kcal mol^{-1}, necessary for converting, at 650 K, HCHO and HCN into glycolonitrile (reaction (1)). Abscissa S represents the progress of the reaction; $S \sim 1.14$ refers to a region of the collective variable (CV) space close to the reactants. As reported in the legend, gaussian heights of 2.4 kcal mol^{-1} have been deposed every 50 fs of AIMD exploiting the BLYP-D3(BJ) exchange and correlation functional.

developed MetD schemes (Pietrucci & Saitta 2015) may be useful. In fact, when the latter approach is coupled with AIMD simulations, a fully anharmonic treatment of the entropic contributions is performed by construction. Moreover, such a MetD approach represents a valuable tool in order to characterize the molecular mechanism and, at the same time, gives an estimate of the free-energy barrier characterizing the reaction channel connecting formaldehyde and HCN, on one side, and glycolonitrile ($HOCH_2CN$), on the other. To this aim, several gas-phase AIMD simulations exploiting the BLYP-D3(BJ) exchange and correlation functional have been performed in conjunction with advanced MetD techniques at 650 K. In Fig. 5, the MetD bias deposited on the CV region ascribed to the reactants of reaction (1) until the occurrence of the reaction is shown. In particular, from the depth of such a basin, it is possible to infer an approximate estimate of the free-energy barrier separating reactants from products (at 650 K) as 67 ± 6 kcal mol^{-1}. Incidentally, the latter value is not that far from the previously estimated free-energy barrier of 62.3 kcal mol^{-1} obtained within the harmonic approximation of the entropic contributions to the reaction (albeit using a different exchange-correlation functional). The combination of AIMD and MetD is necessary for tracing the mechanistic evolution of the reactions with atomistic precision and allows for, along with committor analysis (Bolhuis et al. 2002), the precise identification of the TSs fully including the entropic contributions. This way, an educative comparison of the TSs estimated by traditional quantum chemistry calculations, on the one hand, and by AIMD + MetD, on the other, has been performed, as shown in Fig. 6.

3.3.2. Channel 2: $HCHO + NH_3 \rightarrow HCONH_2 + H_2$

The same computational protocol employed for reaction (1) has also been used in order to characterize reaction (2), where the conversion of formaldehyde and ammonia into formamide and di-hydrogen was investigated. The Gibbs energy of the reactants (R), the TS, and the products (P) of reaction (2) was thus evaluated through static quantum chemical calcula-

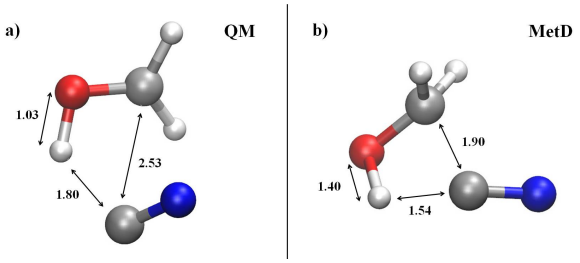

Fig. 6. Comparison between the TSs of reaction (1) obtained by means of static quantum mechanical (*panel a*) and AIMD in conjunction with MetD (*panel b*) techniques at 650 K.

tions, as shown in Fig. 7. In contraposition to the results stemming from reaction (1), at all the investigated temperatures the thermochemical data suggest that formamide and H_2 are more stable than HCHO and NH_3, pointing to a viability of the reaction in the gas phase at all temperatures. Moreover, the higher the temperature is, the more stable are the products with respect to the reactants. In fact, the latter are less stable than the products by 8.7 kcal mol^{-1}, 9.0 kcal mol^{-1}, and 16.5 kcal mol^{-1} at 300 K, 650 K, and 4500 K, respectively, as shown in Fig. 7. On the other hand, in agreement with the data gathered for reaction (1), an increment of the temperature determines a sizable decrease of the barrier height of the process in k_BT units. In particular, whereas the Gibbs energy barrier is 74.4 kcal mol^{-1} and 79.1 kcal mol^{-1} at 300 K and 650 K, respectively, an almost double (absolute) barrier (i.e., 143.2 kcal mol^{-1}) characterizes the energy relative to the reactants of the first-order saddle point (i.e., the TS). After the standard rescaling by the k_BT factor, indeed, it turns out that the reaction at 300 K is hindered by an energy barrier that is about two and ten times larger than those at 650 K and 4500 K, respectively, similar to reaction (1).

In order to handle with higher accuracy the entropic contributions underlying reaction (2), exploratory AIMD + MetD simulations performed at 650 K allowed us to estimate the finite-temperature free-energy barrier of the process, which is shown in Fig. 8. By deposing gaussian hills of the bias with heights equal to 4.8 kcal mol^{-1} every 50 fs of AIMD, we found that a free-energy barrier of 88 ± 4 kcal mol^{-1} has to be overcome in order to convert a gas-phase sample of formaldehyde and ammonia into a sample composed of formamide and di-hydrogen at 650 K. Such an estimate indicates, a posteriori, that albeit not accurate from the entropic treatment standpoint, the energy barrier calculated by means of traditional thermochemistry calculations (i.e., 79.1 kcal mol^{-1}) – at the same (mimicked) temperature – represents a fairly good estimate. Of course, also differences stemming from the use of different exchange-correlation functionals contribute to the difference.

On the other hand, the great advantage in employing AIMD techniques in conjunction with MetD methods is represented by the possibility of tracing the atomistic evolution of the chemical transformation (i.e., the reaction pathway). From our AIMD + MetD simulations, when no constraints are imposed on the possibility to visit the CV space, it turned out that the system tends to pass through an intermediate basin corresponding to aminomethanol. The latter situation has not been predicted by traditional quantum chemistry simulations. However, in order to have a one-to-one comparison with the TS that emerges from such calculations, we also decided to impose a constraint on the accessible portions of the CV space. This way, the direct conversion of the reactants into the products of reaction (2) (i.e., without the inclusion of the aminomethanol intermediate

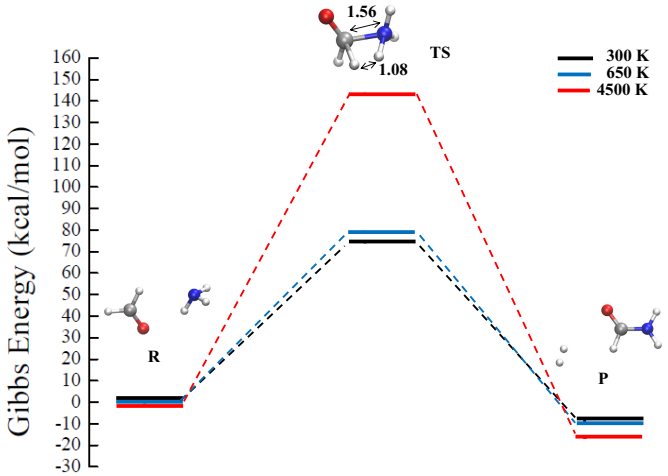

Fig. 7. Gibbs energy of reaction (2) determined through the hybrid meta exchange and correlation functional PW6B95 and Grimme's D3(BJ) dispersion corrections. Some distances (in Å) characterizing the TS are shown. The reaction products become more stable than the reactants at higher temperatures.

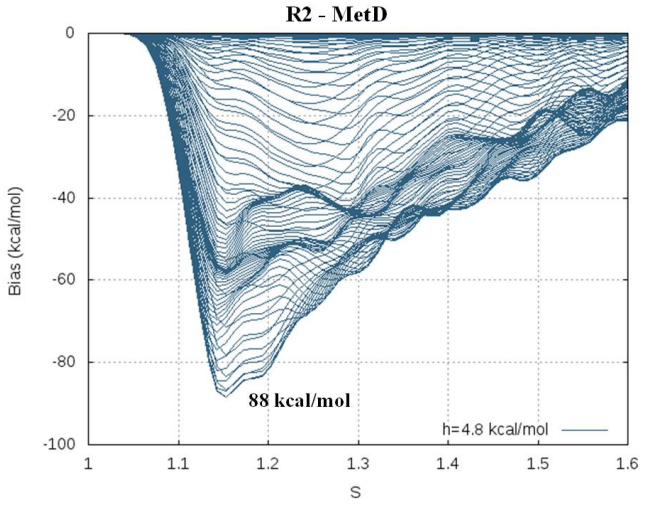

Fig. 8. Metadynamics (MetD) bias, in kcal mol^{-1}, necessary for converting, at 650 K, HCHO and NH_3 into formamide and H_2 (reaction (2)). Abscissa S represents the progress of the reaction; $S \sim 1.15$ refers to a region of the CV space close to the reactants. As reported in the legend, gaussian heights of 4.8 kcal mol^{-1} have been deposed every 50 fs of AIMD exploiting the BLYP-D3(BJ) exchange and correlation functional.

basin) was reproduced by means of AIMD + MetD, mimicking the result of the quantum chemical calculation. Then, a further committor analysis led us to find the most plausible TS structure, which we compare in Fig. 9 with that stemming from quantum mechanical calculations.

4. Formaldehyde in environments of early planets

As mentioned in the Introduction, the analysis of trace elements of ancient zircons indicates a trend of decreasing oxygen fugacity more than 3.6 Gyr ago, suggesting that the early atmosphere was reducing (Yang et al. 2014). Based on astrochemical studies and the analysis of interplanetary matter, we can expect the presence of simple molecules (Hashimoto et al. 2007) such as CO, NH_3, CO_2, H_2O, HCN, HCHO, CH_3OH, and

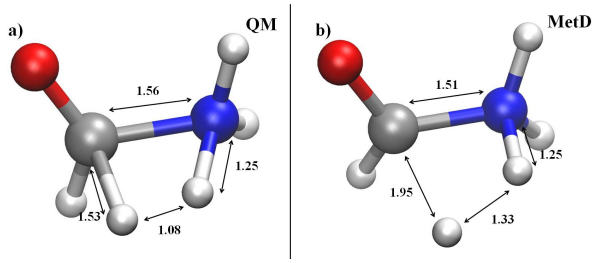

Fig. 9. Comparison between the TSs of reaction (2) obtained by means of static Quantum Mechanical (*panel a*) and AIMD in conjunction with MetD (*panel b*) techniques at 650 K.

maybe $HCONH_2$ (Brucato et al. 2006) together with complex substances such as polymers (tholins) (Khare et al. 1994), various organic compounds, and also biomolecules themselves due to impact delivery or transformation of early planetary chemical environments (Chyba & Sagan 1992; Chyba et al. 1990; Schaefer & Fegley 2007; Hazen & Sverjensky 2010).

In the atmosphere of modern Earth, HCHO is formed largely by the decomposition of isoprene and other large biogenic compounds (Palmer et al. 2003). HCHO is not efficiently formed abiotically in oxygen-rich atmospheres, owing largely to the UV protection afforded by the ozone layer. In $N_2/CO_2/CO/CH_4$ dominated atmospheres, there is no such ozone layer, and CO_2, CH_4, and H_2O can be photodissociated within the troposphere. HCHO is formed from the photochemical products in trace amounts, and HCHO itself is readily photodissociated. These competing processes result in quantities of atmospheric HCHO concentrations on the order of 0.1–10 ppbv. HCHO is readily absorbed into rainwater (Palmer et al. 2003), with a Henry's Law constant of 10^4–10^5 and, assuming that HCHO remains relatively stable within water over million-year timescales, means that rainout of HCHO may lead to concentrated solutions of HCHO and its polymers on the surface. HCHO is formed by the photodissociation of either CO_2 or CH_4, and is not formed efficiently without at least one of these two gases. In a one bar atmosphere composed of 1000 ppm H_2 and H_2O at vapor pressure, HCHO is formed from CO_2 by the following photochemical pathway (Palmer et al. 2003):

$$CO_2 + h\nu \rightarrow CO + O \quad (3)$$

$$H_2 + O \rightarrow \bullet OH + H \quad (4)$$

$$CO + H + M \rightarrow HCO\bullet + M \quad (5)$$

$$HCO\bullet + HCO\bullet \rightarrow HCHO + CO. \quad (6)$$

When we consider the production of formaldehyde using the ARGO 1D model with the STAND2018 network (Ardaseva et al. 2017), we do not find that the photodissociation of water is very efficient in the troposphere in comparison to the oxidation of H_2, but this may depend on the amount of H_2 assumed to be present in the atmosphere of the early Earth. In the absence of CO_2, there is no efficient source of atomic oxygen, and there is therefore a lack of atomic hydrogen needed to protonate CO. It turns out that CH_4 provides an alternative route to the HCHO formation via methanol:

$$CH_4 + h\nu \rightarrow \bullet CH_2(\text{singlet}) + H_2 \quad (7)$$

$$\bullet CH_2(\text{singlet}) + M \rightarrow \bullet CH_2(\text{triplet}) + M \quad (8)$$

Table 2. Detection of prebiotic molecules in experiments with treatment of formaldehyde by electric discharge in the presence of nitrogen and by laser-induced dielectric breakdown plasma induced in a nitrogen atmosphere upon formaldehyde solution in water in the presence of montmorillonite clay, titania (TiO_2), and basaltic rock.

System	Temp	Catalyst	Biomolecules content (ppmv)				
			Adenine	Guanine	Uracil	Cytosine	Glycine
Discharge	650 K	No catalyst	10	3	3	3	200
LIDB	4500 K	Montmorillonite	15	1	0.5	0.5	30
LIDB	4500 K	TiO_2	2	2	0.1	0.4	20
LIDB	4500 K	Basalt	700	3	40	12	50

$$\bullet CH_2(\text{triplet}) + H_2O + M \rightarrow CH_3OH + M \quad (9)$$

$$CH_3OH + h\nu \rightarrow HCHO + H_2O. \quad (10)$$

In both cases, HCHO is destroyed by $HCHO + h\nu \rightarrow CO + H_2$. When atomic oxygen arises from CO_2 photodissociation, an additional pathway to destroying HCHO opens up (i.e., $HCHO + \bullet O \rightarrow HCO \bullet + \bullet OH$); and since the HCO• radical when it reacts with itself can also form $2CO + H_2$, the destruction is not part of a closed loop back to HCHO. Since in the case of a CO/CH_4 dominated atmosphere there is no destruction of HCHO by O, and the formation of HCHO by photodissociating methane is more efficient, the trace abundances of HCHO are predicted to be about an order of magnitude higher in a CH_4/CO dominated atmosphere than in a CO/CO_2 dominated atmosphere, and so the timescale for rainout and concentration of HCHO would be about one order of magnitude shorter, or on the order of 10^5 years.

5. Synthesis based on HCHO impact plasma reprocessing

As shown in the previous section, formaldehyde can be produced by photochemical processes in a planetary atmosphere on trace levels. Extraterrestrial delivery therefore remains the main source of formaldehyde on young planets. In such a case, we can expect plasma reprocessing of this molecule. On surfaces including clays, porous basalt, or metal oxides such as titanium dioxide, we expect a rich chemistry leading to the synthesis of the major building blocks of life. In fact, we observed the formation of biomolecules only in experiments involving porous minerals or on the rocks listed below. This chemistry can therefore take place on the surface of the descending body, when formed compounds are sprayed during disintegration, on dust released from the descending body, or on a planetary surface exposed to impact plasma. Further analyses, executed by means of GC-MS, show that all the canonical nucleobases and glycine (i.e., the simplest amino acid) have also been synthesized in our laser-induced fireball experiments. A description of the experiments is supplied in Table 2.

Our results clearly show that the plasma chemistry of formaldehyde in a nitrogen atmosphere leads to the major building blocks of the RNA world, such as the nucleobases adenine, guanine, uracil, and cytosine, as well as to the formation of ribose and other sugars proven in our previous studies (Civis et al. 2016b). Moreover, we have demonstrated that formamide might not necessarily have played the role of starting prebiotic compound delivered from the extra planetary environments, but it could also serve as an intermediate (maybe also cumulated in the environment) produced, for example, in the plasma chemistry (hypervelocity impacts or electric discharges) in mixtures such as Miller-like $CO + NH_3 + H_2O$ or, as shown here, from far more abundant amounts of formaldehyde. In addition, a recent work published by Sleep (Sleep 2018) suggests that all the formamide-based origin of life scenarios, including that assuming accumulation of formamide in concentrated form as well as that working with diluted aqueous solutions, are highly plausible on early Earth. Our previous study (Ferus et al. 2017a), as well as the spectroscopic survey of the gas phase presented in Fig. 1, additionally shows that in a laser-induced breakdown simulation of an asteroid impact, the formation of large amounts of hydrogen cyanide should also be expected. Besides, the presented quantum-based molecular dynamics simulations clearly show that HCN may participate in the formation of glycolonitrile through reaction (1).

6. Significance for prebiotic chemistry

Our findings, in combination with some evidence gathered during the past two decades, show that the mechanism of prebiotic synthesis heads toward a chemistry of either hydrogen cyanide or formamide, and that these synthetic routes are mutually interconnected. In general, it has been established that the one-pot synthesis of molecules relevant to prebiotic chemistry (sugars, nucleobases, nucleosides, and amino acids) under various conditions such as thermolysis (Saladino et al. 2013), UV irradiations (Senanayake & Idriss 2006), proton irradiation (Ferus et al. 2015b; Saladino et al. 2015, 2017), or plasma chemistry starting with simple compounds and ending with biomolecular building blocks, does not exhibit yields comparable with step by step mechanisms demonstrated by Sutherland et al. (Sutherland 2016). On the other hand, for example the one-pot proton irradiation-initiated formation of ribo- and 2′-deoxyribonucleosides from sugars and purine nucleobases approaches yields of 20% (Saladino et al. 2017) and a recent paper (Becker et al. 2016) shows that the condensation of formamidopyrimidines (FaPys) with sugars provides the natural N-9 nucleosides with extreme regioselectivity and in good yields (60%). Importantly, the FaPys are available from simple precursors: formic acid and aminopyrimidines, which are available from prebiotic molecules that were also detected during the Rosetta comet mission.

However, different conditions are required for each phase, and therefore such synthesis cannot run in a one-pot fashion like the formation of biomolecules initiated, for example, by an asteroid impact. We have shown that all the canonical nucleobases – together with the simplest amino acid glycine – are synthesized from these molecules in high-energy plasma chemistry, notably from starting mixtures composed of NH_3+CO, CH_4+N_2+H_2O, $HCOHN_2$, or HCHO, as inter alia here demonstrated. The early and heavy bombardment represents a significantly long period of the early Earth's history (i.e., about 300 million years; Nesvorny & Morbidelli 2012; Koeberl 2006; Geiss & Rossi 2013; Morbidelli et al. 2012. Impact-induced synthesis therefore does not represent a single event, but a continuing process with a significant impact on the planetary environment over geological timescales. A series of impact events could form deposits of prebiotic feedstock molecules (as shown here, formamide, glycolaldehyde) or serve as a source of prebiotic molecules undergoing further processes (directly sugars, nucleobases, and glycine). One-pot low-yield chemistry needs a final step, which lies in the concentration of the parent molecules as well as products. In the case of formamide produced by impact reprocessing of HCHO, concentration is due to its very high boiling point, for example, in periodically dried lagoons at the sea coasts. Recent prebiotic models also suggest

(Sponer et al. 2016; Cassone et al. 2017c) possible accumulation of formamide via the thermal dissociation of ammonium formate at 180°C near some volcanoes. Under these conditions, formamide forms as a liquid, while water is immediately evaporated.

7. Conclusions

In this study, laboratory simulations of the high-velocity impact of extraterrestrial bodies into planetary atmospheres have been performed with a focused beam of the high power kJ-class laser system. In particular, the reaction network of formaldehyde – in a nitrogen atmosphere – arising upon exposure to such high-density-energy events has been identified, with a special focus on the formation of prebiotically relevant precursors. In fact, the formation of the key intermediate molecule formamide has been observed during those experiments. As quantitatively evaluated by traditional quantum chemical calculations and ab initio molecular dynamics coupled with advanced metadynamics simulations, here synergistically exploited in a complementary fashion, the conversion of formaldehyde into formamide is thermodynamically plausible under such extreme conditions.

From the formamide synthesis, the further chemical evolution of the sample subjected to the impact develops toward the formation of more complex molecules, which are intimately related to the onset of life on early Earth or on Earth-like planets. Indeed, besides the formation of a variety of unstable radicals and simple molecular species such as formic acid, the plasma-induced chemistry leads to the synthesis of other prebiotic molecules such as AHAN and AHMN. Even more interestingly, here we demonstrate that the reaction network of a sample composed of formaldehyde and nitrogen-bearing species subjected to conditions typical of impact events leads to the onset of biologically relevant entities. Indeed, the one-pot synthesis of all the canonical nucleobases of the simplest amino acid (i.e., glycine), and of the sugar ribose has been observed. To summarize, not only the chemical pathways and the thermodynamics of the first steps from formaldehyde toward chemical complexity have been here disclosed by combining standard, static, quantum chemistry calculations and more recent ab initio molecular dynamics simulations coupled with enhanced sampling techniques, but we have also experimentally demonstrated the one-pot formation of all the nucleobases, of glycine, and of ribose from formaldehyde- and nitrogen-containing samples under impact shock conditions. This way, we have shown not only that the chemistries of formaldehyde and formamide may be interconnected but also that both parent molecules may serve as precursors of the main building blocks for the subsequent formation of informational polymers and – ultimately – of life.

Acknowledgements. This work is part of a research series funded by the Czech Science Foundation (grants no. 17-05076S and 18-20609S), and ERDF/ESF "Centre of Advanced Applied Sciences" (No. CZ.02.1.01/0.0/0.0/16019/0000778).

References

Abelson, P. H. 1956, Science, 124, 935
Adam, Z. R., Hongo, Y., Cleaves, II., H. J., et al. 2018, Sci Rep., 8, 165
Adande, G. R., Woolf, N. J., & Ziurys, L. M. 2013, Astrobiology, 13, 439
Al-Edhari, A. J., Ceccarelli, C., Kahane, C., et al. 2017, A&A, 597, A40
Ardaseva, A., Rimmer, P. B., Waldmann, I., et al. 2017, MNRAS, 470, 187
Barks, H. L., Buckley, R., Grieves, G. A., et al. 2010, ChemBioChem, 11, 1240
Becke, A. D. 1988, Phys. Rev. A, 38, 3098
Becker, S., Thoma, I., Deutsch, A., et al. 2016, Science, 352, 833
Bell, E. A., Boehnke, P., Harrison, T. M., & Mao, W. L. 2015, Proc. Natl. Acad. Sci. USA, 112, 14518
Berezhnoy, A. A., & Borovicka, J. 2010, Icarus, 210, 150
Bernstein, M. P., Sandford, S. A., Allamandola, L. J., et al. 1995, ApJ, 454, 327
Bockelee-Morvan, D., Lis, D. C., Wink, J. E., et al. 2000, A&A, 353, 1101
Bolhuis, P. G., Chandler, D., Dellago, C., & Geissler, P. L. 2002, Annu. Rev. Phys. Chem., 53, 291
Borovicka, J., & Berezhnoy, A. A. 2016, Icarus, 278, 248
Botta, L., Bizzarri, B. M., Piccinino, D., et al. 2017, Eur. Phys. J. Plus, 132, 317
Branduardi, D., Gervasio, F. L., & Parrinello, M. 2007, J. Chem. Phys., 126, 54103
Brucato, J. R., Baratta, G. A., & Strazzulla, G. 2006, A&A, 455, 395
Bussi, G., Donadio, D., & Parrinello, M. 2007, J. Chem. Phys., 126, 14101
Camacho, J. J., Diaz, L., Santos, M., et al. 2008, J. Phys. D, 41, 40037178
Cassone, G., Pietrucci, F., Saija, F., et al. 2017a, Chem. Sci., 8, 2329
Cassone, G., Pietrucci, F., Saija, F., et al. 2017b, Sci. Rep., 7, 6901
Cassone, G., Sponer, J., Saija, F., et al. 2017c, Phys. Chem. Chem. Phys., 19, 1817
Cassone, G., Saija, F., Sponer, J., et al. 2018a, ApJL, 866, L23
Cassone, G., Sponer, J., Sponer, J. E., et al. 2018b, Chem. Commun., 54, 3211
Chyba, C., & Sagan, C. 1992, Nature, 355, 125
Chyba, C. F., Thomas, P. J., Brookshaw, L., & Sagan, C. 1990, Science, 249, 366
Civis, S., Babankova, D., Cihelkat, J., et al. 2008, J. Phys. Chem. A, 112, 7162
Civis, S., Ferus, M., Kubelik, P., et al. 2012a, A&A, 532, A35
Civis, S., Ferus, M., Kubelik, P., et al. 2012b, A&A, 535, A61
Civis, S., Ferus, M., Kubelik, P., et al. 2012c, J. Opt. Soc. Am., 29, 1112
Civis, S., Kubelik, P., & Ferus, M. 2012d, J. Phys. Chem. A, 116, 3137
Civis, S., Ferus, M., Zukalova, M., et al. 2013, Opt. Mater., 36, 159
Civis, S., Szabla, R., Szyja, B. M., et al. 2016a, Sci. Rep., 6, 23199
Civis, S., Ferus, M., Knízek, A., et al. 2016b, Phys. Chem. Chem. Phys., 18, 27317
Civis, S., Knízek, A., Ivanek, O., et al. 2017, Nat. Astron., 1, 721
Cleaves, II., H. J. 2008, Precambrian Res., 164, 111
Cohen, R. J. 1984, MNRAS, 208, 101
Cooper, G., Kimmich, N., Belisle, W., et al. 2001, Nature, 414, 879
Dodd, M. S., Papineau, D., Greene, T., et al. 2017, Nature, 543, 60
Downes, D., & Wilson, T. L. 1974, ApJ, 191, L77
Ferus, M., Cihelka, J., & Civis, S. 2008, Chem. List., 102, 417
Ferus, M., Kubelik, P., & Civis, S. 2011a, J. Phys. Chem. A, 115, 12132
Ferus, M., Kubelik, P., Kawaguchi, K., et al. 2011b, J. Phys. Chem. A, 115, 1885
Ferus, M., Civis, S., Mladek, A., et al. 2012, J. Am. Chem. Soc., 134, 20788
Ferus, M., Knizek, A., Civis, S., et al. 2015a, Proc. Natl. Acad. Sci. USA, 112, 7109
Ferus, M., Nesvorný, D., Sponer, J., et al. 2015b, Proc. Natl. Acad. Sci. USA, 112, 657
Ferus, M., Kubelík, P., Knízek, A., et al. 2017a, Sci. Rep., 7, 6275
Ferus, M., Pietrucci, F., Saitta, A. M., et al. 2017b, Proc. Natl. Acad. Sci. USA, 114, 4306
Ferus, M., Laitl, V., Knizek, A., et al. 2018, A&A, 616, A150
Forster, J. R., Goss, W. M., Dickel, H. R., & Habing, H. J. 1981, MNRAS, 197, 513
Fox, S. W., & Windsor, C. R. 1971, Science, 174, 1040
Frank, N. 2012, Wiley Interdiscip. Rev. Comput. Mol. Sci., 2, 73
Geiss, J., & Rossi, A. P. 2013, Astron. Astrophys. Rev., 21, 1
Gilbert, W. 1986, Nature, 319, 618
Goedecker, S., Teter, M., & Hutter, J. 1996, Phys. Rev. B, 54, 1703
Goesmann, F., Rosenbauer, H., Bredehoeft, J. H., et al. 2015, Science, 349, 6247
Grimme, S., Antony, J., Ehrlich, S., & Krieg, H. 2010, J. Chem. Phys., 132, 154104
Grimme, S., Ehrlich, S., & Goerigk, L. 2011, J. Comput. Chem., 32, 1456
Halfen, D. T., Apponi, A. J., Woolf, N., et al. 2006, ApJ, 639, 237
Hashimoto, G. L., Abe, Y., & Sugita, S. 2007, J. Geophys. Res., 112, E05010
Hazen, R. M., & Sverjensky, D. A. 2010, Cold Spring Harb Perspect Biol., 2, a002162
Hoerst, S. M., Yelle, R. V., Buch, A., et al. 2012, Astrobiology, 12, 809
Hutter, J., Iannuzzi, M., Schiffmann, F., & VandeVondele, J. 2014, Wiley Interdiscip. Rev. Comput. Mol. Sci., 4, 15
Jenniskens, P., Laux, C. O., Wilson, M. A., & Shaller, E. L. 2004, Astrobiology, 4, 81
Jungwirth, K., Cejnarova, A., Juha, L., et al. 2001, Phys. Plasmas, 8, 2495
Kahane, C., Ceccarelli, C., Faure, A., & Caux, E. 2013, ApJ, 763, L38
Khare, B. N., Sagan, C., Thomson, W. R., et al. 1994, Rev. Can. Chim., 72, 678
Koeberl, C. 2006, Elements, 2, 211
Kuwahara, H., & Sugita, S. 2015, Icarus, 257, 290
Laio, A., & Parrinello, M. 2002, Proc. Natl. Acad. Sci. USA, 99, 12562
Lazcano, A., & Bada, J. L. 2003, Orig. Life Evol. Biosph., 33, 235
Lee, C., Yang, W., & Parr, R. G. 1988, Phys. Rev. B, 37, 785
Mangum, J. G., Wootten, A., Loren, R. B., & Wadiak, E. J. 1990, ApJ, 348, 542

Manion, J. A., Huie, R. E., & Levin, R. D. 2015, Kinetic Database. In: NIST Chem. Kinet. Database, NIST Stand. Ref. Database 17, Version 7.0 (Web Version), Release 1.6.8, Data, Natl. Inst. Stand. Technol. Gaithersburg, Maryland, 20899
Martins, Z. 2011, Elements, 7, 35
Martins, Z., Botta, O., Fogel, M. L., et al. 2008, Earth Planet Sci. Lett., 270, 130
Martins, Z., Modica, P., Zanda, B., & D'Hendecourt, L. L. S. 2015, Meteorit. Planet. Sci., 50, 926
Menor-Salvan, C., & Marin-Yaseli, M. R. 2012, Chem. Soc. Rev., 41, 5404
Miller, S. L. 1953, Science, 117, 528
Miyakawa, S., Yamanashi, H., Kobayashi, K., et al. 2002, Proc. Natl. Acad. Sci. USA, 99, 14628
Mojzsis, S. J., Arrhenius, G., McKeegan, K. D., et al. 1996, Nature, 384, 55
Morbidelli, A., Marchi, S., Bottke, W. F., & Kring, D. A. 2012, Earth Planet. Sci. Lett., 355, 144
Nemes, L., Mohai, M., Donko, Z., & Bertoti, I. 2000, Spectrochim. Acta, 56, 761
Nesvorny, D., & Morbidelli, A. 2012, AJ, 144, 20
Oberg, K. I. 2016, Chem. Rev., 116, 9631
Oberg, K. I., Guzman, V. V., Furuya, K., et al. 2015, Nature, 520, 198
Okabe, H. 1970, J. Chem. Phys., 53, 3507
Palmer, P. I., Jacob, D. J., Fiore, A. M., et al. 2003, J. Geophys. Res., 108, D6
Parker, E. T., Zhou, M., Burton, A. S., et al. 2014, Chem. Int. Ed., 53, 8132
Pietrucci, F. 2017, Rev. Phys., 2, 32
Pietrucci, F., & Saitta, A. M. 2015, Proc. Natl. Acad. Sci. USA, 112, 15030
Powner, M. W., & Sutherland, J. D. 2011, Phil. Trans. R. Soc., 366, 2870
Powner, M. W., Sutherland, J. D., & Szostak, J. W. 2011, Synlett, 14, 1956
Raunier, S., Chiavassa, T., Duvernay, F., et al. 2004, A&A, 416, 165
Rode, B. M. 1999, Peptides, 20, 773
Rotelli, L., Trigo-Rodriguez, J. M., Moyano-Cambero, C. E., et al. 2016, Sci. Rep., 6, 38888
Rothman, L. S., Gordon, I. E., Babikov, Y., et al. 2013, J. Quant. Spectrosc. Radiat. Transf., 130, 4
Saitta, A. M., & Saija, F. 2014, Proc. Natl. Acad. Sci. USA, 111, 13768
Saladino, R., Crestini, C., Costanzo, G., et al. 2001, Med. Chem., 9, 1249
Saladino, R., Crestini, C., Ciciriello, F., et al. 2007, Chem. Biodivers., 4, 694
Saladino, R., Botta, G., Pino, S., et al. 2012a, Biochimie, 94, 1451
Saladino, R., Botta, G., Pino, S., et al. 2012b, Chem. Soc. Rev., 41, 5526
Saladino, R., Botta, G., Delfino, M., & Di Mauro, E. 2013, Chem. Eur. J., 19, 16916
Saladino, R., Carota, E., Botta, G., et al. 2015, Proc. Natl. Acad. Sci. USA, 112, E2746
Saladino, R., Botta, G., Bizzarri, B. M., et al. 2016, Biochem., 55, 2806
Saladino, R., Bizzarri, B. M., Botta, L., et al. 2017, Sci Rep., 7, 14709
Senanayake, S. D., & Idriss, H. 2006, Proc. Natl. Acad. Sci. USA, 103, 1194
Schaefer, L., & Fegley, B. 2007, Icarus, 186, 462
Schlesinger, G., & Miller, S. L. 1983, J. Mol. Evol., 19, 383
Sleep, N. H. 2018, Astrobiology, 18, 1199
Sponer, J. E., Sponer, J., Novakova, O., et al. 2016, Chem. Eur. J., 22, 3572
Strecker, A. 1850, Ann. Chem. Pharm., 1, 27
Strecker, A. 1854, Ann. Chem. Pharm., 3, 349
Sutherland, J. D. 2017, Nat. Rev. Chem., 1, 0012
Sutherland, J. D. 2016, Angew. Chem. Int. Ed., 55, 104
Sponer, J. E., Szabla, R., Góra, R. W., et al. 2016, Phys. Chem. Chem. Phys., 18, 20047
Thompson, M. A., Macdonald, G. H., & Millar, T. J. 1999, A&A, 342, 809
Tribello, G. A., Bonomi, M., Branduardi, D., et al. 2014, Comput. Phys. Commun., 185, 604
Weigend, F. 2006, Phys. Chem. Chem. Phys., 8, 1057
Weigend, F., & Ahlrichs, R. 2005, Phys. Chem. Chem. Phys., 7, 3297
Xu, J., Tsanakopoulou, M., Magnani, C. J., et al. 2017, Nat. Chem., 9, 303
Yang, X., Gaillard, F., & Scaillet, B. 2014, Earth Planet Sci. Lett., 393, 210
Zahnle, K., Schaefer, L., & Fegley, B. 2010, Cold Spring Harb. Perspect. Biol., 2, a004895
Zhao, Y., & Truhlar, D. G. 2005, J. Phys. Chem. A, 109, 5656

Appendix A: Additional material

A.1. Plasma chemistry network studied by ab initio molecular dynamics, metadynamics, and quantum chemical calculations

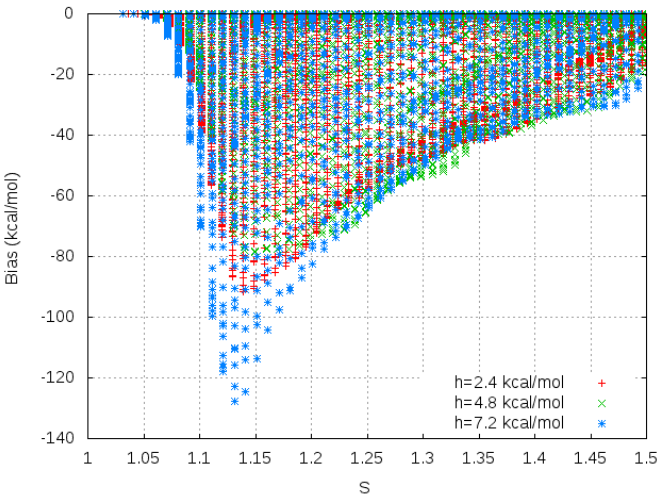

Fig. A.1. Metadynamics (MetD) bias, in kcal mol^{-1}, necessary for converting, at 650 K, HCHO and HCN into glycolonitrile (reaction (1)). As reported in the legend, red crosses, green crosses, and blues asterisks correspond to simulations conducted by deposing gaussian heights of the bias equal to 2.4, 4.8, and 7.2 kcal mol^{-1}, respectively. Since the simulation employing heights equal to 2.4 kcal mol^{-1} was "slow" enough (yielding a bias profile similar to the choice 4.8 kcal mol^{-1}), such a value has been chosen in order to repeat, three additional times, reaction (1) by means of AIMD + MetD techniques.

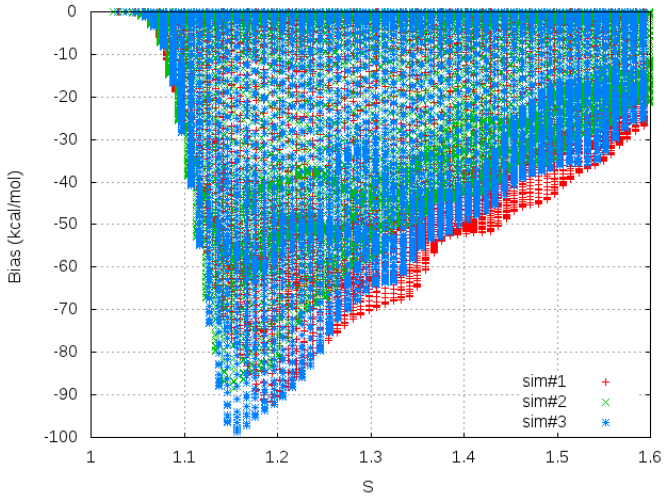

Fig. A.2. Metadynamics (MetD) bias, in kcal mol^{-1}, necessary for converting, at 650 K, HCHO and NH_3 into formamide and H_2 (reaction (2)). Data points represent the bias deposed in the reactants portion of the collective variables space referred to three parallel simulations performed by employing gaussian heights equal to 4.8 kcal mol^{-1}.

A.2. Detection of nucleobases

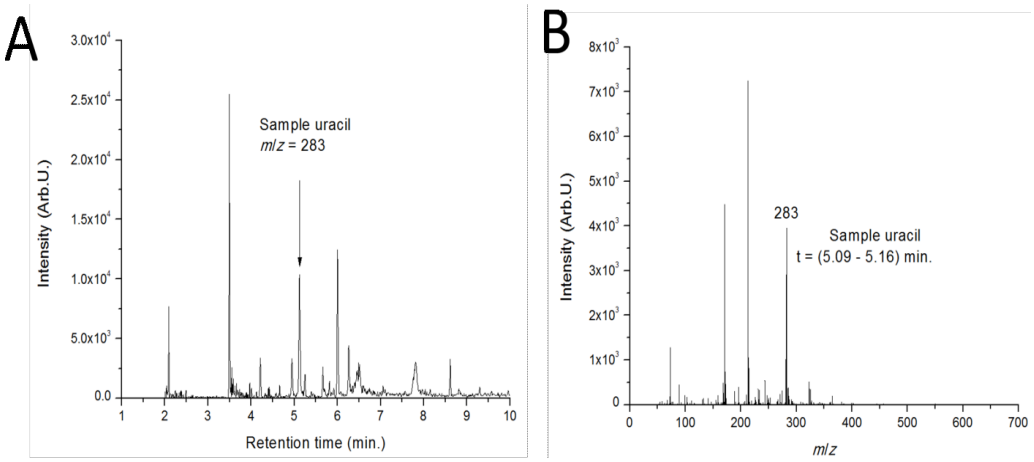

Fig. A.3. Uracil detected in the sample from electric discharge cell (methanol extract from the discharge tube) in HCHO mixed with nitrogen. *Panel A*: chromatogram with the assignment of a corresponding peak of uracil. *Panel B*: mass spectrum of uracil with retention time t and typical peak at $m/z = 283$.

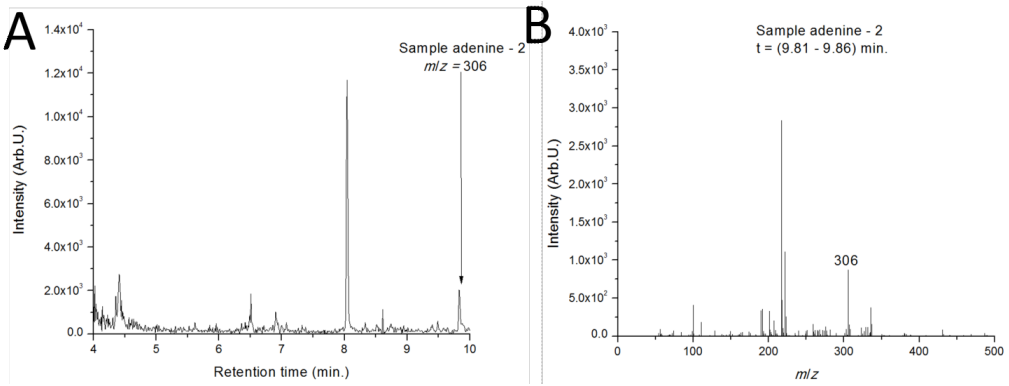

Fig. A.4. Adenine detected in the sample from electric discharge cell (methanol extract from the discharge tube) in HCHO mixed with nitrogen. *Panel A*: chromatogram with the assignment of a corresponding peak of adenine. *Panel B*: mass spectrum of adenine with retention time t and typical peak at $m/z = 306$.

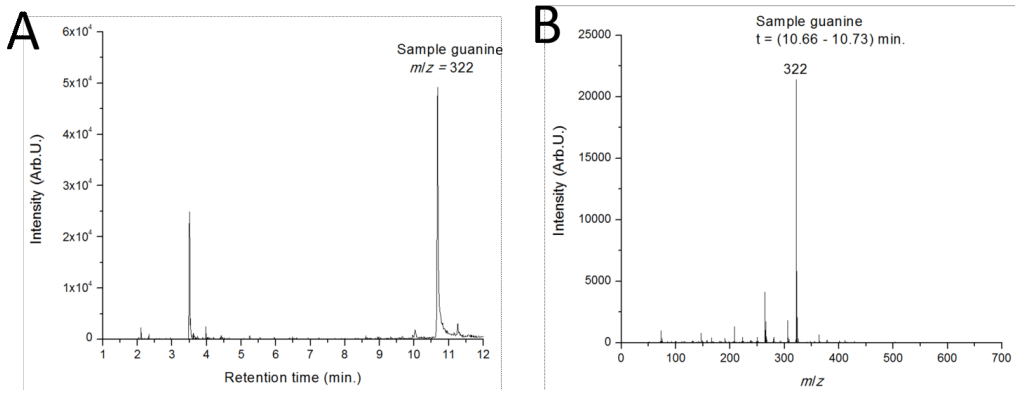

Fig. A.5. Guanine detected in the sample from electric discharge cell (methanol extract from the discharge tube) in HCHO mixed with nitrogen. *Panel A*: chromatogram with the assignment of a corresponding peak of guanine. *Panel B*: mass spectrum of guanine with retention time t and typical peak at $m/z = 322$.

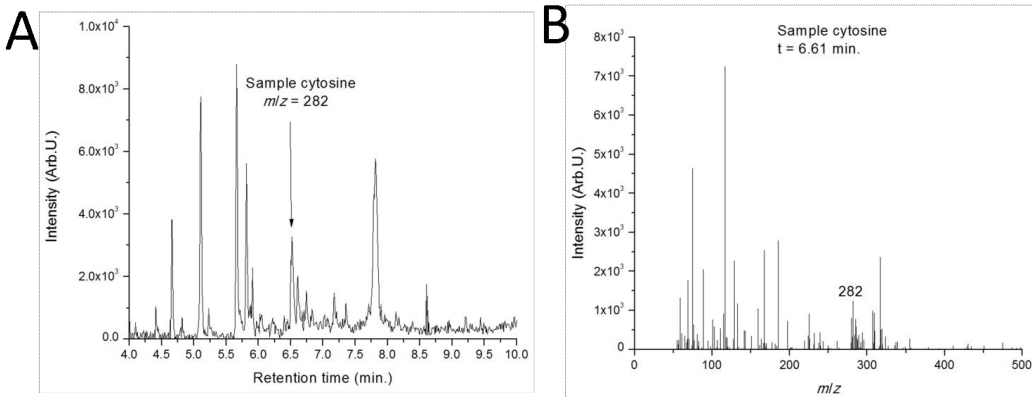

Fig. A.6. Cytosine detected in the sample from electric discharge cell (methanol extract from the discharge tube) in HCHO mixed with nitrogen. *Panel A*: chromatogram with the assignment of a corresponding peak of cytosine. *Panel B*: mass spectrum of cytosine with retention time t and typical peak at $m/z = 282$.

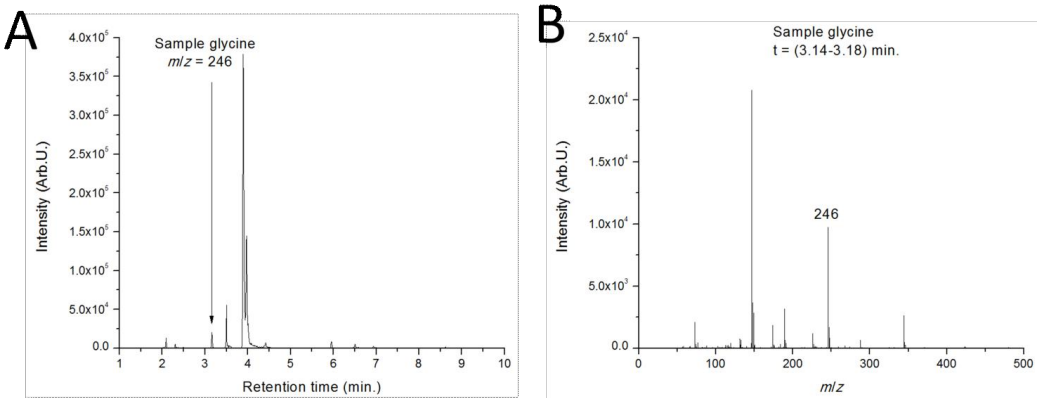

Fig. A.7. Glycine detected in the sample from electric discharge cell (methanol extract from the discharge tube) in HCHO mixed with nitrogen. *Panel A*: chromatogram with the assignment of a corresponding peak of glycine. *Panel B*: mass spectrum of glycine with retention time t and typical peak at $m/z = 246$.

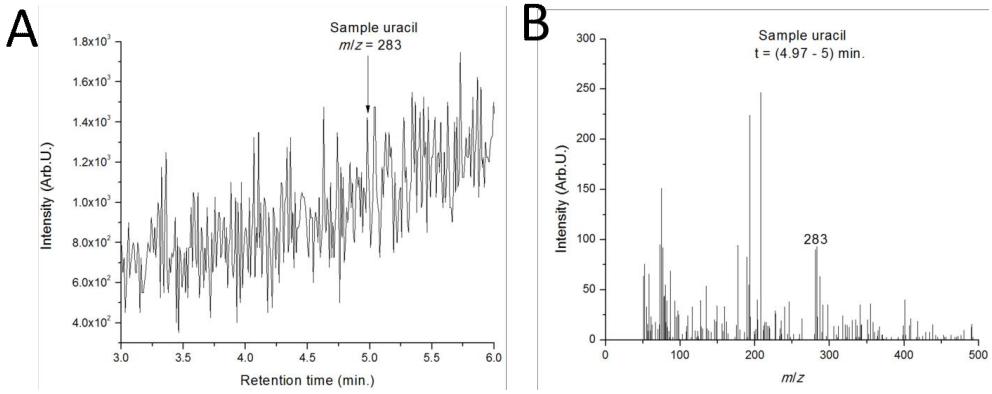

Fig. A.8. Uracil detected in the sample of HCHO solution treated with LIDB in the presence of montmorillonite upon nitrogen atmosphere. *Panel A*: chromatogram with the assignment of a corresponding peak of uracil. *Panel B*: mass spectrum of uracil with retention time t and typical peak at $m/z = 283$.

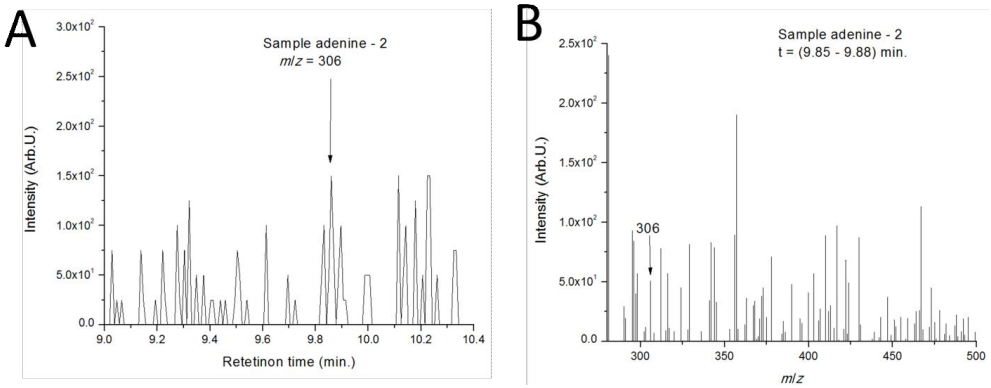

Fig. A.9. Adenine detected in the sample of HCHO solution treated with LIDB in the presence of montmorillonite upon nitrogen atmosphere. *Panel A*: depicts a chromatogram with the assignment of a corresponding peak of adenine. Panel B shows the mass spectrum of adenine with retention time t and typical peak at $m/z = 306$.

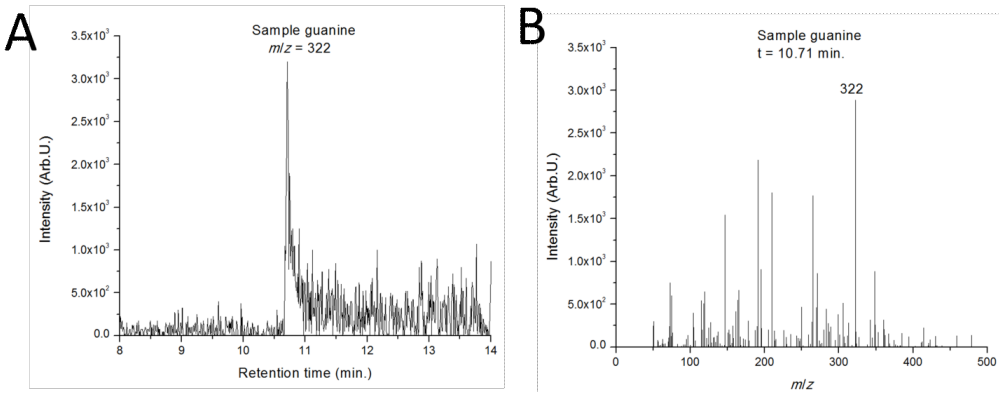

Fig. A.10. Guanine detected in the sample of HCHO solution treated with LIDB in the presence of montmorillonite upon nitrogen atmosphere. *Panel A*: depicts a chromatogram with the assignment of a corresponding peak of guanine. *Panel B*: mass spectrum of guanine with retention time t and typical peak at $m/z = 322$.

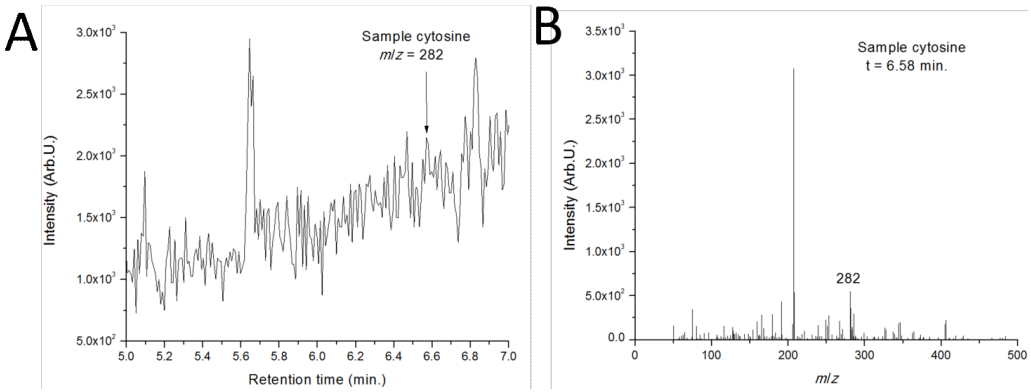

Fig. A.11. Cytosine detected in the sample of HCHO solution treated with LIDB in the presence of montmorillonite upon nitrogen atmosphere. *Panel A*: depicts a chromatogram with the assignment of a corresponding peak of cytosine. *Panel B*: mass spectrum of cytosine with retention time t and typical peak at $m/z = 282$.

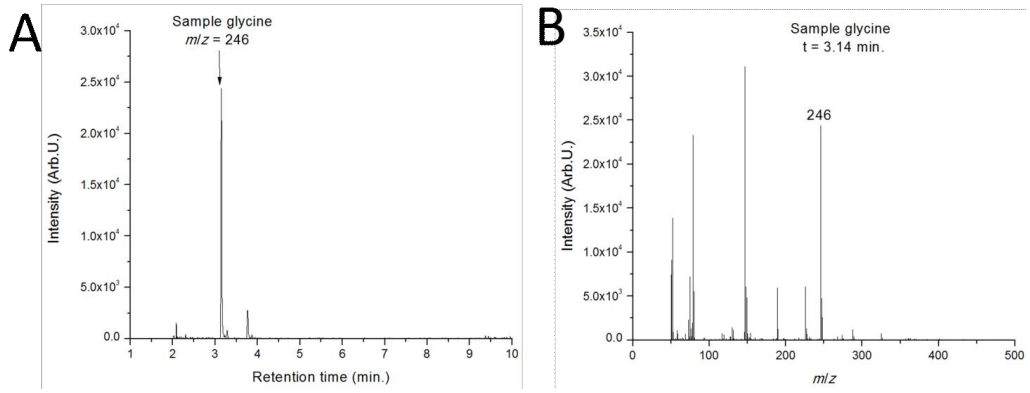

Fig. A.12. Glycine detected in the sample of HCHO solution treated with LIDB in the presence of montmorillonite upon nitrogen atmosphere. *Panel A*: depicts a chromatogram with the assignment of a corresponding peak of glycine. *Panel B*: mass spectrum of glycine with retention time t and typical peak at $m/z = 246$.

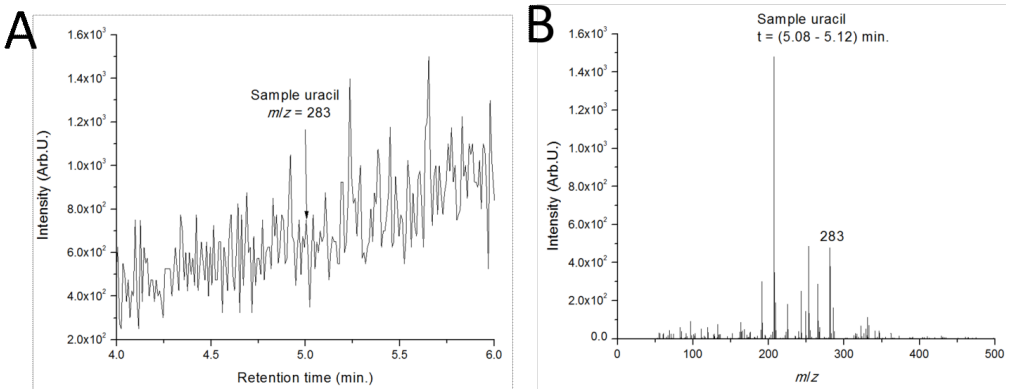

Fig. A.13. Uracil detected in the sample of HCHO solution treated with LIDB in the presence of anatase upon nitrogen atmosphere. *Panel A*: chromatogram with the assignment of a corresponding peak of uracil. *Panel B*: mass spectrum of uracil with retention time t and typical peak at $m/z = 283$.

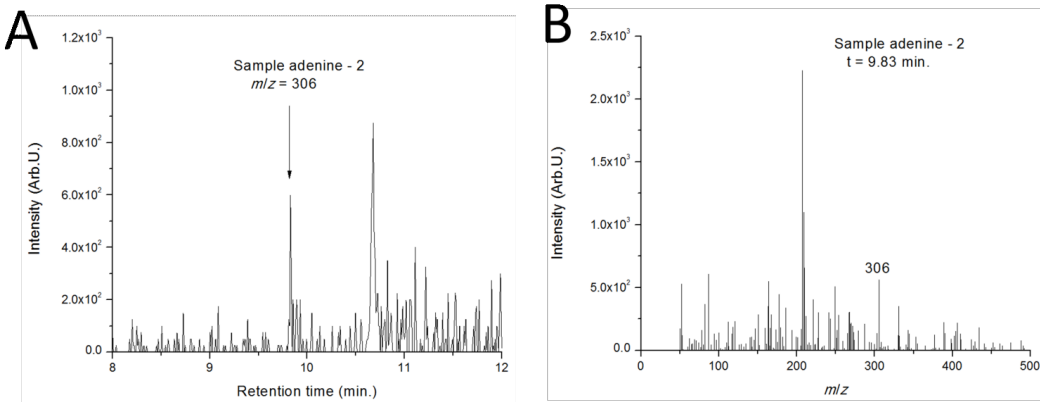

Fig. A.14. Adenine detected in the sample of HCHO solution treated with LIDB in the presence of anatase upon nitrogen atmosphere. *Panel A*: chromatogram with the assignment of a corresponding peak of adenine. *Panel B*: mass spectrum of adenine with retention time t and typical peak at $m/z = 306$.

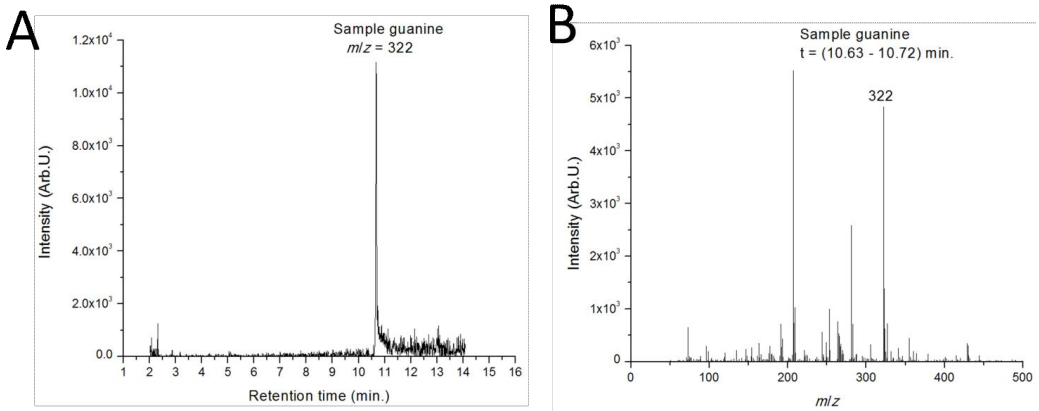

Fig. A.15. Guanine detected in the sample of HCHO solution treated with LIDB in the presence of anatase upon nitrogen atmosphere. *Panel A*: chromatogram with the assignment of a corresponding peak of guanine. *Panel B*: mass spectrum of guanine with retention time t and typical peak at $m/z = 322$.

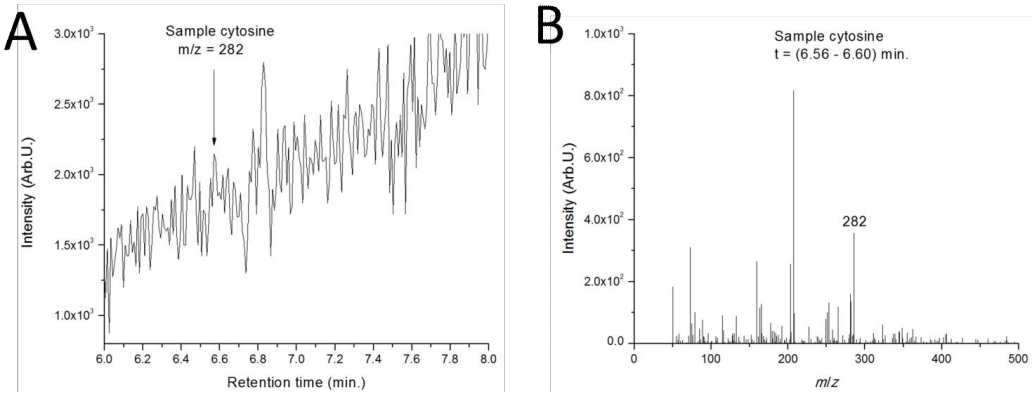

Fig. A.16. Cytosine detected in the sample of HCHO solution treated with LIDB in the presence of anatase upon nitrogen atmosphere. *Panel A*: chromatogram with the assignment of a corresponding peak of cytosine. *Panel B*: mass spectrum of cytosine with retention time t and typical peak at $m/z = 282$.

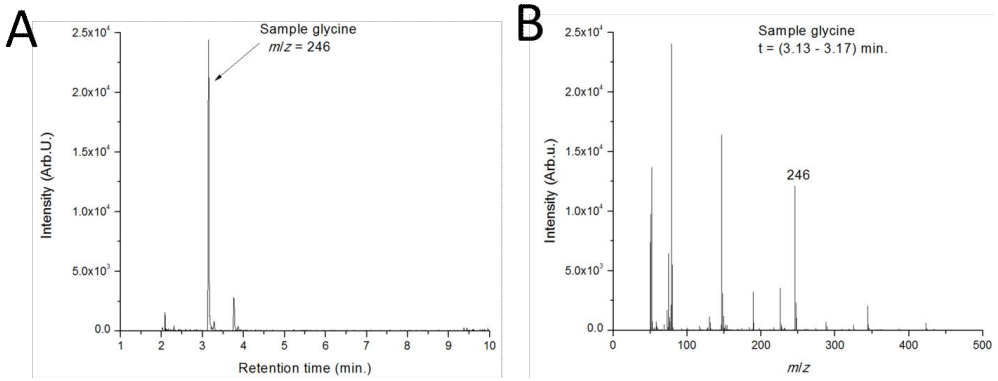

Fig. A.17. Glycine detected in the sample of HCHO solution treated with LIDB in the presence of anatase upon nitrogen atmosphere. *Panel A*: chromatogram with the assignment of a corresponding peak of glycine. *Panel B*: mass spectrum of glycine with retention time t and typical peak at $m/z = 246$.

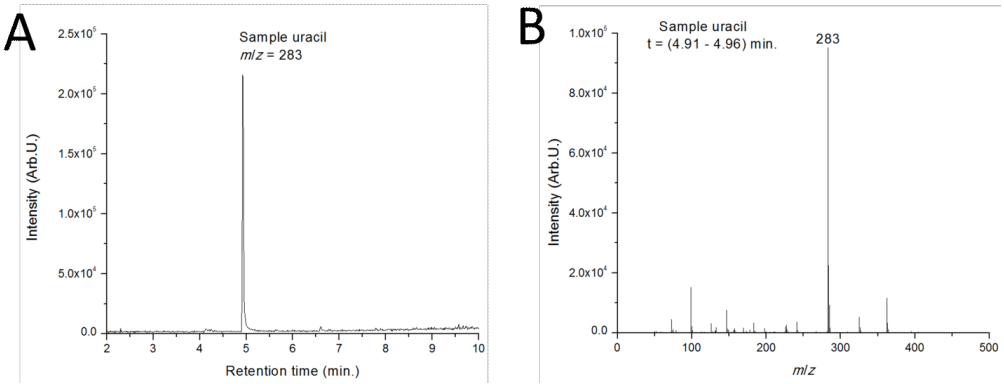

Fig. A.18. Uracil detected in the sample of HCHO solution treated with LIDB in the presence of basalt upon nitrogen atmosphere. *Panel A*: chromatogram with the assignment of a corresponding peak of uracil. *Panel B*: mass spectrum of uracil with retention time t and typical peak at $m/z = 283$.

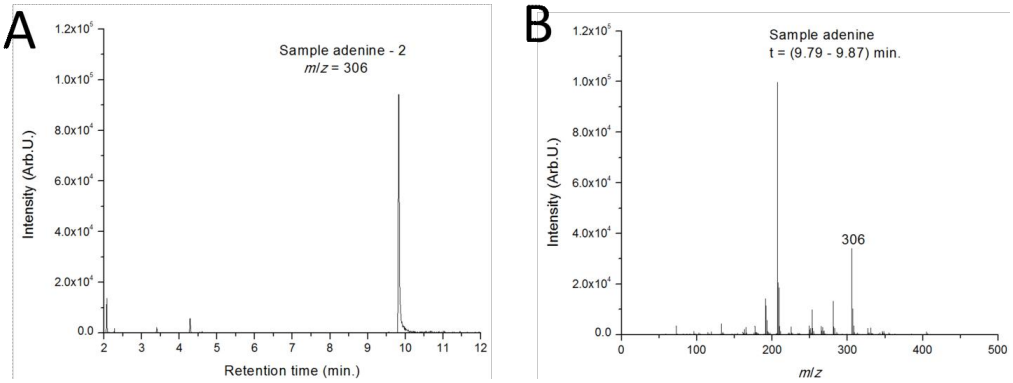

Fig. A.19. Adenine detected in the sample of HCHO solution treated with LIDB in the presence of basalt upon nitrogen atmosphere. *Panel A*: chromatogram with the assignment of a corresponding peak of adenine. *Panel B*: mass spectrum of adenine with retention time t and typical peak at $m/z = 306$.

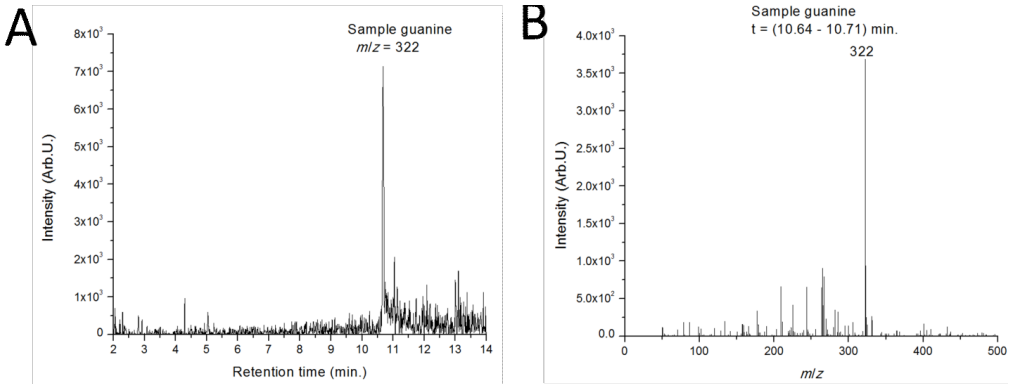

Fig. A.20. Guanine detected in the sample of HCHO solution treated with LIDB in the presence of basalt upon nitrogen atmosphere. *Panel A*: chromatogram with the assignment of a corresponding peak of guanine. *Panel B*: mass spectrum of guanine with retention time t and typical peak at $m/z = 322$.

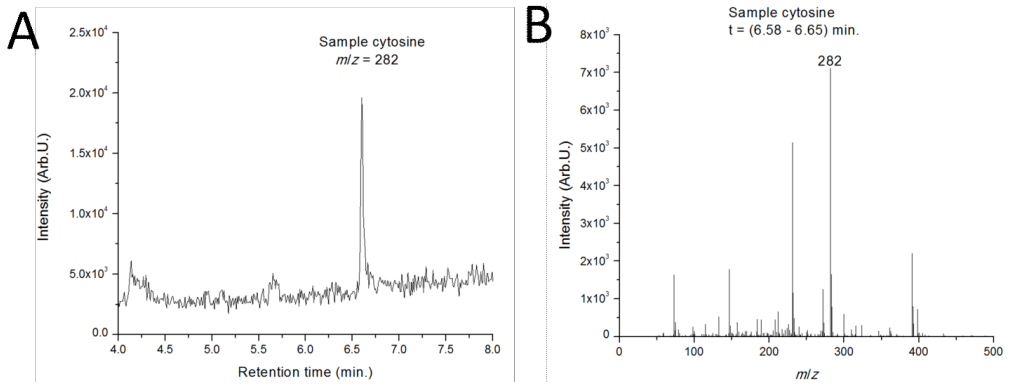

Fig. A.21. Cytosine detected in the sample of HCHO solution treated with LIDB in the presence of basalt upon nitrogen atmosphere. *Panel A*: chromatogram with the assignment of a corresponding peak of cytosine. *Panel B*: mass spectrum of cytosine with retention time t and typical peak at $m/z = 282$.

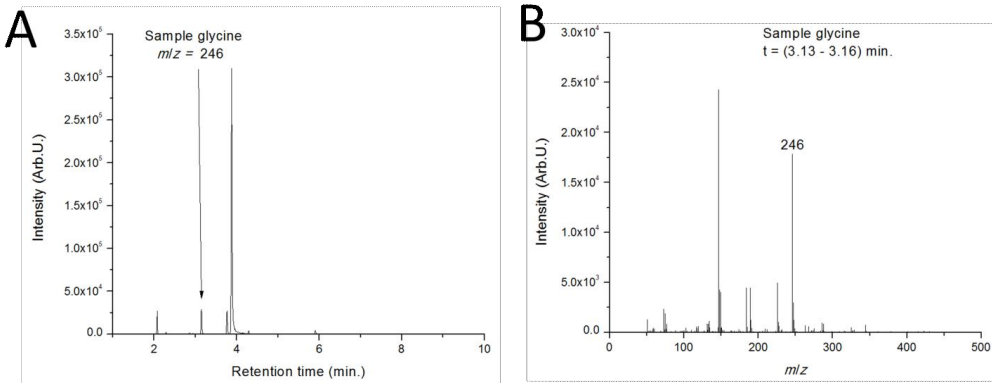

Fig. A.22. Glycine detected in the sample of HCHO solution treated with LIDB in the presence of basalt upon nitrogen atmosphere. *Panel A*: chromatogram with the assignment of a corresponding peak of glycine. *Panel B*: mass spectrum of glycine with retention time t and typical peak at $m/z = 246$.

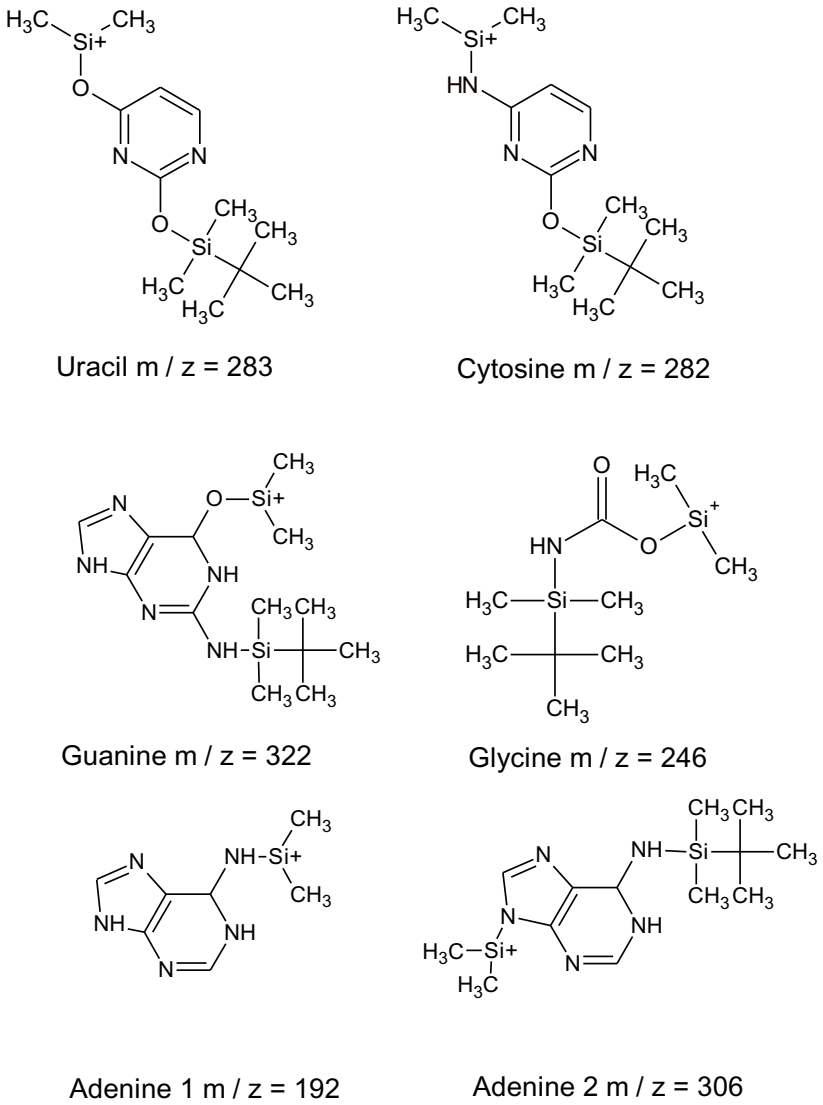

Fig. A.23. Structure and typical masses of main fragments of the canonical nucleic bases and glycine after derivatization.

A.3. Contamination

Regarding possible contamination, we have performed a comparative analysis of blanks. The blanks are compared with a standard chromatogram of 20 ppm of nucleobases diluted in formaldehyde (Fig. A.24, panel A) and with irradion upon a nitrogen atmosphere (panel B). We conducted a reference experiment without irradiation with montmorillonite used as a catalyst (panel C), and we did not detect any one nucleobase. All the results were negative. We also tested nucleobases in water after washing of the vessel touched with fingers without gloves (panel D) and water washed using a montmorillonite catalyst (panel E). We obtained negative results. We show four blank chromatograms. Apart from analyses of blank samples, we would like to note that if any contamination had been caused by biological DNA/RNA, then other compounds, such as ribose, should have been detected. Another argument for the noncontamination is that adenine and uracil, and guanine and cytosine, would have to exhibit comparable concentrations (due to standard A=U and G=C pairing in RNA), which, again, was not observed. Last, but not least, amounts of nucleobases found in the sample imply ng μl^{-1} concentrations of nucleic acids. Such concentrations are usually observed during standard plasmid DNA extraction and purification from E. coli. It is very difficult to imagine that such a high concentration of nucleic acids was caused by simple contamination.

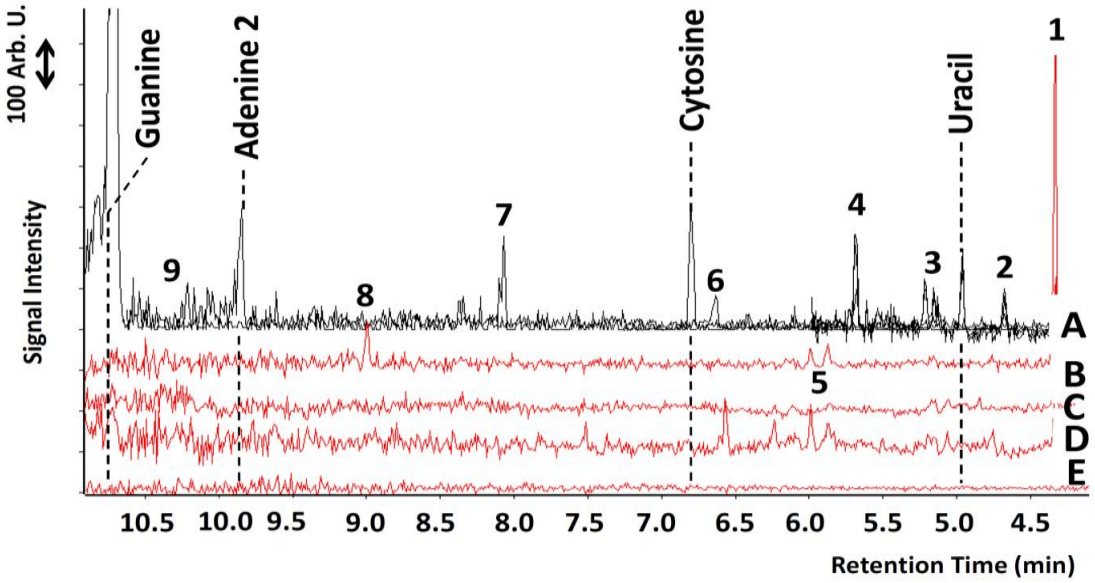

Fig. A.24. Chromatograms of blank measurements, all of them with a derivatization agent, together with a chromatogram of standard of 20 ppm of nucleobases for comparison depicted in *panel A*. *Panels B and C*: chromatographic record of a cell filled with nitrogen exposed to a plasma and a record of a cell from a laser shock wave experiment not exposed to plasma, both washed with water; *panel D*: chromatogram of a cell touched with fingers without gloves, and *panel E*: record of water after washing of a montmorillonite catalyst. Numbers 1–9 mark manifold products of mutual reactions in derivatization agent.

A&A 630, A127 (2019)
https://doi.org/10.1051/0004-6361/201935816

Astronomy & Astrophysics

Main spectral features of meteors studied using a terawatt-class high-power laser

M. Ferus[1], P. Kubelík[1,4], L. Petera[1,2], L. Lenža[1,3], J. Koukal[1,3], A. Křivková[1,7], V. Laitl[1], A. Knížek[1,2], H. Saeidfirozeh[1], A. Pastorek[1,7], T. Kalvoda[1,2], L. Juha[4,5], R. Dudžák[4,5], S. Civiš[1], E. Chatzitheodoridis[6], and M. Krůs[5]

[1] J. Heyrovský Institute of Physical Chemistry, Czech Academy of Sciences, Dolejškova 3, 18223 Prague 8, Czech Republic
e-mail: martin.ferus@jh-inst.cas.cz
[2] Charles University in Prague, Faculty of Science, Department of Physical and Macromolecular Chemistry, Albertov 2030, 12840 Prague 2, Czech Republic
[3] Valašské Meziříčí Observatory, Vsetínská 78, 75701 Valašské, Meziříčí, Czech Republic
[4] Department of Radiation and Chemical Physics, Institute of Physics, Czech Academy of Sciences, Na Slovance 1999/2, 18221 Prague 8, Czech Republic
[5] Institute of Plasma Physics, Czech Academy of Sciences, Za Slovankou 1782/3, 182 00 Prague 8, Czech Republic
e-mail: krus@ipp.cas.cz
[6] National Technical University of Athens, School of Mining and Metallurgical Engineering, 9 Heroon Polytechneiou str., 15780, Zografou Athens, Greece
[7] Czech Technical University in Prague, Jugoslávských partyzánů 1580/3, 160 00 Prague 6, Czech Republic

Received 1 May 2019 / Accepted 17 August 2019

ABSTRACT

Context. Meteor spectra are commonly interpreted using data from databases and tables. Several studies have demonstrated very sophisticated calculations of elemental compositions of meteoroid bodies based on the computation of synthetic meteor spectra or on the spectral analysis of airglow plasma containing evaporated, atomized, and ionized meteoroid matter. However, considering accuracy, reliability of computations, lack of laboratory experimental data in this field, as well as the complicated physical structure of meteor plasma, such qualitative assignment or quantitative calculations are still extensively discussed in the scientific community. Even on the laboratory level, many studies have shown the high complexity of the acquisition and interpretation of the data that are recorded with techniques of emission spectroscopy that are in fashion and philosophy similar to the spectral analysis of meteor plasma, that is, detection and quantification of the elements that are ablated from complicated multicomponent matrices.
Aims. The current study is focused on the application of terawatt-class laser-induced breakdown spectroscopy (TC-LIBS) of real samples of chondritic meteorites. We recorded emission spectra with high resolution and high precision that contain spectral lines that are typical for real meteoric spectra. Experimental data were compiled in a form that is convenient for the meteoric spectra interpretation and calibration.
Methods. TC-LIBS was carried out by a high-power terawatt-class laser facility, the Prague Asterix Laser System (PALS). The spectra were simultaneously recorded by an echelle high-resolution spectrograph in the UV/VIS spectral ranges and by a low-resolution spectrograph that was used for real observation of meteor spectra. We also present calculated synthetic spectra based on data from the NIST atomic spectra database.
Results. We assembled etalon qualitative tables of major meteoric spectral features that can be used both for the spectral wavelength calibration of low-resolution observational instruments and for the exact interpretation of meteor spectra. The data are compared with real meteor spectra.

Key words. atomic data – meteorites, meteors, meteoroids

1. Introduction

Meteor observation and spectroscopy is a highly important astronomical discipline. To date, most observational data are interpreted theoretically, and experimental work is lacking in this field. An in-depth analysis of meteor spectra can be used for example for basic qualitative or quantitative elemental analyses and characterization of meteoroids and their parent bodies, i.e., asteroids and comets. Asteroids and comets are remnants of the protoplanetary disk that formed the planetesimals and planets. Therefore, meteorites allow us to discover details about the properties of this disk as well as its history, that is, the physical and chemical evolution of the solar system. However, even in the rare cases when a piece of meteorite is found, the fundamental problem of linking specific meteorites to their parent bodies remains (interplanetary matter, asteroids, or comet nuclei). Most bodies are evaporated and completely disintegrated during their descent, and their emission spectra, measured using spectrographs, are the only record of their chemical composition. When the trajectory is recorded alongside with the emission spectrum and if chemical composition is correctly interpreted, these data can provide detailed information about the chemical properties of its source in interplanetary space. Determination of the elemental composition provided by emission spectra analysis of the plasma formed above the surface of the evaporated object (meteor) is practically similar to laboratory laser-induced

breakdown spectroscopy (LIBS) elemental spectral analysis. In our recent pilot studies, we focused on the application of the calibration-free LIBS method in the interpretation of meteor spectra and the calculation of the elemental composition of meteoroids (Ferus et al. 2017a, 2018a). The method has been identified as feasible, but relatively time-demanding computation is still necessary. Ciucci et al. (1999), Tognoni et al. (2010), Giacomo (2011), Dell'Aglio et al. (2014), Horzňáčková et al. (2014), Ozdín et al. (2015) and Takahashi et al. (2015) provided a LIBS chemical analysis of meteorites and identified many advantages of this method, such as the applicability for a real-time in situ analysis without any preceding treatment, preparation, or isolation. On the other hand, as concluded in Tognoni et al. (2010) and references therein, even if the LIBS method is operated under strictly laboratory controlled conditions, the emission intensity of a particular spectral line, which is the main factor that influences the quantitave analysis, depends not only on the physical parameters of the spectral transition and the quantity of the emitting element, but also on the matrix in which the element is embedded. This influence of the matrix means that calibration curves or matrix-matched standards are required, which are not available in some practical situations, including meteorite samples. A coincidence of spectral lines in multicomponent analysis also complicates or even renders impossible a qualitative analysis of the spectra when low-resolution data are used. Although several studies have been published by only a few experts, such as Borovička et al. (1999), Jenniskens (2007), and Madiedo et al. (2014, 2013a,b), it was Ferus et al. (2018b) who demonstrated that a qualitative and quantitative analysis of mainly high-quality emission spectra that are assigned to the most abundant class of ordinary chondrites is possible. Many spectra of meteors are still classified as "unusual" and difficult to interpret.

The simulation of the chemical and physical consequences analogous to plasma formed by hypervelocity meteoroids or asteroids entering the Earth's atmosphere by terawatt-class laser introduces a novel experimental approach also in the research of meteor spectra. In the past two decades, our team demonstrated several experiments that mostly focused on the chemical transformations of the atmosphere or on the interaction with solid or liquid surfaces (Babánková et al. 2006a). Most studies have been focused on impact-induced synthesis of biomolecules (Šponer et al. 2016; Ferus et al. 2017b) such as canonical nucleobases in Ferus et al. (2012, 2014a,b, 2015, 2017b), sugars in Civiš et al. (2016a), and aminoacids in Civiš et al. (2004), or the transformation of atmospheric molecules on early terrestrial planets (Civiš et al. 2008) such as the formation or decay of prebiotic substances, for instance, formamide (Ferus et al. 2011), isocyanic acid (Ferus et al. 2018a), and the transformations of hydrogen cyanide (Ferus et al. 2017c), acetylene (Civiš et al. 2016b), methane (Civiš et al. 2017), or carbon monoxide (Civiš et al. 2008; Ferus et al. 2009). Pyrometric measurement of dielectric breakdown induced by high-power terawatt-class lasers in the gas phase has shown that airglow temperatures of 4500 K (Babánková et al. 2006b) are very close to the low-temperature component in meteor spectra that exhibits 3800–6000 K independent of the mass of the impacting body or its velocity (specifically in the ranges of 35 and 72 km s^{-1} and masses between 1025 g and 1 g, according to Jenniskens et al. 2004). A spectroscopic survey of high-power terawatt-class laser plasma interaction with samples of meteorites has not been explored spfar. Several studies that focused on the simulation of high-density energy events connected with asteroid or meteoroid bodies have been published. Zakharov (2003) concluded that among other phenomena such as barium releases from the Earth's magnetosphere, collisionless deceleration of supernova remnants or related shock-wave generation in the interstellar medium, near-Earth anti-asteroid explosions could be also reproduced in the laboratory using laser experiments. Milley et al. (2007) simulated meteor luminosity through laser ablation of meteorites. The first comprehensive work proposing that laboratory-based laser ablation techniques can be used not only to study the size of the luminous region, but also to predict spectral features, estimate the luminous efficiency factor, and assess the role of chemically differentiated thermal ablation of meteoroids was published by Hawkes et al. (2007). Ebert et al. (2017) simulated the virtually instantaneous melting of target rocks during meteorite impacts. They discovered that the entropy changes for laser-melting of a sandstone and an iron meteorite correspond to a minimum impact velocity of 6 km s^{-1}, inducing peak shock pressures of 100 GPa in the target.

Alongside with these studies, the simulation of space weathering together with the deflection of asteroids by lasers remains the most frequently studied research topic connected with application of lasers in this field (Park & Mazanek 2003). Recently, Aristova et al. (2018) studied impact physics of nuclear explosion on hazardous asteroids, Moroz et al. (1996) simulated using laser ablation optical effects of impact melting and repeated crystallization on asteroidal surfaces, and Kurahashi et al. (2002) conducted laser ablation laboratory simulation of space weathering focused on finding the source of the difference between reflectance spectra of ordinary chondrites and their parent bodies, i.e., S-type asteroids. Loeffler et al. (2008) studied the effect of the redeposition of impact-ejecta on mineral surfaces using laser ablation.

To facilitate the understanding of meteor spectra and in order to increase the precision of the qualitatively assigned emission, we employed a high-power terawatt-class laser that can generate in one shot large volumes of plasma under strictly defined conditions. Alongside with the more than 1000× higher power in comparison with classical laboratory lasers, our terawatt-class laser-induced breakdown spectroscopy (TC-LIBS) also provides a great advantage in evaporation of a significantly larger area of the meteorite specimen. This occurs in a manner entirely to that induced by the plasma that is generated during meteoroid descent. Spectra have been recorded in situ by modern high-resolution echelle spectrograph alongside with a low-resolution astronomical meteor spectrograph that was used for the observation of real meteors. The current study provides a catalog of emission lines that we recorded in our experiments and highlights how low-resolution data can be interpreted.

2. Experimental details

Samples of chondrite metorites (see Table 1) were ablated by sub-nanosecond laser pulses (pulse duration 300 ps, wavelength 1.315 μm) with an energy of 600 J generated by the high-power TW-class facility Prague Asterix Laser System (PALS; Jungwirth et al. 2001). The intensity of the laser radiation focused on the surface of a meteorite specimen reached 2.2 TWcm^{-2}. The experimental setup is depicted in Fig. 1. TC-LIBS spectra were simultaneously recorded by a high-resolution echelle spectrograph and the astronomical meteor spectrograph that was employed in spectroscopic surveys of meteors in direct observation. The instrumental equipment and methods are described in the following two subsections. The TC-LIBS spectra of these chondritic meteorites were then averaged in order to obtain the appropriate signal-to-noise ratio and

Table 1. Elemental composition of the meteorites used to calculate the synthetic spectra.

Type	Specification	Mg	Fe	Si	Ca	Cr	Mn	Ni	Na	Reference
CK5	NWA 8214	1	0.704	0.89	0.119	0.011	0.009	0.017	0.056	This work
CM2	DHO 1994	1	0.693	0.917	0.197	0.011	0.009	0.038	0.037	This work
CV3	NWA 3118	1	0.918	1.017	0.073	0.015	0.009	0.027	0.027	This work
CO3	JAH 815	1	0.718	0.939	0.094	0.013	0	0.042	0.045	This work
H3	SAU 567	1	0.65	0.975	0.053	0.009	0.008	0.036	0.082	This work
L3	RAS 445	1	0.608	0.991	0.071	0.013	0.009	0.048	0.067	This work
L3	SAU 571	1	0.682	1.054	0.07	0.011	0.009	0.033	0.092	This work
H	NWA 8212	1	0.408	1.104	0.052	0.012	0.009	0.014	0.065	This work
Av. spec.		1	0.673	0.986	0.091	0.012	0.008	0.032	0.059	This work
L		1	0.628	1.075	0.053	0.012	0.008	0.033	0.05	Drouard et al. (2018)
LL		1	0.547	1.082	0.056	0.013	0.006	0.024	0.051	Drouard et al. (2018)
H		1	0.855	1.045	0.054	0.012	0.007	0.047	0.048	Drouard et al. (2018)
CM		1	0.753	0.967	0.066	0.012	0.006	0.042	0.027	Drouard et al. (2018)
HED		1	1.5	4.796	1.086	0.025	0.046		0.076	Drouard et al. (2018)
	PER2015	1	1	3	0.52	0.001	0.086	0.02	0.02	Ferus et al. (2018b)
	PER1	1	0.778	0.926	0.036	0.009	0.002		0.074	Trigo-Rodriguez et al. (2004a)
	PER2	1	0.807	1.136	0.02	0.009	0.003		0.08	Trigo-Rodriguez et al. (2004a)
	PER3	1	1.024	1.176	0.032	0.011	0.009		0.094	Trigo-Rodriguez et al. (2004a)
	PER4	1	1.01	1.031	0.062	0.011	0.006	0.015	0.113	Trigo-Rodriguez et al. (2004a)
	PER5	1	1.048	1.205	0.025	0.01	0.005	0.041	0.084	Trigo-Rodriguez et al. (2004a)
	LEO	1	1	1.3	0.12	0.001	0.081	0.02	0.01	Ferus et al. (2018b)
	LEO	1	1.025	1.266	0.033	0.005	0.009		0.101	Trigo-Rodriguez et al. (2004a)
	AND	1		1.176	0.015	0.009	0.01	0.019	0.094	Trigo-Rodriguez et al. (2004a)
	SPO2	1		2.564	0.028	0.028	0.018	0	0.282	Trigo-Rodriguez et al. (2004a)
	SPO1	1	0.879	1.099	0.026	0.009	0.006	0.016	0.11	Trigo-Rodriguez et al. (2004a)
	SPO3	1		1.124	0.027	0.007	0.007	0.026	0.09	Trigo-Rodriguez et al. (2004a)
	SPO3r	1		0.947	0.034	0.006	0.007	0.02	0.076	Trigo-Rodriguez et al. (2004a)
	SPO4	1	1.492	1.639	0.061	0.01	0.009	0.041	0.148	Trigo-Rodriguez et al. (2004a)
	Geminid 200111	1	1	1.16	0.04		0.008	0.08	0.03	Madiedo et al. (2013b)
	Geminid 151209	1	0.909	1.055	0.027		0.007	0.027	0.055	Madiedo et al. (2013a)
	GEMr	1	1.111	1.289	0.020		0.005		0.133	Trigo-Rodriguez et al. (2004b)

the qualitative average analysis that is representative for a spectrum of a chondrite meteorite. These data qualitatively provide spectral features that are expected in the emission from the meteor plasma. These spectra and their recorded dominant features were compared with the average synthetic spectrum calculated for a wide range of temperatures and averaged for the chemical composition of a chondrite in Table 1. Elemental composition of the particular chondrite meteorite studied in this work by TC-LIBS was examined using an energy dispersive analysis (EDS). The physical constants for this calculation were taken from the NIST (National Institute of Standards and Technology) database. We would like to highlight that the intention of this work is in the first place to provide a qualitative catalog of spectral features, their experimental measurement, and their comparison with synthetic spectra. A quantitative comparison of spectra recorded for a particular specimen that is ablated by high-power TW-class laser, but also by a standard laboratory Nd:YAG laser, an excimer laser and a femtosecond Ti:Sapphire TW-laser will be provided in a follow-up study.

2.1. Simulation of meteor plasma using the PALS laser facility

The plasma creation and radiation during the meteoroid descent in the atmosphere was simulated using the high-power laser PALS. The laser beam was focused by a plano-convex lens ($f/2, f = 60$ cm) on the target, which was positioned out of focus; the spot size was 1 cm in diameter. All the experiments were performed under pressure of 2 mbar, corresponding to the altitudes that are typical for the very early stages of ablation of the meteoroid body ablation (above 110 km).

2.2. Optical emission spectroscopy of laser-induced breakdown plasma

Complex spectra within the entire UV/VIS range have been recorded by the High Resolution Echelle Spectra Analyzer ESA 4000 (LLA Instruments GmbH, Germany). The optical analyzer unit enables a spatially and temporally resolved image at the lowest spectral intensities. The resolution ranges from a few pm in the range 200–780 nm with resolution of 0.005 nm (200 nm) to 0.019 nm (780 nm). Simultaneously, the spectra were recorded for direct calibration by our astronomical meteor spectrograph that is directly employed in the observation of real meteors for comparative measurements. The spectrograph is based on the high-resolution camera PointGrey Grasshoper3 GS3-U3-32S4M-C with high quantum efficiency (QE = 76%, 525 nm), dynamical range (71.34 dB), with CMOS chip Sony Pregius 2048×1536 px, and a grating of 1000 lines mm^{-1}, which allows a resolution of 0.48 nm px^{-1}. The spectral intensity recorded by the instrument is calibrated using standard sources, such as a deuterium lamp, a tungsten source and calibration using standard spectra of Venus. Wavelength calibration is achieved using high-resolution data and standard wavelengths of calibration sources (deuterium lamp). In our measurements, for every meteorite sample, the echelle spectrograph was set to trigger 1 μs after the laser pulse with the gate open for 4 μs for a total accumulation of one signal after one large laser shot. The PALS high-power

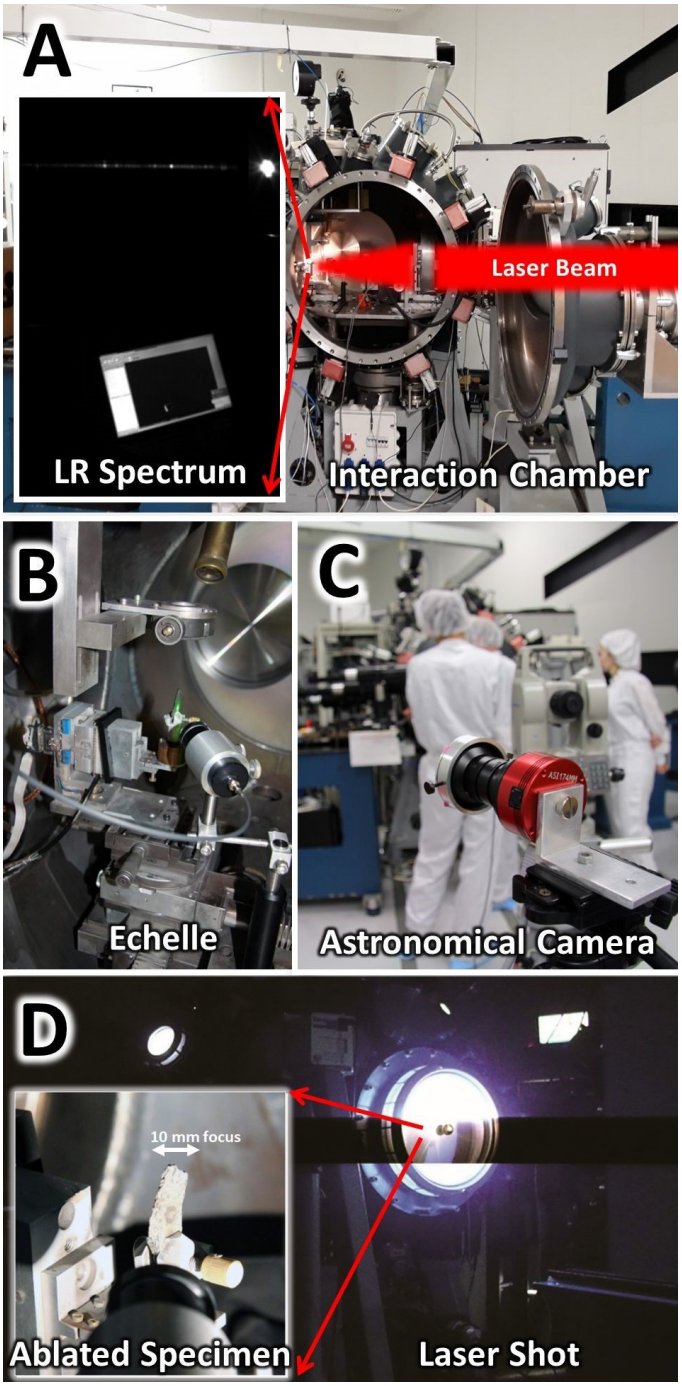

Fig. 1. *Panel A*: vacuum interaction chamber with ablation set-up. A photography of a spectrum is shown in the embedded picture (left). *Panel B*: detailed experimental set-up with a collimator of Echelle spectrograph. *Panel C*: low resolution astronomical camera for comparative measurement. *Panel D*: sample of a meteorite prepared for the TC-LIBS experiment (left), high-power laser induced dielectric breakdown inside the interaction chamber (right).

laser provides a single 600 J-laser shot every 30 min. The low-resolution astronomical meteor spectrograph opened the gate for 1 s after it was triggered by the laser system.

2.3. Bulk elemental analysis of chondrite samples

Chemical analyses of meteorites were provided by secondary and backscatter electron imaging (SEI/BSE) conducted with the JEOL JSM-6380 LV SEM system at the National Technical University of Athens, Greece. This system is equipped with the Energy Dispersive X-Ray Analysis (EDX) from Oxford Instruments, and it is controlled by the INCA software. Prior to any quantitative chemical analyses the instrument was calibrated using a set of mineral standards. Analyses were performed in high vacuum, with an electron beam size of about 1 μm and accelerating voltage of 20 kV. The beam current was generally set between 1–2 nA, and the analytical integration time was 120 s. The bulk analysis was performed by acquiring an X-ray spectrum while scanning and averaging an area of 100 mm^2.

3. Calculating the synthetic spectra

The measured high-resolution emission spectra were compared with the synthetic spectra calculated from high-precision data obtained from the NIST atomic spectral database (Kramida et al. 2018). This approach greatly facilitates the orientation in the experimental data because the user can visually quickly compare the measured spectra with the standard spectra from the database; in addition to this advantage, the positions of the simulated peaks can be also used as standard values for the wavelength calibration of the observed spectra. This subsection describes how the synthetic spectra were obtained.

The synthetic spectra were generated as a sum of the individual peaks corresponding to the energy transitions that are included in the simulation. The intensity of each peak was calculated according to the equation

$$I_{\mathrm{ul}} = \frac{hc}{4\pi\lambda_{\mathrm{ul}}} A_{\mathrm{ul}} g_u N_i \frac{e^{\frac{-E_u}{kT}}}{Q(T)_i} \quad (1)$$

where I_{ul}, h, c, λ_{ul}, A_{ul}, g_u, N_i, E_u, k, T, and $Q(T)_i$ are the emission intensity, Planck's constant, the speed of light in vacuum, the transition wavelength, the Einstein A-coefficient of the transition, the g-factor of the upper energy level, the number of the particles in ionization state i, the energy of the upper level, the Boltzmann constant, temperature, and the partition function of the ionization state, respectively. The simulation assumed a local thermodynamic equilibrium and optically thin conditions where no self-absorption effects are present. The N_i value was calculated as the product of the abundance of the specific element and the relative abundance of the ionization states produced by ionization of the neutral atoms of the element. The relative concentrations of the ionization states were calculated according to the Saha equation. Synthetic spectra were calculated based on elemental abundances measured in our laboratory for several samples of chondritic meteorites by means of energy dispersive analysis (EDS). These specimens were also used for ablation by the PALS laser. The average elemental composition is shown in the Table 1 and compared with values from the current literature.

The values of the electron density were set to 1×10^{14} cm^{-3}, which is a typical value for the meteoric plasma (Borovička 1994). The synthetic spectra are provided in three different temperatures: 4000 K, which is typical for the lower temperature component of the meteoric spectra, 7000 K, which is often observed in our ablation experiments, and 10 000 K, which is near the value estimated for the so-called higher temperature component of the meteoric spectra (Borovička 1994). The maximum ionization degree of the species considered in this simulations was 1 (e.g., Ca II). Because the spectral resolution of most of the observation cameras used today is still lower than 1 nm px^{-1}, the observed spectral peak profiles are still strongly

influenced by the instrumental function of these spectrometers. For this reason, the simplest possible (Gaussian) peak profile was chosen as the profile function. The FWHM of the peaks was set to the same value as the spectral resolution of our observation camera used in this experiment (0.48 nm px^{-1}).

4. Results and discussion

4.1. Compilation of the spectral features

Although the meteoric spectra show considerable variability, certain groups of commonly observed spectra can be identified. The spectral features in this work are presented in the form of groups of spectral lines that occur in narrow spectral regions between approximately 370 and 660 nm.

The purpose of this data compilation is to provide a detailed description of the selected spectral features in terms of assignment to the energy transitions that contribute significantly to the appearance of the most frequently observed spectral lines in the meteor spectra. As candidates for the most prominent meteoric spectral features, the lines listed in the literature (Vojáček et al. 2015; Ceplecha 1971, 1966; IMC 2015[1]) were selected. For an overview of all the selected spectral features, see Fig. 2, where our laboratory low-resolution spectrum acquired with the observation camera is compared to the real spectra of several meteors (Ferus et al. 2018a).

Because this study uses extensively the experimental data measured by the TC-LIBS of real meteoritic samples, we mainly focussed on the spectral lines assigned to the metalic species. The spectral lines of atmospheric gases that are also observed in meteoric spectra are included, but they are not paid much attention.

All the spectral features are listed in the Table A.1. Each feature is composed of one or more spectral lines that can include several energy transitions. The features are separated by horizontal lines that reach over all the table columns. Each feature is labeled by a tag (F1, F2, etc.) that serves as its reference in the text and figures. Each feature in the table is accompanied by a figure (Figs. B.1–B.4). All the marked peaks (their positions and heights) are listed in the corresponding part the Table A.1. In addition to the experimental and simulated spectra, the individual energy transitions are plotted (as a stick diagram). The columns of Table A.1 can be divided into two main groups. The first group contains the data of the energy transitions, and the second group collects the information about the selected spectral lines (peaks). Each spectral line can be composed of several energy transitions. The table lines (transitions) contributing to a specific peak are separated by one column spanning horizontal lines in the last four columns of the table (peak wavelengths and intensities). Each peak begins at the row of the table where the values of its wavelength and height are written and ends at the nearest following horizontal line. The beginning and end of each peak were determined by the nearest left and nearest right local minima, respectively. Lines that can be observed too far from the listed transitions are not included in the table, nor are they marked in the figures.

Only transitions with known Einstein A-coefficients were added into the table. Moreover to simplify the present table we included only the energy transitions gathered from the NIST Atomic Spectral Database Kramida et al. (2018) whose intensities (calculated using the Eq. (1)) are higher than 10% of the maximum calculated intensity within the particular spectral feature. Similarly, only the peaks exceeding the height of 10% of the highest peak in the feature are selected.

[1] International Meteor Conference (IMC) 2015 (Mistelbach, Austria, August 27) (IMO), 16–23.

4.2. Description of spectral features

This section contains a brief description of the selected spectral features. Only interesting or doubtful cases are listed.

- F1 (371.58–375.35 nm): almost only lines of Fe I.
- F2 (381.64–389.03 nm): the low-temperature lines of Mg I and Fe I, which partially overlap.The lines of Si II can also become important at higher temperatures.
- F3 (392.95–397.19 nm): typical for fast meteors. The most significant lines belong to the Ca II doublet. These lines are overlapped by two Al I lines of comparable intensity, however. This may cause difficulties when the lines are used for the quantitative analysis.
- F4 (402.69–406.74 nm): the low-temperature lines of Fe I and Mn I.
- F5 (412.68–413.50 nm): the fast meteor feature, the Si II line (higher temperatures), is very close to a line of Fe I, which is much more intensive at lower temperatures, however.
- F6 (419.67–432.97 nm): low-temperature lines of Fe I, Ca I, and Cr I.
- F7 (437.18–440.89 nm): low-temperature and weak lines of Fe I; at higher temperatures, lines of Mg II and Fe II can apear.
- F8 (441.65–448.44 nm): fast meteors, contains the low-temperature lines of Ca I and Fe I, at higher temperatures, lines of Mg II can appear. The measured high-resolution spectrum also contains one significant peak that can be assigned to Mn I energy transitions.
- F9 (451.61–454.40 nm): low-temperature lines of Ca I and Fe I. At high temperature, the lines of Fe II become more significant. The measured high-resolution spectrum also contains one significant peak that was not selected and included in the table because the Einstein A-coefficient of the nearby Fe I transition is missing.
- F10 (469.90–470.70 nm): low-temperature lines of Mg I.
- F11 (486.80–496.16 nm): low-temperature lines of Fe I. At high temperature, the line of Fe II becomes more significant.
- F12 (500.74–502.11 nm): fast meteors, Fe I and Fe II lines, together with transitions of Ti I, can also contribute to the lines observed in this spectral region.
- F13 (510.59–511.49 nm) contains Fe I and Fe II transitions.
- F14 (516.33–522.41 nm): low-temperature and weak lines of Mg I, Fe I, and Cr I.
- F15 (526.49–527.34 nm): low-temperature Fe I lines, lines of Ca I are also of comparable intensity in this spectral region.
- F16 (532.60–533.60 nm): lines of atmospheric O I (at higher temperatures) and Fe I (lower temperatures).
- F17 (536.75–545.96 nm): in this spectral region and at low temperature Fe I, Cr I lines are most significant. At high temperature, the lines of Fe II become more significant.
- F18 (552.10–553.40 nm): the dominant Mg I line.
- F19 (557.29–561.94 nm): the dominant lines in this spectral region belong to Ca I and Fe I. At high temperature, the lines of Fe II can appear.
- F20 (588.60–589.98 nm): low-temperature Na I lines (usually a very intensive feature).
- F21 (623.10–624.42 nm): low-temperature lines of Fe I. At high temperature, the lines of Fe II and Si II can appear.

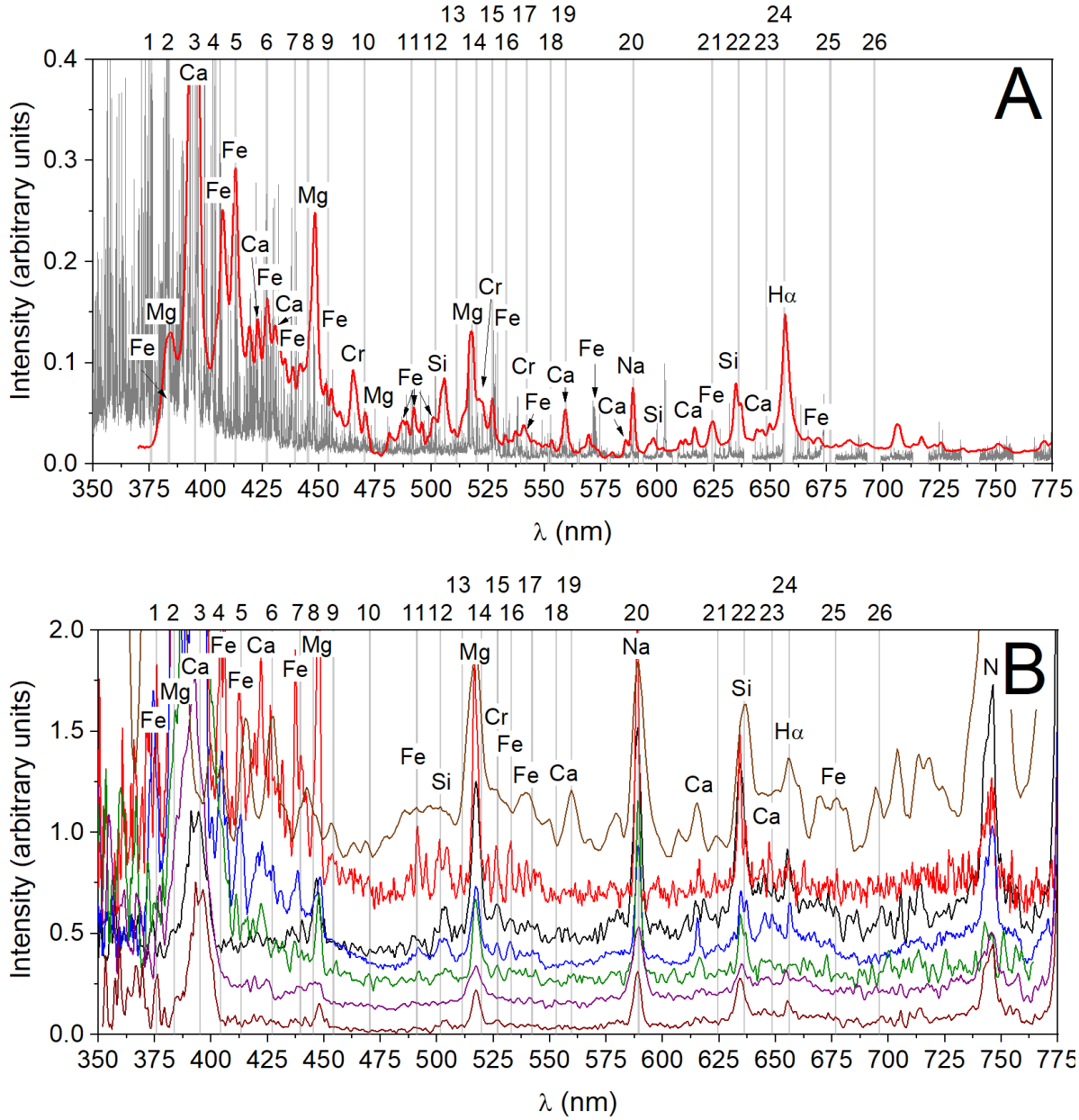

Fig. 2. *Panel A*: high-resolution (gray) together with the low-resolution (red) spectrum. The most significant spectral lines are labeled. *Panel B*: examples of spectra recorded by observational spectographs. Starting with the upper spectrum of Perseid 20150811_014658 (brown), Sporadic 20161227_020734 (red), Perseid 20150812_231001 (black), Leonide 20161117_042009 (blue), Ursae Majorid 20161213_014212 (green), Alpha Camelopardalid 20161002_013415 (purple), and Perseid 20150812_232102 (wine). Overview of the selected spectral features (marked with gray lines). The detailed description of the individual spectral lines is provided in Table A.1.

F22 (634.32–637.52 nm): fast meteors, high-temperature lines of Si II.

F23 (645.24–649.88 nm): lines of atmospheric O I and N I, but the lines of Ca I and Fe I are also present in this region.

F24 (655.88–656.69 nm): fast meteors, H I lines. At the experimental spectrum only the left wing of the spectral line can be seen.

F25 (674,55–679,41 nm): low-temperature lines of Fe I and Ni I. At higher temperature, the lines of Mg II and N I can appear.

F26 (693.72–698.59 nm): in this spectral region and at low temperature Fe I, Cr I lines are most significant. At high temperature, the lines of Fe II and N I become more significant.

4.3. Meteor spectra in the laboratory: advantages, challenges, and limitations

Evaluating meteor emission spectra is a very complex scientific problem. Our experimental spectra depicted in panel A of Fig. 2, as well as several examples of spectra recorded by observational spectrographs in panel B, exhibit a series of overlapping bands that are typical for complex multicomponent matrices. Our experimental data as well as their comparison with synthetic spectra calculated using the NIST database show that position, range, and intensity of many spectral features can depend not only on the chemical composition of the meteoroid body, but also on their overlapping and on the temperature of the plasma. Meteor spectra recorded by the low-resolution observational camera were obtained by the analysis of a spectrum photogra-

phy. For this analysis, theoretical tables cannot serve as calibration spectroscopic standard. Experimental LIBS of chondrites by terawatt-class laser and their assignment introduced in this study can therefore help with the precise assignment of spectral lines. In Table A.1 we show that wavelenghts assigned to features observed in meteor spectra can differ. Experimental data can provide a standard for the spectral assignment for such complicated and complex matrices. Experimental data also show that considering intensity and number of spectral features in UV region between 115–400 nm, accuracy and sensitivity of meteor spectroscopy could be improved by measuring in this range. However, this is beyond the capabilities of the current instrumentation; detection outside Earth's atmosphere using very high-resolution spectrographs are required. Standard observational cameras operate in the 400 nm to 780 nm region, and emission lines above 300 nm are significantly attenuated by absorption in atmospheres as well as by the decreasing sensitivity of detectors. On the other hand in regions of longer wavelengths we performed in our laboratory systematic studies of the Rydberg states of atoms in the near- and mid-infrared ranges (NIR and MIR) (Civiš et al. 2011, 2012a,b,c,d, 2013a,b) (e.g., Fourier transform type) (Kawaguchi et al. 2008; Civiš et al. 2012e,c,f). Molecules and atomic species exhibit strong emission spectra under these conditions. In this manner, the elemental and molecular compositions of the objects can be simultaneously studied in the NIR and MIR regions. However, there are several limitations: the emission spectra of atoms are either not known or they are not assigned to Rydberg states that emit infrared radiation.

We supply a comparison of averaged spectra recorded by TC-LIBS of chondrite specimens with a selection of several spectra of meteors recorded at the Observatory Valašské Meziříčí (Czech Republic, Moravia - Zlín Region, GPS 49.46373, 17.97366). Our TC-LIBS measurements exhibit a wide range of emission lines. The most intense include Fe I, II, Mg I, II, Ca I, II, Mn I, Si II, Cr I, II, Ti I, Al I, Na I, H I, and N I, II (as described in Sect. 4.2, Figs. 2 and B.1–B.5, and Table A.1). However, we should note that several studies reported a number of rather extraordinary spectra: For instance, our experiments always exhibit intense sodium lines. Meteors with expected chondrite composition exhibit either a lack of sodium (Borovička et al. 2005) or a high concentration of sodium is described (Trigo-Rodriguez & Llorca 2007). The effect is explained by the depletion in Na through the exposure to solar radiation. Other meteors are classified based on the spectra by iron (in agreement with common meteorite classification). They are classified into mainstream and normal (with expected composition close to chondritic), and Fe poor (Vojáček et al. 2015). The TC-LIBS experiments will also facilitate a more precise classification, when the results are also connected with an abundance determination of particular elements. In these investigations, the simulation of relatively optically thin plasma around the path of the meteor is another challenging experimental problem.

Laboratory studies focused on meteor plasma are complicated by the fundamental problem connected with every experimental work: achieving experimental conditions as close to the real system as possible. The large volume of plasma produced by a terawatt-class laser exhibits a temperature of 9600 K and expands to 6 km s^{-1} (based on the Doppler shift of the spectral lines). Furthermore, regarding the high-energy output of 600 J of a terawatt-laser, this device is powerful enough to ablate significantly large areas of about 1 cm^2 of meteorite. This is similarly to the ablation of small meteoroid bodies in the atmosphere. This is not possible with common laboratory lasers. These conditions can serve as a kind of simulation of the frontal shock wave region of the meteor.

This frontal shockwave contributes to the high-temperature component in meteor emission spectra. Two meteor spectral components were described by Borovička et al. for the first time in 1993 (Borovička 1994; Borovička & Betlem 1997; Borovička et al. 1999; Berezhnoy & Borovička 2010). The intense low-temperature component exhibits an excitation temperature ranging from 2900 K (lower extreme) to 6200 K (higher extreme) with a typical value of about 4500 K. Jenniskens et al. (2004) discovered a slight increase in the temperature with decreasing meteor altitude, but otherwise nearly constant values for meteoroids with speeds between 35 and 72 km s^{-1} and masses between 1025 g and 1 g. However, Ceplecha (1965) observed a decrease in the excitation temperature as a function of meteor luminosity and also reported a temperature of atomic oxygen lines in airglow plasma of about 14 000 K. Typical lines of the second component make up only 0.02% of the meteor vapor envelope in slow meteors, but account for more than 5% in fast meteors (Borovička 1994). These lines consist of high excitation of H I, Mg II, Si II, or Ca II that is also observed in the spectra of TC-LIBS recorded in this work. However, they are also mixed with a series of neutral lines in our case. We should note that global spectroscopic observations still oversimplify the much more complicated structure as well as temperature distribution in the plasma fireball that surrounds the meteoroid. The problem is described in detail in a recent comprehensive review by Silber et al. (2018). Our pilot study of TC-LIBS again opens this topic. TC-LIBS will certainly offer a unique opportunity to study the complicated phenomenon of meteoroid surface ablation under strictly controlled laboratory conditions on the macroscopic scale of large laser sparks.

5. Conclusions

We presented a compilation of the dominant spectral features of the plasma produced by ablation of chondrite meteoroids. Laboratory simulations of meteor plasma were performed by ablating of several specimens of chondrite meteorites by the high-power terawatt-class laser facility PALS. They reached the energy of 600 J and an output intensity of 2.2 TWcm^{-2} when focused on an area of 1 cm^2 of the meteorite specimen. The produced ablation plasma attained the temperature of 9600 K and plasma expanded with a velocity of 6 km s^{-1}. Spectra were recorded by the high-resolution echelle spectrograph, and for comparison and calibration, spectra were also recorded by the astronomical meteor spectrograph. All the spectral features were interpreted by synthetic spectra that were calculated based on the data from the NIST atomic spectra database. In this manner, we provide a data set for the evaluation of observational spectra that are recorded by the meteor spectrographs. Experimental spectra were also compared with selected meteor spectra.

Acknowledgements. This paper has been published as part of research series supported by the Czech Science Foundation within the project reg. no. 18-27653S, Programme of Regional Cooperation between the Regions and the Institutes of the Czech Academy of Sciences in 2018 (projects no.: R200401721 and R200401801), ERDF/ESF "Centre of Advanced Applied Sciences" (No. CZ.02.1.01/0.0/0.0/16_019/0000778) and Ministry of Education, Youth and Sports – PALS RI (LM2015083). Moreover, we would like thank to PALS crew: J. Skála, J. Mareš, P. Prchal, M. Červeňák, J. Golasowski, J. Hřebíček for their help and support. *Contribution Statement.* MF invetended the research, conducted the experiments, evaluated the data, and wrote the paper, PK conducted the experiments, conducted the spectra simulation, and wrote the

paper, LP, LL, JK, AK, AP, JH, TK, SC participated in the experiments, AK evaluated the data and wrote the paper, HS wrote the paper, LJ, RD contributed from the side of the PALS facility, EC conducted EDS and wrote the paper, MK supervised and conducted experiments in the PALS facility and wrote the paper.

References

Aristova, E. Y., Aushev, A. A., Baranov, V. K., et al. 2018, J. Exp. Theor. Phys., 126, 132
Babánková, D., Civiš, S., & Juha, L. 2006a, Prog. Quantum Electron., 30, 75
Babánková, D., Civiš, S., Juha, L., et al. 2006b, J. Phys. Chem. A, 110, 12113
Berezhnoy, A. A., & Borovička, J. 2010, Icarus, 210, 150
Borovička, J. 1994, Planet. Space Sci., 42, 145
Borovička, J., & Betlem, H. 1997, Planet. Space Sci., 45, 563
Borovička, J., Stork, R., & Bocek, J. 1999, Meteorit. Planet. Sci., 34, 987
Borovička, J., Koten, P., Spurný, P., Boček, J., & Štork, R. 2005, Icarus, 174, 15
Ceplecha, Z. 1965, Bull. Astron. Inst. Czechosl., 16, 88
Ceplecha, Z. 1966, Bull. Astron. Inst. Czechosl., 17, 195
Ceplecha, Z. 1971, Bull. Astron. Inst. Czechosl., 22, 219
Ciucci, A., Corsi, M., Palleschi, V., et al. 1999, Appl. Spectros., 53, 960
Civiš, S., Juha, L., Babánková, D., et al. 2004, Chem. Phys. Lett., 386, 169
Civiš, S., Babánková, D., Cihelka, J., Sazama, P., & Juha, L. 2008, J. Phys. Chem. A, 112, 7162
Civiš, S., Matulková, I., Cihelka, J., et al. 2011, J. Phys. B: At. Mol. Opt. Phys., 44, 025002
Civiš, S., Ferus, M., Kubelík, P., Chernov, V. E., & Zanozina, E. M. 2012a, J. Phys. B: At. Mol. Opt. Phys., 45, 175002
Civiš, S., Ferus, M., Kubelík, P., Chernov, V. E., & Zanozina, E. M. 2012b, A&A, 545, A61
Civiš, S., Ferus, M., Kubelík, P., Jelinek, P., & Chernov, V. E. 2012c, A&A, 541, A125
Civiš, S., Ferus, M., Kubelík, P., et al. 2012d, A&A, 542, A35
Civiš, S., Ferus, M., Kubelík, P., et al. 2012e, J. Opt. Soc. Amer. B, 29, 1112
Civiš, S., Kubelík, P., & Ferus, M. 2012f, J. Phys. Chem. A, 116, 3137
Civiš, S., Ferus, M., Chernov, V., Zanozina, E., & Juha, L. 2013a, J. Quant. Spectrosc. Radiat. Transfer, 129, 324
Civiš, S., Ferus, M., Chernov, V. E., & Zanozina, E. M. 2013b, A&A, 554, A24
Civiš, S., Szabla, R., Szyja, B. M., et al. 2016a, Sci. Rep., 6
Civiš, M., Ferus, M., Knížek, A., et al. 2016b, Phys. Chem. Chem. Phys., 18, 27317
Civiš, S., Knížek, A., Ivanek, O., et al. 2017, Nat. Astron., 1, 721
Dell'Aglio, M., Giacomo, A. D., Gaudiuso, R., Pascale, O. D., & Longo, S. 2014, At. Spectrosc., 101, 68
Drouard, A., Vernazza, P., Loehle, S., et al. 2018, A&A, 613, A54
Ebert, M., Hecht, L., Hamann, C., & Luther, R. 2017, Meteorit. Planet. Sci., 52, 1475
Ferus, M., Matulková, I., Juha, L., & Civiš, S. 2009, Chem. Phys. Lett., 472, 14
Ferus, M., Kubelík, P., & Civiš, S. 2011, J. Phys. Chem. A, 115, 12132
Ferus, M., Civiš, S., Mládek, A., et al. 2012, J. Am. Chem. Soc., 134, 20788
Ferus, M., Michalčíková, R., Shestivská, V., et al. 2014a, J. Phys. Chem. A, 118, 719
Ferus, M., Nesvorný, D., Šponer, J., et al. 2014b, Proc. Nat. Acad. Sci., 112, 657
Ferus, M., Knížek, A., & Civiš, S. 2015, Proc. Nat. Acad. Sci., 112, 7109
Ferus, M., Koukal, J., Lenza, L., et al. 2017a, 2017 19th International Conference on Transparent Optical Networks (ICTON) (IEEE)
Ferus, M., Pietrucci, F., Saitta, A. M., et al. 2017b, Proc. Nat. Acad. Sci., 114, 4306
Ferus, M., Kubelík, P., Knížek, A., et al. 2017c, Sci. Rep., 7
Ferus, M., Laitl, V., Knizek, A., et al. 2018a, A&A, 616, A150
Ferus, M., Koukal, J., Lenza, L., et al. 2018b, A&A, 610, A73
Giacomo, A. D. 2011, Spectrochim. Acta Part B, 66, 661
Hawkes, R. L., Milley, E. P., Ehrman, J. M., et al. 2007, Earth Moon Planets, 102, 331
Horzňáčková, M., Plavčan, J., Rakovský, J., et al. 2014, Eur. Phys. J. Appl. Phys., 66, 10702
Jenniskens, P. 2007, Adv. Space Res., 39, 491
Jenniskens, P., Laux, C. O., Wilson, M. A., & Schaller, E. L. 2004, Astrobiol., 4, 81
Jungwirth, K., Cejnarova, A., Juha, L., et al. 2001, Phys. Plasmas, 8, 2495
Kawaguchi, K., Sanechika, N., Nishimura, Y., et al. 2008, Chem. Phys. Lett., 463, 38
Kramida, A., Ralchenko, Y., Reader, J., & NIST ASD Team (2018) 2018, NIST Atomic Spectra Database (version 5.5.6)
Kurahashi, E., Yamanaka, C., Nakamura, K., & Sasaki, S. 2002, Earth Planets Space, 54, e5
Loeffler, M., Baragiola, R., & Murayama, M. 2008, Icarus, 196, 285
Madiedo, J. M., Ortiz, J. L., Trigo-Rodríguez, J. M., et al. 2014, Icarus, 231, 356
Madiedo, J. M., Trigo-Rodríguez, J. M., Castro-Tirado, A. J., Ortiz, J. L., & Cabrera-Caño, J. 2013a, MNRAS, 436, 2818
Madiedo, J. M., Trigo-Rodríguez, J. M., Lyytinen, E., et al. 2013b, MNRAS, 431, 1678
Milley, E. P., Hawkes, R. L., & Ehrman, J. M. 2007, MNRAS, 382, L67
Moroz, L., Fisenko, A., Semjonova, L., Pieters, C., & Korotaeva, N. 1996, Icarus, 122, 366
Ozdín, D., Plavčan, J., Horňáčková, M., et al. 2015, Meteorit. Planet. Sci., 50, 864
Park, S.-Y., & Mazanek, D. D. 2003, J. Guidance Control Dyn., 26, 734
Silber, E. A., Boslough, M., Hocking, W. K., Gritsevich, M., & Whitaker, R. W. 2018, Adv. Space Res., 62, 489
Šponer, J. E., Szabla, R., Góra, R. W., et al. 2016, Phys. Chem. Chem. Phys., 18, 20047
Takahashi, T., Thornton, B., Ohki, K., & Sakka, T. 2015, At. Spectrosc., 111, 8
Tognoni, E., Cristoforetti, G., Legnaioli, S., & Palleschi, V. 2010, Spectrochim. Acta Part B, 65, 1
Trigo-Rodriguez, J., & Llorca, J. 2007, Adv. Space Res., 39, 517
Trigo-Rodriguez, J., Llorca, J., & Fabregat, J. 2004a, MNRAS, 348, 802
Trigo-Rodriguez, J. M., Llorca, J., Borovička, J., & Fabregat, J. 2004b, Earth Moon Planets, 95, 375
Vojáček, V., Borovička, J., Koten, P., Spurný, P., & Štork, R. 2015, A&A, 580, A67
Zakharov, Y. 2003, IEEE Trans. Plasma Sci., 31, 1243

Appendix A: Energy transitions and lines of the spectral features

Table A.1. Spectral features of the meteors.

Label	Specie	Energy transitions								Peaks (experiment)		Peaks (simulation)					
		Lower energy level			Upper energy level			4000 K		High resolution		4000 K		7000 K		10 000 K	
		El. conf.	Term	J	El. conf.	Term	J	λ (nm)	I_{em}	λ (nm)	I_{em}	λ (nm)	I_{em}	λ (nm)	I_{em}	λ (nm)	I_{em}
F1	Fe I	$3d^64s^2$	a ^{5}D	4	$3d^6(^5D)$ 4s 4p (^{3}P°)	z ^{5}F°	5	371.99	1.3e−17	372.00	2.5e−01	372.01	2.6e−17				
	Fe I	$3d^64s^2$	a ^{5}D	2	$3d^6(^5D)$ 4s 4p (^{3}P°)	z ^{5}F°	2	372.26	1.4e−18	372.24	7.4e−02						
	Fe I	$3d^7(^4F)$ 4s	a ^{5}F	5	$3d^7(^4F)$ 4p	y ^{5}F°	5	373.49	6.1e−18	373.49	2.4e−01	373.62	2.4e−17	373.68	1.8e−17	373.69	2.8e−18
	Ca II	$3p^64p$	^{2}P°	3/2	$3p^65s$	^{2}S	1/2	373.69	3.7e−21	373.71	1.9e−01						
	Fe I	$3d^64s^2$	a ^{5}D	3	$3d^6(^5D)$ 4s 4p (^{3}P°)	z ^{5}F°	4	373.71	8.2e−18								
	Fe I	$3d^64s^2$	a ^{5}D	2	$3d^6(^5D)$ 4s 4p (^{3}P°)	z ^{5}F°	3	374.56	4.8e−18	374.55	1.3e−01	374.77	1.5e−17			374.85	4.6e−19
	Fe I	$3d^64s^2$	a ^{5}D	1	$3d^6(^5D)$ 4s 4p (^{3}P°)	z ^{5}F°	2	374.83	2.6e−18	374.83	8.2e−02						
	Fe II	$3d^6(^1D2)$ 4s	c ^{2}D	5/2	$3d^6(^3P2)$ 4p	z ^{2}P°	3/2	374.85	1.5e−26								
	Fe I	$3d^7(^4F)$ 4s	a ^{5}F	4	$3d^7(^4F)$ 4p	y ^{5}F°	4	374.95	3.7e−18	374.95	1.9e−01						
F2	Fe I	$3d^7(^4F)$ 4s	a ^{5}F	5	$3d^7(^4F)$ 4p	y ^{5}D°	4	382.04	4.5e−18	382.04	1.8e−01	382.09	9.6e−18	382.06	1.3e−18		
	Fe I	$3d^64s^2$	a ^{5}D	4	$3d^6(^5D)$ 4s 4p (^{3}P°)	z ^{5}D°	3	382.44	1.8e−18	382.45	5.8e−02	382.51	9.4e−18	383.22	2.5e−18		
	Fe I	$3d^7(^4F)$ 4s	a ^{5}F	4	$3d^7(^4F)$ 4p	y ^{5}D°	3	382.59	2.7e−18	382.59	1.4e−01						
	Fe I	$3d^7(^4F)$ 4s	a ^{3}F	3	$3d^7(^4F)$ 4p	y ^{3}D°	2	382.78	5.3e−19	382.78	1.3e−01						
	Mg I	3s 3p	^{3}P°	0	3s 3d	^{3}D	1	382.94	3.4e−19	382.93	1.3e−01						
	Mg I	3s 3p	^{3}P°	1	3s 3d	^{3}D	1	383.23	2.5e−19	383.23	2.6e−01						
	Mg I	3s 3p	^{3}P°	1	3s 3d	^{3}D	2	383.23	7.6e−19								
	Fe I	$3d^7(^4F)$ 4s	a ^{5}F	3	$3d^7(^4F)$ 4p	y ^{5}D°	2	383.42	1.3e−18	383.42	8.5e−02						
	Mg I	3s 3p	^{3}P°	2	3s 3d	^{3}D	3	383.83	1.4e−18	383.83	3.4e−01	383.78	4.0e−18	383.83	3.3e−18		
	Mg I	3s 3p	^{3}P°	2	3s 3d	^{3}D	2	383.83	2.5e−19								
	Fe I	$3d^7(^4F)$ 4s	a ^{3}F	2	$3d^7(^4F)$ 4p	y ^{3}D°	1	384.10	3.6e−19	384.11	1.2e−01						
	Si II	3s $3p^2$	^{2}D	3/2	$3s^24p$	^{2}P°	3/2	385.37	1.2e−28			385.97	1.8e−17	385.96	8.6e−19	385.59	1.4e−17
	Si II	3s $3p^2$	^{2}D	5/2	$3s^24p$	^{2}P°	3/2	385.60	1.0e−27	385.64	4.5e−02						
	Fe I	$3d^64s^2$	a ^{5}D	3	$3d^6(^5D)$ 4s 4p (^{3}P°)	z ^{5}D°	2	385.64	2.0e−18								
	Fe I	$3d^64s^2$	a ^{5}D	4	$3d^6(^5D)$ 4s 4p (^{3}P°)	z ^{5}D°	4	385.99	8.6e−18	385.99	1.4e−01						
	Si II	3s $3p^2$	^{2}D	3/2	$3s^24p$	^{2}P°	1/2	386.26	4.7e−28							386.25	6.1e−18
	Fe I	$3d^64s^2$	a ^{5}D	2	$3d^6(^5D)$ 4s 4p (^{3}P°)	z ^{5}D°	1	387.86	1.5e−18	387.86	4.6e−02	387.86	2.9e−18				
	Fe I	$3d^64s^2$	a ^{5}D	3	$3d^6(^5D)$ 4s 4p (^{3}P°)	z ^{5}D°	3	388.63	3.3e−18	388.63	8.3e−02	388.63	6.5e−18				
F3	Ca II	$3p^64s$	^{2}S	1/2	$3p^64p$	^{2}P°	3/2	393.37	9.2e−17	393.37	2.3e−01	393.37	1.8e−16	393.37	6.6e−15	393.37	2.1e−16
	Ca II	$3p^64s$	^{2}S	1/2	$3p^64p$	^{2}P°	1/2	396.85	4.7e−17	396.85	3.4e−01	396.85	9.2e−17	396.85	3.3e−15	396.85	1.0e−16
F4	Mn I	$3d^54s^2$	a ^{6}S	5/2	$3d^5(^6S)$ 4s 4p (^{3}P°)	z ^{6}P°	7/2	403.08	8.8e−19	403.09	2.5e−02	403.22	2.9e−18				
	Mn I	$3d^54s^2$	a ^{6}S	5/2	$3d^5(^6S)$ 4s 4p (^{3}P°)	z ^{6}P°	5/2	403.31	6.4e−19	403.32	2.1e−02						
	Mn I	$3d^54s^2$	a ^{6}S	5/2	$3d^5(^6S)$ 4s 4p (^{3}P°)	z ^{6}P°	3/2	403.45	4.1e−19	403.46	2.0e−02						
	Fe I	$3d^7(^4F)$ 4s	a ^{3}F	4	$3d^7(^4F)$ 4p	y ^{3}F°	4	404.58	1.5e−18	404.59	5.1e−02	404.58	3.0e−18	404.58	7.1e−19	404.58	2.5e−20
	Cr II	$3d^5$	b ^{4}D	5/2	$3d^4(^5D)$ 4p	z ^{4}P°	5/2	405.41	2.7e−25							405.41	7.9e−21
	Fe I	$3d^7(^4F)$ 4s	a ^{3}F	3	$3d^7(^4F)$ 4p	y ^{3}F°	3	406.36	7.6e−19	406.37	4.5e−02	406.36	1.5e−18	406.36	3.8e−19	406.36	1.4e−20
F5	Si II	$3s^23d$	^{2}D	5/2	$3s^24f$	^{2}F°	7/2	413.09	2.5e−30	413.09	2.0e−02	413.21	2.6e−19	413.19	7.6e−20	413.09	4.0e−18
	Fe I	$3d^7(^4F)$ 4s	a ^{3}F	2	$3d^7(^4F)$ 4p	y ^{3}F°	3	413.21	1.3e−19	413.21	5.4e−02						
F6	Fe I	$3d^7(^2G)$ 4s	a ^{1}G	4	$3d^7(^2G)$ 4p	z ^{1}H°	5	419.91	1.5e−20	419.91	2.8e−02						
	Fe I	$3d^7(^4F)$ 4s	a ^{3}F	4	$3d^7(^4F)$ 4p	z ^{3}G°	4	420.20	1.9e−19	420.21	3.1e−02						
	Ca I	$3p^64s^2$	^{1}S	0	$3p^64s$ 4p	^{1}P°	1	422.67	7.4e−17	422.68	1.2e−01	422.67	1.4e−16	422.68	9.1e−19	423.32	3.0e−18
	Fe I	$3d^6(^5D)$ 4s 4p (^{3}P°)	z ^{5}F°	5	$3d^6(^5D)$ 4s (^{6}D) 4d	e ^{5}G	6	422.74	8.8e−21	422.74	3.2e−02						

Table A.1. continued.

Label	Specie	Energy transitions								Peaks (experiment)		Peaks (simulation)					
		Lower energy level			Upper energy level			4000 K		High resolution		4000 K		7000 K		10 000 K	
		El. conf.	Term	J	El. conf.	Term	J	λ (nm)	I_{em}	λ (nm)	I_{em}	λ (nm)	I_{em}	λ (nm)	I_{em}	λ (nm)	I_{em}
	Fe II	$3d^6(^3P2)\ 4s$	b ^4P	5/2	$3d^6(^5D)\ 4p$	z $^4D°$	7/2	423.32	8.9e−24	423.36	1.5e−02			423.32	6.3e−19		
	Fe I	$3d^6(^5D)\ 4s\ 4p\ (^3P°)$	z $^7D°$	1	$3d^6(^5D)\ 4s\ (^6D)\ 5s$	e ^7D	2	423.36	1.4e−20								
	Fe I	$3d^6(^5D)\ 4s\ 4p\ (^3P°)$	z $^7D°$	4	$3d^6(^5D)\ 4s\ (^6D)\ 5s$	e ^7D	4	423.59	3.1e−20	423.60	2.5e−02						
	Fe I	$3d^6(^5D)\ 4s\ 4p\ (^3P°)$	z $^7D°$	2	$3d^6(^5D)\ 4s\ (^6D)\ 5s$	e ^7D	3	425.01	2.4e−20	425.02	2.5e−02						
	Fe I	$3d^7(^4F)\ 4s$	a ^3F	3	$3d^7(^4F)\ 4p$	z $^3G°$	3	425.08	1.6e−19	425.09	3.0e−02						
	Cr I	$3d^5(^6S)\ 4s$	a ^7S	3	$3d^5(^6S)\ 4p$	z $^7P°$	4	425.43	2.4e−18	425.43	2.0e−02						
	Fe I	$3d^6(^5D)\ 4s\ 4p\ (^3P°)$	z $^7D°$	5	$3d^6(^5D)\ 4s\ (^6D)\ 5s$	e ^7D	5	426.05	8.9e−20	426.06	5.6e−02						
	Fe I	$3d^6(^5D)\ 4s\ 4p\ (^3P°)$	z $^7D°$	3	$3d^6(^5D)\ 4s\ (^6D)\ 5s$	e ^7D	4	427.12	2.9e−20	427.12	2.9e−02			427.19	3.4e−19		
	Fe I	$3d^7(^4F)\ 4s$	a ^3F	4	$3d^7(^4F)\ 4p$	z $^3G°$	5	427.18	7.4e−19	427.18	8.5e−02						
	Fe II	$3d^6(^3P2)\ 4s$	b ^4P	3/2	$3d^6(^5D)\ 4p$	z $^4D°$	1/2	427.33	2.1e−25								
	Cr I	$3d^5(^6S)\ 4s$	a ^7S	3	$3d^5(^6S)\ 4p$	z $^7P°$	3	427.48	1.9e−18	427.49	2.0e−02						
	Fe I	$3d^7(^4P)\ 4s$	a ^5P	3	$3d^6(^3P2)\ 4s\ 4p\ (^3P°)$	z $^5S°$	2	428.24	2.4e−20								
	Cr I	$3d^5(^6S)\ 4s$	a ^7S	3	$3d^5(^6S)\ 4p$	z $^7P°$	2	428.97	1.4e−18	428.97	1.6e−02			430.78	3.2e−19		
	Fe I	$3d^7(^4F)\ 4s$	a ^3F	4	$3d^7(^4F)\ 4p$	z $^5G°$	4	429.41	8.6e−20								
	Fe II	$3d^6(^3P2)\ 4s$	b ^4P	3/2	$3d^6(^5D)\ 4p$	z $^4F°$	5/2	429.66	5.1e−25								
	Fe I	$3d^6(^5D)\ 4s\ 4p\ (^3P°)$	z $^7D°$	4	$3d^6(^5D)\ 4s\ (^6D)\ 5s$	e ^7D	5	429.92	2.9e−20	429.93	2.2e−02					430.32	4.1e−19
	Ca I	$3p^6 4s\ 4p$	$^3P°$	2	$3p^6 4p^2$	^3P	2	430.25	3.6e−19	430.22	3.7e−02						
	Fe II	$3d^6(^3P2)\ 4s$	b ^4P	3/2	$3d^6(^5D)\ 4p$	z $^4D°$	3/2	430.32	1.1e−24								
	Fe I	$3d^7(^4F)\ 4s$	a ^3F	3	$3d^7(^4F)\ 4p$	z $^3G°$	4	430.79	7.7e−19	430.79	8.7e−02						
	Fe I	$3d^7(^4F)\ 4s$	a ^3F	2	$3d^7(^4F)\ 4p$	z $^3G°$	3	432.58	8.2e−19	432.58	1.1e−01			432.58	3.5e−19		
F7	Fe I	$3d^7(^4F)\ 4s$	a ^3F	4	$3d^7(^4F)\ 4p$	z $^5G°$	5	438.35	2.0e−18	438.36	1.1e−01	438.35	3.8e−18	438.37	7.4e−19	438.52	5.1e−19
	Mg II	$2p^6 4p$	$^2P°$	1/2	$2p^6 5d$	^2D	3/2	438.46	3.9e−30								
	Fe II	$3d^6(^3P2)\ 4s$	b ^4P	1/2	$3d^6(^5D)\ 4p$	z $^4D°$	1/2	438.54	1.0e−24								
	Mg II	$2p^6 4p$	$^2P°$	3/2	$2p^6 5d$	^2D	5/2	439.06	7.0e−30								
	Fe I	$3d^7(^4F)\ 4s$	a ^3F	3	$3d^7(^4F)\ 4p$	z $^5G°$	4	440.47	7.4e−19	440.50	7.0e−02	440.47	1.4e−18	440.47	2.8e−19		
F8	Ca I	$3p^6 4s\ 4p$	$^3P°$	0	$3p^6 4s\ 4d$	^3D	1	442.54	1.0e−19	442.55	2.3e−02	442.62	3.1e−19				
	Fe I	$3d^6 4s^2$	a ^5D	3	$3d^6(^5D)\ 4s\ 4p\ (^3P°)$	z $^7F°$	4	442.73	7.5e−20	442.73	1.4e−02						
	Ca I	$3p^6 4s\ 4p$	$^3P°$	1	$3p^6 4s\ 4d$	^3D	2	443.50	2.3e−19	443.49	3.5e−02	443.51	5.7e−19				
	Ca I	$3p^6 4s\ 4p$	$^3P°$	1	$3p^6 4s\ 4d$	^3D	1	443.57	7.0e−20	443.56	2.4e−02						
	Fe I	$3d^7(^4P)\ 4s$	a ^5P	2	$3d^6(^5D)\ 4s\ 4p\ (^1P°)$	x $^5D°$	2	444.23	9.3e−21	444.24	1.6e−02						
	Ca I	$3p^6 4s\ 4p$	$^3P°$	2	$3p^6 4s\ 4d$	^3D	3	445.48	4.1e−19	445.47	4.6e−02	445.49	9.2e−19				
	Ca I	$3p^6 4s\ 4p$	$^3P°$	2	$3p^6 4s\ 4d$	^3D	2	445.59	6.7e−20	445.60	2.5e−02						
	Fe I	$3d^7(^4P)\ 4s$	a ^5P	3	$3d^6(^5D)\ 4s\ 4p\ (^1P°)$	x $^5D°$	3	445.91	9.5e−21	445.92	1.9e−02						
	Fe I	$3d^6 4s^2$	a ^5D	2	$3d^6(^5D)\ 4s\ 4p\ (^3P°)$	z $^7F°$	3	446.17	4.8e−20								
	Fe I	$3d^7(^4P)\ 4s$	b ^3P	2	$3d^6(^3P2)\ 4s\ 4p\ (^3P°)$	x $^3D°$	3	446.66	6.9e−21	446.66	2.2e−02					448.12	2.1e−17
	Fe II	$3d^6(^3F2)\ 4s$	b ^4F	5/2	$3d^6(^5D)\ 4p$	z $^4F°$	3/2	447.29	1.1e−25					448.12	4.8e−19		
	Fe I	$3d^7(^4P)\ 4s$	b ^3P	1	$3d^6(^3P2)\ 4s\ 4p\ (^3P°)$	x $^3D°$	2	447.60	4.0e−21	447.61	2.1e−02						
	Mg II	$2p^6 3d$	^2D	5/2	$2p^6 4f$	$^2F°$	7/2	448.11	3.9e−27	448.12	5.2e−02						
	Mg II	$2p^6 3d$	^2D	5/2	$2p^6 4f$	$^2F°$	5/2	448.12	2.0e−28								
	Mg II	$2p^6 3d$	^2D	3/2	$2p^6 4f$	$^2F°$	5/2	448.13	2.7e−27								

Table A.1. continued.

Label	Specie	Energy transitions								Peaks (experiment)		Peaks (simulation)					
		Lower energy level			Upper energy level			4000 K		High resolution		4000 K		7000 K		10 000 K	
		El. conf.	Term	J	El. conf.	Term	J	λ (nm)	I_{em}	λ (nm)	I_{em}	λ (nm)	I_{em}	λ (nm)	I_{em}	λ (nm)	I_{em}
F9	Fe II	$3d^6(^3F2)\ 4s$	b ^4F	9/2	$3d^6(^5D)\ 4p$	z $^4F°$	7/2	452.02	1.0e−24			452.87	7.9e−20	452.23	3.2e−19	452.23	1.7e−18
	Fe II	$3d^6(^3F2)\ 4s$	b ^4F	5/2	$3d^6(^5D)\ 4p$	z $^4D°$	3/2	452.26	3.9e−24								
	Ca I	$3p^6 3d\ 4s$	^1D	2	$3p^6 4s\ np$	w $^1P°$	1	452.69	8.8e−21	452.72	1.2e−02						
	Fe I	$3d^7(^4P)\ 4s$	a ^5P	3	$3d^6(^5D)\ 4s\ 4p\ (^1P°)$	x $^5D°$	4	452.86	3.0e−20	452.86	1.8e−02						
	Fe I	$3d^7(^4F)\ 4s$	a ^3F	4	$3d^7(^4F)\ 4p$	y $^5F°$	4	453.11	1.0e−20								
	Fe II	$3d^6(^3F2)\ 4s$	b ^4F	3/2	$3d^6(^5D)\ 4p$	z $^4D°$	3/2	454.15	4.2e−25								
F10	Fe I	$3d^6(^5D)\ 4s\ 4p\ (^3P°)$	z $^7D°$	2	$3d^8$	^3P	1	470.10	8.4e−22			470.28	1.2e−20	470.30	3.9e−20	470.30	2.2e−21
	Mg I	$3s\ 3p$	$^1P°$	1	$3s\ 5d$	^1D	2	470.30	5.6e−21	470.31	2.4e−02						
F11	Fe I	$3d^6(^5D)\ 4s\ 4p\ (^3P°)$	z $^7F°$	3	$3d^6(^5D)\ 4s\ (^6D)\ 5s$	e ^7D	2	487.13	1.6e−20	487.14	2.9e−03	487.16	5.0e−20	487.16	3.5e−20		
	Fe I	$3d^6(^5D)\ 4s\ 4p\ (^3P°)$	z $^7F°$	1	$3d^6(^5D)\ 4s\ (^6D)\ 5s$	e ^7D	1	487.21	9.6e−21	487.22	2.7e−03						
	Ca I	$3p^6 3d\ 4s$	^1D	2	$3p^6 4s\ 4f$	$^1F°$	3	487.81	1.6e−20	487.83	2.2e−03	487.80	3.1e−20				
	Fe I	$3d^6(^5D)\ 4s\ 4p\ (^3P°)$	z $^7F°$	2	$3d^6(^5D)\ 4s\ (^6D)\ 5s$	e ^7D	2	489.08	1.5e−20	489.09	3.0e−03	489.13	8.8e−20	489.12	6.0e−20		
	Fe I	$3d^6(^5D)\ 4s\ 4p\ (^3P°)$	z $^7F°$	4	$3d^6(^5D)\ 4s\ (^6D)\ 5s$	e ^7D	3	489.15	3.1e−20	489.16	5.0e−03						
	Fe I	$3d^6(^5D)\ 4s\ 4p\ (^3P°)$	z $^7F°$	3	$3d^6(^5D)\ 4s\ (^6D)\ 5s$	e ^7D	3	491.90	1.8e−20	491.91	3.0e−03	492.01	1.3e−19	492.39	1.8e−18	492.39	8.5e−18
	Fe I	$3d^6(^5D)\ 4s\ 4p\ (^3P°)$	z $^7F°$	5	$3d^6(^5D)\ 4s\ (^6D)\ 5s$	e ^7D	4	492.05	5.0e−20	492.07	6.8e−03						
	Fe II	$3d^5 4s^2$	a ^6S	5/2	$3d^6(^5D)\ 4p$	z $^6P°$	3/2	492.39	3.1e−23								
	Fe I	$3d^6(^5D)\ 4s\ 4p\ (^3P°)$	z $^7F°$	4	$3d^6(^5D)\ 4s\ (^6D)\ 5s$	e ^7D	4	495.73	1.6e−20	495.78	8.0e−03	495.75	1.9e−19	495.75	1.2e−19		
	Fe I	$3d^6(^5D)\ 4s\ 4p\ (^3P°)$	z $^7F°$	6	$3d^6(^5D)\ 4s\ (^6D)\ 5s$	e ^7D	5	495.76	8.1e−20								
F12	Fe I	$3d^7(^4F)\ 4s$	a ^5F	5	$3d^6(^5D)\ 4s\ 4p\ (^3P°)$	z $^5F°$	5	501.21	3.2e−20	501.22	7.7e−03	501.21	6.3e−20	501.84	1.3e−18	501.84	6.2e−18
	Fe II	$3d^5 4s^2$	a ^6S	5/2	$3d^6(^5D)\ 4p$	z $^6P°$	5/2	501.84	2.4e−23	501.84	1.2e−02						
F13	Fe I	$3d^7(^2H)\ 4s$	a ^1H	5	$3d^7(^2G)\ 4p$	z $^1H°$	5	511.04	2.5e−22	511.03	1.2e+02	511.04	6.4e−20	511.04	1.8e−21	511.27	9.9e−21
	Fe I	$3d^6 4s^2$	a ^5D	4	$3d^6(^5D)\ 4s\ 4p\ (^3P°)$	z $^7D°$	4	511.04	3.2e−20								
	Fe II	$3d^6(^5D)\ 4d$	^6P	5/2	$3d^6(^5D_1)\ 4f$	$^2[4]°$	7/2	511.22	2.7e−32	511.21	2.2e+01						
	Fe II	$3d^6(^5D)\ 4d$	^6D	5/2	$3d^6(^5D_3)\ 4f$	$^2[3]°$	5/2	511.30	6.0e−32	511.30	3.4e+01						
F14	Mg I	$3s\ 3p$	$^3P°$	0	$3s\ 4s$	^3S	1	516.73	3.6e−19	516.75	1.0e−01	517.26	2.1e−18	516.91	4.4e−18	516.90	1.8e−17
	Fe I	$3d^7(^4F)\ 4s$	a ^3F	4	$3d^6(^5D)\ 4s\ 4p\ (^3P°)$	z $^3D°$	3	516.75	2.0e−19								
	Fe II	$3d^5 4s^2$	a ^6S	5/2	$3d^6(^5D)\ 4p$	z $^6P°$	7/2	516.90	8.1e−23	516.90	4.3e−02						
	Mg I	$3s\ 3p$	$^3P°$	1	$3s\ 4s$	^3S	1	517.27	1.1e−18	517.28	1.2e−01						
	Mg I	$3s\ 3p$	$^3P°$	2	$3s\ 4s$	^3S	1	518.36	1.8e−18	518.36	1.6e−01	518.36	3.5e−18	518.36	1.2e−18		
	Cr I	$3d^5(^6S)\ 4s$	a ^5S	2	$3d^5(^6S)\ 4p$	z $^5P°$	1	520.45	3.3e−19	520.46	3.7e−02	520.70	2.4e−18				
	Cr I	$3d^5(^6S)\ 4s$	a ^5S	2	$3d^5(^6S)\ 4p$	z $^5P°$	2	520.60	5.5e−19	520.61	4.2e−02						
	Cr I	$3d^5(^6S)\ 4s$	a ^5S	2	$3d^5(^6S)\ 4p$	z $^5P°$	3	520.84	7.6e−19	520.85	5.1e−02						
F15	Fe II	$3d^6(^5D)\ 4d$	f ^4D	7/2	$3d^6(^5D_2)\ 4f$	$^2[2]°$	5/2	526.84	1.8e−32			526.97	1.9e−18	526.98	1.0e−19	526.99	1.7e−20
	Fe I	$3d^7(^4F)\ 4s$	a ^5F	5	$3d^6(^5D)\ 4s\ 4p\ (^3P°)$	z $^5D°$	4	526.95	8.3e−19	526.96	8.8e−03						
	Fe II	$3d^6(^5D)\ 4d$	e ^6G	7/2	$3d^6(^5D_2)\ 4f$	$^2[5]°$	9/2	527.00	1.0e−31								
	Ca I	$3p^6 3d\ 4s$	^3D	3	$3p^6 3d\ 4p$	$^3P°$	2	527.03	8.0e−20	527.04	3.7e−03						
	Fe I	$3d^7(^4F)\ 4s$	a ^3F	2	$3d^6(^5D)\ 4s\ 4p\ (^3P°)$	z $^3D°$	1	527.04	9.1e−20								
	Fe II	$3d^6(^5D)\ 4d$	e ^6G	7/2	$3d^6(^5D_2)\ 4f$	$^2[3]°$	7/2	527.11	1.2e−32								
F16	Fe I	$3d^7(^4F)\ 4s$	a ^5F	4	$3d^6(^5D)\ 4s\ 4p\ (^3P°)$	z $^5D°$	3	532.80	5.3e−19	532.81	5.5e−03	532.81	1.1e−18	532.82	5.9e−20	533.00	1.0e−19
	Fe I	$3d^7(^4F)\ 4s$	a ^3F	3	$3d^6(^5D)\ 4s\ 4p\ (^3P°)$	z $^3D°$	3	532.85	3.4e−20								
	N I	$2s\ 2p^4$	^4P	5/2	$2s^2 2p^2(^3P)\ 4p$	$^4D°$	7/2	532.86	1.5e−29								
	O I	$2s^2 2p^3(^4S°)\ 3p$	^5P	1	$2s^2 2p^3(^4S°)\ 5d$	$^5D°$	0	532.91	9.5e−30								
	O I	$2s^2 2p^3(^4S°)\ 3p$	^5P	1	$2s^2 2p^3(^4S°)\ 5d$	$^5D°$	1	532.91	2.1e−29								

Table A.1. continued.

Label	Specie	Energy transitions								Peaks (experiment)		Peaks (simulation)					
		Lower energy level			Upper energy level			4000 K		High resolution		4000 K		7000 K		10 000 K	
		El. conf.	Term	J	El. conf.	Term	J	λ (nm)	I_{em}	λ (nm)	I_{em}	λ (nm)	I_{em}	λ (nm)	I_{em}	λ (nm)	I_{em}
	O I	$2s^22p^3(^4S°)$ 3p	^{5}P	1	$2s^22p^3(^4S°)$ 5d	^{5}D°	2	532.91	1.7e−29								
	O I	$2s^22p^3(^4S°)$ 3p	^{5}P	2	$2s^22p^3(^4S°)$ 5d	^{5}D°	2	532.97	2.8e−29								
	O I	$2s^22p^3(^4S°)$ 3p	^{5}P	2	$2s^22p^3(^4S°)$ 5d	^{5}D°	3	532.97	4.4e−29								
	O I	$2s^22p^3(^4S°)$ 3p	^{5}P	3	$2s^22p^3(^4S°)$ 5d	^{5}D°	3	533.07	2.2e−29	533.09	1.5e−03						
	O I	$2s^22p^3(^4S°)$ 3p	^{5}P	3	$2s^22p^3(^4S°)$ 5d	^{5}D°	4	533.07	8.5e−29								
F17	Fe I	$3d^7(^4F)$ 4p	z ^{5}G°	4	$3d^7(^4F)$ 4d	e ^{5}H	5	537.00	2.4e−21	537.02	1.1e−02	537.15	6.3e−19	537.10	4.3e−20	537.58	9.9e−21
	Fe I	$3d^7(^4F)$ 4s	a ^{5}F	3	$3d^6(^5D)$ 4s 4p (^{3}P°)	z ^{5}D°	2	537.15	3.2e−19	537.17	2.7e−02						
	Fe II	$3d^6(^5D)$ 4d	e ^{6}G	11/2	$3d^6(^5D_4)$ 4f	^{2}[6]°	11/2	537.58	9.8e−32	537.58	4.2e−03						
	Fe I	$3d^7(^4F)$ 4p	z ^{5}G°	5	$3d^7(^4F)$ 4d	e ^{5}H	6	538.34	3.7e−21	538.35	7.4e−03			538.34	2.3e−20	538.70	6.1e−20
	Fe II	$3d^6(^5D)$ 4d	e ^{4}G	11/2	$3d^6(^5D_3)$ 4f	^{2}[6]°	13/2	538.71	5.4e−31								
	Fe I	$3d^6(^5D)$ 4s 4p (^{3}P°)	z ^{5}D°	3	$3d^6(^5D)$ 4s (^{6}D) 5s	e ^{5}D	4	539.32	3.6e−21			539.71	3.2e−19	539.68	1.6e−20	539.55	4.2e−20
	Fe II	$3d^6(^5D)$ 4d	e ^{6}G	11/2	$3d^6(^5D_4)$ 4f	^{2}[5]°	11/2	539.38	1.2e−31								
	Fe II	$3d^6(^5D)$ 4d	^{6}S	5/2	$3d^6(^5D_0)$ 4f	^{2}[3]°	7/2	539.59	2.6e−31								
	Fe I	$3d^7(^4F)$ 4s	a ^{5}F	4	$3d^6(^5D)$ 4s 4p (^{3}P°)	z ^{5}D°	4	539.71	1.6e−19	539.74	1.5e−02						
	Fe II	$3d^6(^5D)$ 4d	e ^{4}G	9/2	$3d^6(^5D_2)$ 4f	^{2}[5]°	11/2	540.21	4.5e−31			540.61	4.0e−19	540.52	3.0e−20	540.23	5.9e−20
	Fe I	$3d^7(^4F)$ 4p	z ^{3}G°	4	$3d^7(^4F)$ 4d	e ^{3}H	5	540.42	2.0e−21	540.44	9.8e−03						
	Fe II	$3d^6(^5D)$ 4d	f ^{4}D	1/2	$3d^6(^5D_2)$ 4f	^{2}[1]°	3/2	540.51	5.7e−32								
	Fe II	$3d^6(^5D)$ 4d	f ^{4}D	5/2	$3d^6(^5D_3)$ 4f	^{2}[3]°	*v*52	540.57	6.2e−32	540.58	1.6e−02						
	Fe I	$3d^7(^4F)$ 4s	a ^{5}F	2	$3d^6(^5D)$ 4s 4p (^{3}P°)	z ^{5}D°	1	540.58	1.9e−19								
	Cr I	$3d^44s^2$	a ^{5}D	4	$3d^5(^6S)$ 4p	z ^{5}P°	3	540.98	9.0e−20					541.46	2.7e−20	541.38	4.8e−20
	Fe I	$3d^7(^4F)$ 4p	z ^{3}G°	3	$3d^7(^4F)$ 4d	e ^{3}H	4	541.09	1.3e−21	541.08	7.7e−03						
	Fe II	$3d^6(^5D)$ 4d	^{6}S	5/2	$3d^6(^5D_1)$ 4f	^{2}[3]°	7/2	541.14	1.2e−31	541.12	9.3e−03						
	Fe II	$3d^6(^3G)$ 4s	a ^{4}G	7/2	$3d^6(^5D)$ 4p	z ^{4}D°	7/2	541.41	9.0e−26								
	Fe II	$3d^6(^5D)$ 4d	e ^{4}G	11/2	$3d^6(^5D_3)$ 4f	^{2}[5]°	11/2	541.49	8.2e−32								
	Fe I	$3d^7(^4F)$ 4p	z ^{3}G°	5	$3d^7(^4F)$ 4d	e ^{3}H	6	541.52	3.0e−21								
	Cr II	$3d^4$(a ^{3}P) 4s	b ^{4}P	3/2	$3d^4(^5D)$ 4p	z ^{4}P°	1/2	542.09	2.8e−25					542.95	2.0e−20	542.83	8.5e−20
	Fe II	$3d^6(^3G)$ 4s	a ^{4}G	9/2	$3d^6(^5D)$ 4p	z ^{4}F°	9/2	542.52	1.2e−25			542.99	3.9e−19				
	Fe II	$3d^54s^2$	b ^{4}G	11/2	$3d^6(^3D)$ 4p	w ^{4}F°	9/2	542.78	2.8e−28								
	Fe I	$3d^7(^4F)$ 4s	a ^{5}F	3	$3d^6(^5D)$ 4s 4p (^{3}P°)	z ^{5}D°	3	542.97	1.9e−19	542.98	2.9e−02						
	Fe II	$3d^6(^5D)$ 4d	e ^{4}G	7/2	$3d^6(^5D_1)$ 4f	^{2}[4]°	9/2	543.00	3.7e−31								
	Fe I	$3d^7(^4F)$ 4s	a ^{5}F	1	$3d^6(^5D)$ 4s 4p (^{3}P°)	z ^{5}D°	0	543.45	9.4e−20	543.45	1.4e−02					543.60	3.0e−20
	O I	$2s^22p^3(^4S°)$ 3p	^{5}P	1	$2s^22p^3(^4S°)$ 6s	^{5}S°	2	543.52	1.5e−29								
	O I	$2s^22p^3(^4S°)$ 3p	^{5}P	2	$2s^22p^3(^4S°)$ 6s	^{5}S°	2	543.58	2.5e−29								
	O I	$2s^22p^3(^4S°)$ 3p	^{5}P	3	$2s^22p^3(^4S°)$ 6s	^{5}S°	2	543.69	3.5e−29								
	Fe II	$3d^6(^5D)$ 4d	f ^{4}D	3/2	$3d^6(^5D_3)$ 4f	^{2}[1]°	3/2	544.24	7.9e−32			544.69	3.2e−19	544.69	1.6e−20	544.48	2.9e−20
	Fe II	$3d^6(^5D)$ 4d	^{6}S	5/2	$3d^6(^5D_1)$ 4f	^{2}[2]°	5/2	544.44	9.5e−32								
	Fe II	$3d^6(^5D)$ 4d	f ^{4}D	3/2	$3d^6(^5D_3)$ 4f	^{2}[2]°	5/2	544.58	1.3e−31								
	Fe I	$3d^7(^4F)$ 4s	a ^{5}F	2	$3d^6(^5D)$ 4s 4p (^{3}P°)	z ^{5}D°	2	544.69	1.6e−19	544.70	2.2e−02						
	Fe II	$3d^6(^5D)$ 4d	e ^{4}G	5/2	$3d^6(^5D_0)$ 4f	^{2}[3]°	7/2	545.01	1.1e−31								
	Fe I	$3d^7(^4F)$ 4s	a ^{5}F	1	$3d^6(^5D)$ 4s 4p (^{3}P°)	z ^{5}D°	1	545.56	1.0e−19	545.58	1.9e−02	545.56	2.0e−19	545.56	1.0e−20		
	Fe II	$3d^6(^5D)$ 4d	e ^{6}G	9/2	$3d^6(^5D_4)$ 4f	^{2}[5]°	9/2	545.59	6.2e−32								
F18	Fe II	$3d^6(^3H)$ 4s	b ^{2}H	9/2	$3d^6(^5D)$ 4p	z ^{4}D°	7/2	552.51	3.0e−26			552.84	1.8e−20	552.84	4.1e−20	552.96	4.0e−20
	Mg I	3s 3p	^{1}P°	1	3s 4d	^{1}D	2	552.84	9.4e−21	552.84	5.7e−03						
	Fe II	$3d^6(^5D)$ 4d	f ^{4}D	5/2	$3d^6(^5D_4)$ 4f	^{2}[3]°	5/2	552.91	1.0e−31								

Table A.1. continued.

Label	Specie	Energy transitions							Peaks (experiment)		Peaks (simulation)					
		Lower energy level			Upper energy level			4000 K	High resolution		4000 K		7000 K		10 000 K	
		El. conf.	Term	J	El. conf.	Term	J	λ (nm)	I_{em}	λ (nm)	I_{em}	λ (nm)	I_{em}	λ (nm)	I_{em}	λ (nm)	I_{em}
	Fe II	$3d^5 4s^2$	b ^{4}G	9/2	$3d^6(^3D)$ 4p	w ^{4}F°	7/2	552.99	1.7e−28	552.98	2.1e−03						
	Fe II	$3d^6(^5D)$ 4d	f ^{4}D	3/2	$3d^6(^5D_4)$ 4f	^{2}[1]°	1/2	553.03	3.9e−32								
F19	N I	$2s^2 2p^2(^3P)$ 3p	^{4}D°	5/2	$2s^2 2p^2(^3P)$ 5d	^{4}F	5/2	557.59	2.1e−30			558.89	3.5e−19	558.78	3.3e−20	557.84	2.4e−20
	Fe II	$3d^6(^5D)$ 4d	e ^{4}G	7/2	$3d^6(^5D_3)$ 4f	^{2}[3]°	7/2	557.79	1.2e−31								
	Fe II	$3d^6(^5D)$ 4d	^{6}S	5/2	$3d^6(^5D_3)$ 4f	^{2}[1]°	3/2	557.80	3.6e−32								
	Fe II	$3d^6(^5D)$ 4d	^{4}S	3/2	$3d^6(^5D_2)$ 4f	^{2}[2]°	3/2	557.99	4.4e−32								
	Fe II	$3d^6(^5D)$ 4d	^{6}S	5/2	$3d^6(^5D_3)$ 4f	^{2}[2]°	5/2	558.16	4.6e−32								
	Ca I	$3p^6$3d 4s	^{3}D	2	$3p^6$3d 4p	^{3}D°	3	558.20	1.9e−20	558.21	1.9e−03						
	Fe II	$3d^6(^5D)$ 4d	f ^{4}D	3/2	$3d^6(^5D_4)$ 4f	^{2}[3]°	5/2	558.39	2.7e−32							558.77	4.4e−20
	Fe I	$3d^6(^5D)$ 4s 4p (^{3}P°)	z ^{5}F°	4	$3d^6(^5D)$ 4s (^{6}D) 5s	e ^{5}D	3	558.68	1.1e−20	558.69	1.6e−03						
	Fe II	$3d^5 4s^2$	b ^{4}G	5/2	$3d^6(^3D)$ 4p	w ^{4}F°	3/2	558.71	1.2e−28								
	Fe II	$3d^6(^5D)$ 4d	^{6}S	5/2	$3d^6(^5D_3)$ 4f	^{2}[3]°	7/2	558.80	2.8e−32								
	Fe II	$3d^6(^5D)$ 4d	e ^{4}G	7/2	$3d^6(^5D_3)$ 4f	^{2}[5]°	9/2	558.82	2.3e−31								
	Ca I	$3p^6$3d 4s	^{3}D	3	$3p^6$3d 4p	^{3}D°	3	558.87	1.5e−19	558.89	8.1e−03						
	Ca I	$3p^6$3d 4s	^{3}D	1	$3p^6$3d 4p	^{3}D°	2	559.01	1.9e−20	559.02	3.0e−03						
	Ca I	$3p^6$3d 4s	^{3}D	2	$3p^6$3d 4p	^{3}D°	2	559.45	8.6e−20	559.47	5.1e−03	559.47	2.0e−19	559.47	1.1e−20		
	Ca I	$3p^6$3d 4s	^{3}D	1	$3p^6$3d 4p	^{3}D°	1	559.85	5.9e−20	559.87	3.8e−03						
	Ca I	$3p^6$3d 4s	^{3}D	3	$3p^6$3d 4p	^{3}D°	2	560.13	1.9e−20	560.15	2.0e−03						
	Ca I	$3p^6$3d 4s	^{3}D	2	$3p^6$3d 4p	^{3}D°	1	560.28	1.9e−20	560.30	2.5e−03						
	Fe I	$3d^6(^5D)$ 4s 4p (^{3}P°)	z ^{5}F°	1	$3d^6(^5D)$ 4s (^{6}D) 5s	e ^{5}D	1	560.29	1.8e−21								
	Fe I	$3d^6(^5D)$ 4s 4p (^{3}P°)	z ^{5}F°	5	$3d^6(^5D)$ 4s (^{6}D) 5s	e ^{5}D	4	561.56	1.9e−20	561.58	1.8e−03	561.56	3.7e−20	561.56	3.0e−20	561.56	1.8e−21
F20	Na I	$2p^6$3s	^{2}S	1/2	$2p^6$3p	^{2}P°	3/2	589.00	2.0e−17	589.01	4.7e−02	589.00	4.0e−17	589.00	4.2e−19	589.00	5.4e−20
	Na I	$2p^6$3s	^{2}S	1/2	$2p^6$3p	^{2}P°	1/2	589.59	1.0e−17	589.61	3.1e−02	589.57	2.1e−17	589.57	2.1e−19	589.57	2.8e−20
F21	Fe II	$3d^6(^3D)$ 4s	b ^{4}D	3/2	$3d^6(^5D)$ 4p	z ^{4}P°	3/2	623.84	1.2e−25			624.63	2.8e−21	623.84	1.2e−20	623.91	1.5e−19
	Si II	$3s^2$4f	^{2}F°	7/2	$3s^2$6g	^{2}G	9/2	623.96	9.7e−34								
	Si II	$3s^2$4f	^{2}F°	5/2	$3s^2$6g	^{2}G	7/2	623.97	6.8e−34								
	Fe I	$3d^7(^4P)$ 4s	a ^{5}P	1	$3d^6(^5D)$ 4s 4p (^{3}P°)	z ^{3}P°	2	624.06	3.9e−22								
	Fe I	$3d^6(^5D)$ 4s 4p (^{3}P°)	z ^{5}P°	3	$3d^6(^5D)$ 4s (^{6}D) 5s	e ^{5}D	3	624.63	1.4e−21					624.75	2.6e−20	624.76	1.5e−19
	Fe II	$3d^6(^3D)$ 4s	b ^{4}D	5/2	$3d^6(^5D)$ 4p	z ^{4}P°	3/2	624.76	2.3e−25								
F22	Si II	$3s^2$4s	^{2}S	1/2	$3s^2$4p	^{2}P°	3/2	634.71	8.4e−28	634.72	6.5e−03	635.82	2.4e−21	634.71	1.1e−19	634.71	1.1e−17
	Fe I	$3d^7(^4P)$ 4s	b ^{3}P	1	$3d^7(^4F)$ 4p	y ^{3}D°	2	635.50	5.1e−22								
	Fe I	$3d^7(^4F)$ 4s	a ^{5}F	5	$3d^6(^5D)$ 4s 4p (^{3}P°)	z ^{7}F°	6	635.87	1.1e−21								
	Si II	$3s^2$4s	^{2}S	1/2	$3s^2$4p	^{2}P°	1/2	637.14	5.0e−28	637.14	2.9e−03			637.14	6.4e−20	637.14	6.3e−18
F23	O I	$2s^2 2p^3(^4S°)$ 3p	^{5}P	2	$2s^2 2p^3(^4S°)$ 5s	^{5}S°	2	645.44	1.3e−28			646.26	9.7e−19	645.64	4.4e−20	645.62	3.0e−19
	O I	$2s^2 2p^3(^4S°)$ 3p	^{5}P	3	$2s^2 2p^3(^4S°)$ 5s	^{5}S°	2	645.60	1.8e−28								
	Fe II	$3d^6(^3D)$ 4s	b ^{4}D	7/2	$3d^6(^5D)$ 4p	z ^{4}P°	5/2	645.64	4.2e−25								
	Ca I	$3p^6$3d 4s	^{3}D	2	$3p^6$3d 4p	^{3}F°	3	646.26	3.1e−19	646.27	6.1e−03			646.25	3.4e−20		
	Fe I	$3d^7(^4F)$ 4s	a ^{5}F	4	$3d^6(^5D)$ 4s 4p (^{3}P°)	z ^{7}F°	5	646.27	1.9e−19								
	Ca I	$3p^6$3d 4s	^{3}D	3	$3p^6$3d 4p	^{3}F°	3	647.17	3.8e−20	647.18	1.5e−03	647.17	7.5e−20	647.17	3.0e−21	648.33	1.9e−19
	Fe II	$3d^6(^3F1)$ 4s	c ^{4}F	9/2	$3d^6(^3G)$ 4p	x ^{4}G°	11/2	648.22	1.1e−27					648.33	1.1e−20		
	N I	$2s^2 2p^2(^3P)$ 3p	^{4}D°	7/2	$2s^2 2p^2(^3P)$ 4d	^{4}F	9/2	648.27	1.1e−28			649.39	4.5e−19				

Table A.1. continued.

Label	Specie	Energy transitions								Peaks (experiment)		Peaks (simulation)					
		Lower energy level			Upper energy level			4000 K		High resolution		4000 K		7000 K		10 000 K	
		El. conf.	Term	J	El. conf.	Term	J	λ (nm)	I_{em}	λ (nm)	I_{em}	λ (nm)	I_{em}	λ (nm)	I_{em}	λ (nm)	I_{em}
	N I	$2s^2 2p^2 (^3P)$ 3p	$^4D°$	3/2	$2s^2 2p^2 (^3P)$ 4d	^4F	5/2	648.38	4.9e−29								
	N I	$2s^2 2p^2 (^3P)$ 3p	$^4D°$	5/2	$2s^2 2p^2 (^3P)$ 4d	^4F	7/2	648.48	7.3e−29								
	Ca I	$3p^6$ 3d 4s	^3D	1	$3p^6$ 3d 4p	$^3F°$	2	649.38	2.1e−19	649.39	3.6e−03			649.41	2.2e−20		
	Fe I	$3d^6 4s^2$	a ^3H	6	$3d^7 (^4F)$ 4p	z $^5G°$	5	649.50	2.0e−20	649.50	1.5e−03						
F24	H I	2p	$^2P°$	1/2	3d	^2D	3/2	656.27	9.2e−27	656.25	1.6e−02	656.28	7.0e−26	656.28	2.3e−19	656.28	2.8e−18
	H I	2s	^2S	1/2	3p	$^2P°$	3/2	656.27	3.8e−27								
	H I	2s	^2S	1/2	3p	$^2P°$	1/2	656.28	1.9e−27								
	H I	2p	$^2P°$	3/2	3d	^2D	5/2	656.29	1.7e−26								
	H I	2p	$^2P°$	3/2	3d	^2D	3/2	656.29	1.8e−27								
	H I	2p	$^2P°$	3/2	3d	^2D	5/2	656.29	2.8e−27								
F25	Fe II	$3d^6 (^5D)$ 5p	$^4D°$	5/2	$3d^6 (^5D)$ 5d	^4G	7/2	675.00	9.6e−33			675.02	1.9e−21	675.14	6.1e−22	675.10	6.9e−21
	Fe I	$3d^6 4s^2$	a $^3P2$	1	$3d^6 (^5D)$ 4s 4p ($^3P°$)	z $^3P°$	1	675.02	9.4e−22								
	Si II	3s 3p ($^3P°$) 4s	$^4P°$	5/2	3s 3p ($^3P°$) 4p	^4D	5/2	675.03	3.6e−36								
	N I	$2s^2 2p^2 (^3P)$ 3p	$^4P°$	3/2	$2s^2 2p^2 (^3P)$ 4d	^4P	5/2	675.20	4.3e−30								
	Fe I	$3d^6 (^5D)$ 4s 4p ($^1P°$)	y $^5P°$	1	$3d^6 (^5D)$ 4s (^4D) 5s	g ^5D	1	675.27	4.0e−23								
	Fe II	$3d^6 (^5D)$ 4d	^4P	3/2	$3d^6 (^5D_4)$ 4f	^{2}[3]°	5/2	675.72	1.0e−32					675.91	1.9e−22	675.88	4.0e−21
	N I	$2s^2 2p^2 (^3P)$ 3p	$^4P°$	5/2	$2s^2 2p^2 (^3P)$ 4d	^4P	3/2	675.92	4.2e−30								
	Ni I	$3d^{10}$	^1S	0	$3d^9 (^2D)$ 4p	$^3P°$	1	676.78	6.2e−22			676.78	1.2e−21	676.94	7.1e−22	677.00	1.1e−20
	N I	$2s^2 2p^2 (^3P)$ 3p	$^4P°$	5/2	$2s^2 2p^2 (^3P)$ 4d	^4P	5/2	676.96	9.9e−30								
	Fe II	$3d^6 (^5D)$ 5p	$^6F°$	7/2	$3d^6 (^5D)$ 5d	^6G	7/2	677.09	2.1e−32								
	Ni I	$3d^9 (^2D)$ 4p	$^3P°$	1	$3d^9 (^2D_{3/2})$ 5s	^{2}[3/2]	2	677.23	4.7e−23								
	Fe II	$3d^6 (^5D)$ 5p	$^4P°$	1/2	$3d^6 (^5D)$ 5d	^4P	3/2	677.72	6.0e−33							678.12	3.2e−21
	Mg II	$2p^6$ 5p	$^2P°$	1/2	$2p^6$ 7d	^2D	3/2	678.14	1.9e−32					678.72	1.0e−22		
	Fe I	$3d^7 (^4F)$ 4p	y $^5D°$	2	$3d^7 (^4F)$ 5s	e ^3F	3	678.69	2.3e−23							678.78	5.4e−21
	Mg II	$2p^6$ 5p	$^2P°$	3/2	$2p^6$ 7d	^2D	5/2	678.79	3.3e−32								
F26	N I	$2s^2 2p^2 (^3P)$ 3p	$^4P°$	5/2	$2s^2 2p^2 (^3P)$ 5s	^4P	5/2	694.52	2.5e−29			694.52	2.7e−21	694.52	1.5e−21	694.52	1.8e−20
	Fe I	$3d^6 4s^2$	a $^3P2$	1	$3d^6 (^5D)$ 4s 4p ($^3P°$)	z $^3P°$	2	694.52	1.4e−21								
	N I	$2s^2 2p^2 (^3P)$ 3p	$^4P°$	1/2	$2s^2 2p^2 (^3P)$ 5s	^4P	3/2	695.16	9.7e−30					695.17	4.9e−22	695.24	2.6e−20
	Fe II	$3d^6 (^5D)$ 5p	$^4F°$	5/2	$3d^6 (^5D)$ 5d	^4G	7/2	695.27	1.2e−31								
	N I	$2s^2 2p^2 (^3P)$ 3p	$^4P°$	3/2	$2s^2 2p^2 (^3P)$ 5s	^4P	3/2	696.05	4.4e−30					696.23	4.2e−22		
	Fe I	$3d^8$	c ^3F	2	$3d^6 (^3G)$ 4s 4p ($^3P°$)	v $^5F°$	3	696.30	1.2e−22								
	Fe II	$3d^6 (^5D)$ 5p	$^4D°$	3/2	$3d^6 (^5D)$ 5d	^4D	3/2	697.58	2.3e−32			697.87	5.0e−21	697.80	1.9e−21	697.84	7.9e−21
	Si I	$3s^2$ 3p 4p	^3D	1	$3s^2$ 3p 6d	$^3F°$	2	697.65	7.3e−24								
	Cr I	$3d^4 (^5D)$ 4s 4p ($^3P°$)	y $^7P°$	4	$3d^5 (^6S)$ 4d	e ^7D	5	697.84	1.2e−21								
	Fe I	$3d^6 4s^2$	a $^3P2$	0	$3d^6 (^5D)$ 4s 4p ($^3P°$)	z $^3P°$	1	697.89	1.1e−21								
	N I	$2s^2 2p^2 (^3P)$ 3p	$^4P°$	5/2	$2s^2 2p^2 (^3P)$ 5s	^4P	3/2	697.92	9.2e−30								
	Cr I	$3d^4 (^5D)$ 4s 4p ($^3P°$)	y $^7P°$	4	$3d^5 (^6S)$ 4d	e ^7D	4	697.98	3.3e−22								

Appendix B: Figures of the spectral features

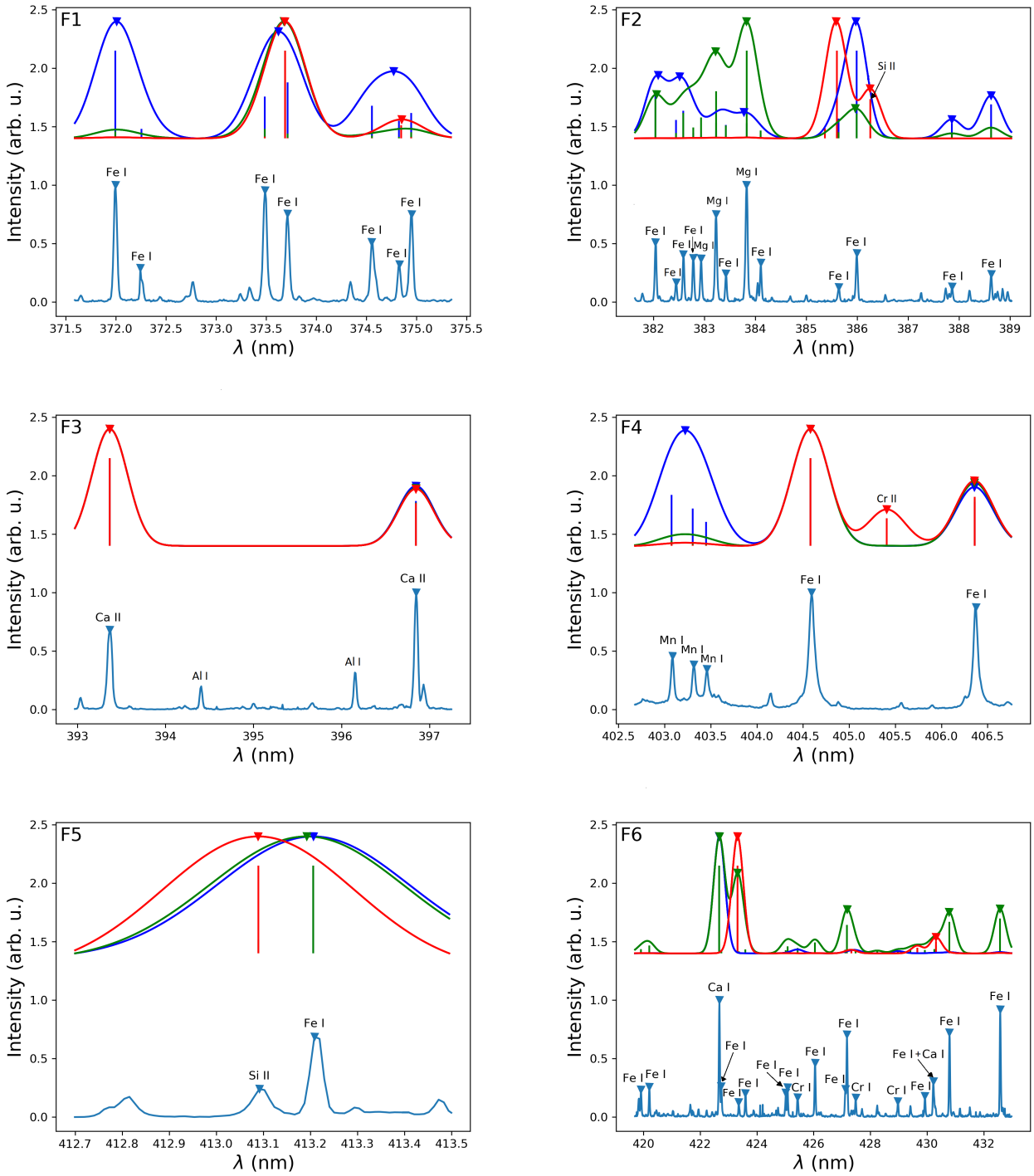

Fig. B.1. Spectral features F1–F6. *Upper part*: synthetic spectra calculated under different temperatures: blue shows 4000 K, green shows 7000 K, and red shows 10 000 K. The intensity of each of these spectra is scaled to 1. *Lower part*: high-resolution emission spectrum of the meteorite laser ablation plasma. Each marked peak is listed in Table A.1

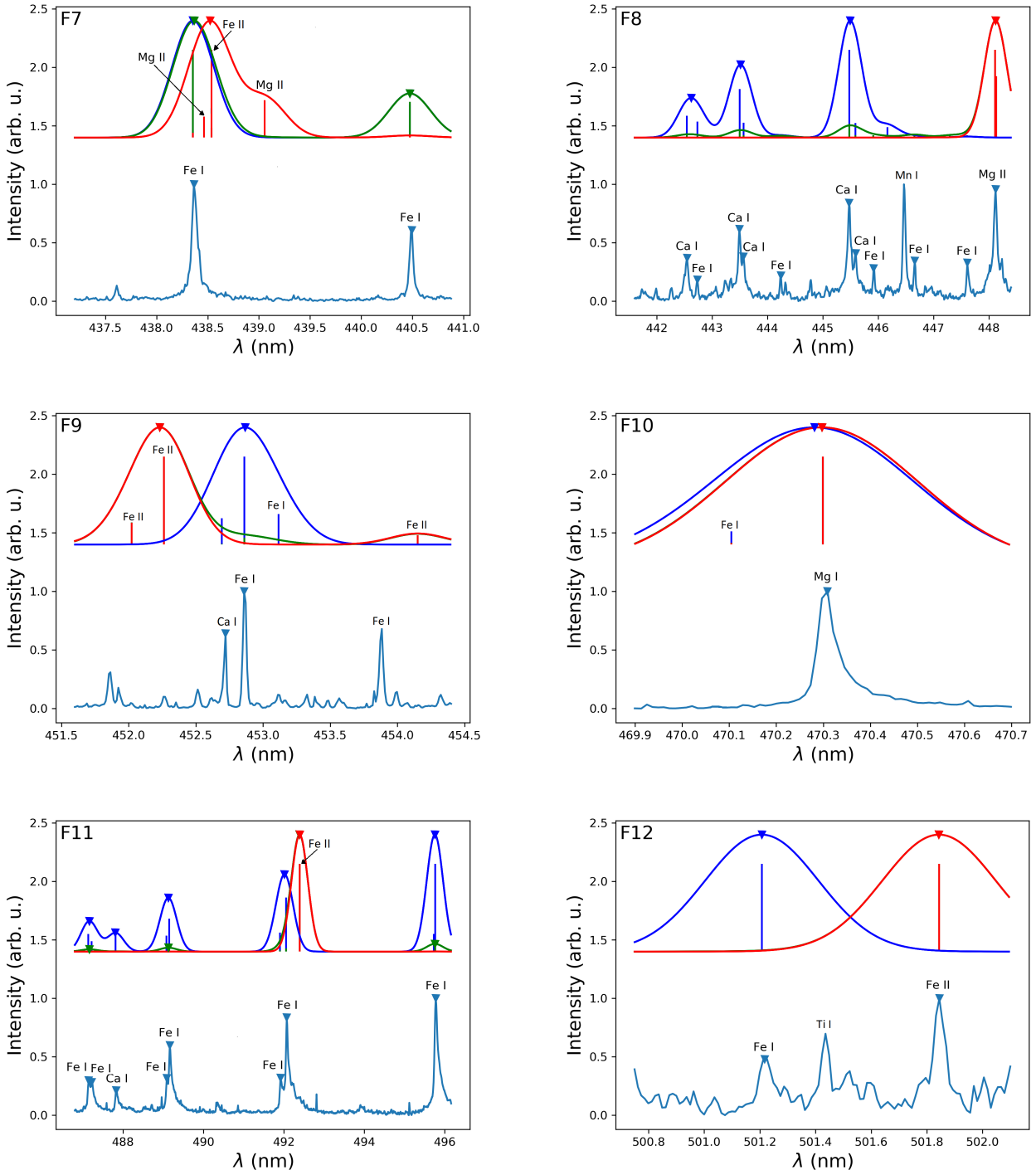

Fig. B.2. Spectral features F7–F12. *Upper part*: synthetic spectra calculated under different temperatures: blue shows 4000 K, green shows 7000 K, and red shows 10 000 K. The intensity of each of these spectra is scaled to 1. *Lower part*: high-resolution emission spectrum of the meteorite laser ablation plasma. Each marked peak is listed in Table A.1

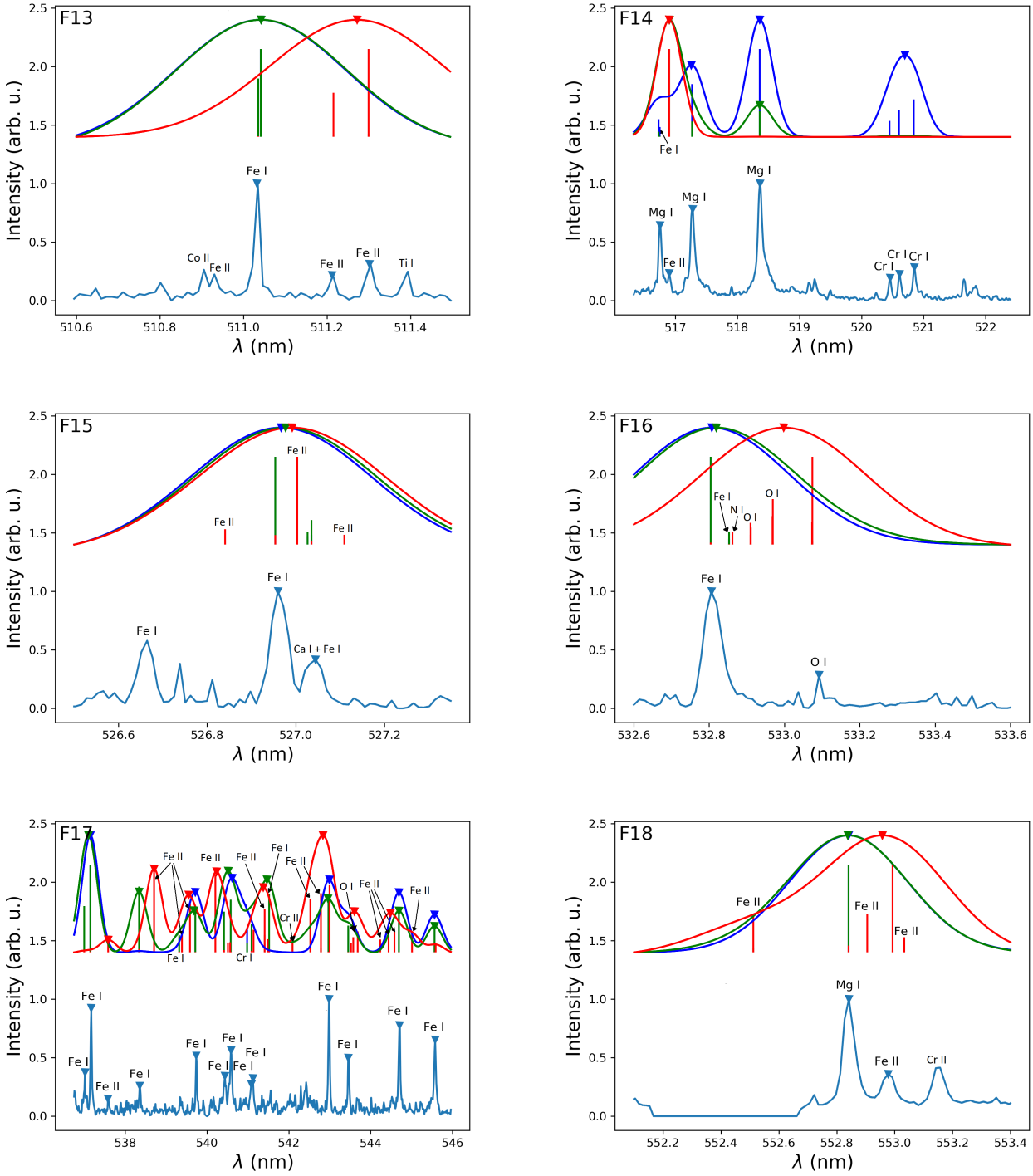

Fig. B.3. Spectral features F13–F18. *Upper part*: synthetic spectra calculated under different temperatures: blue shows 4000 K, green shows 7000 K, and red shows 10 000 K. The intensity of each of these spectra is scaled to 1. *Lower part*: high-resolution emission spectrum of the meteorite laser ablation plasma. Each marked peak is listed in Table A.1

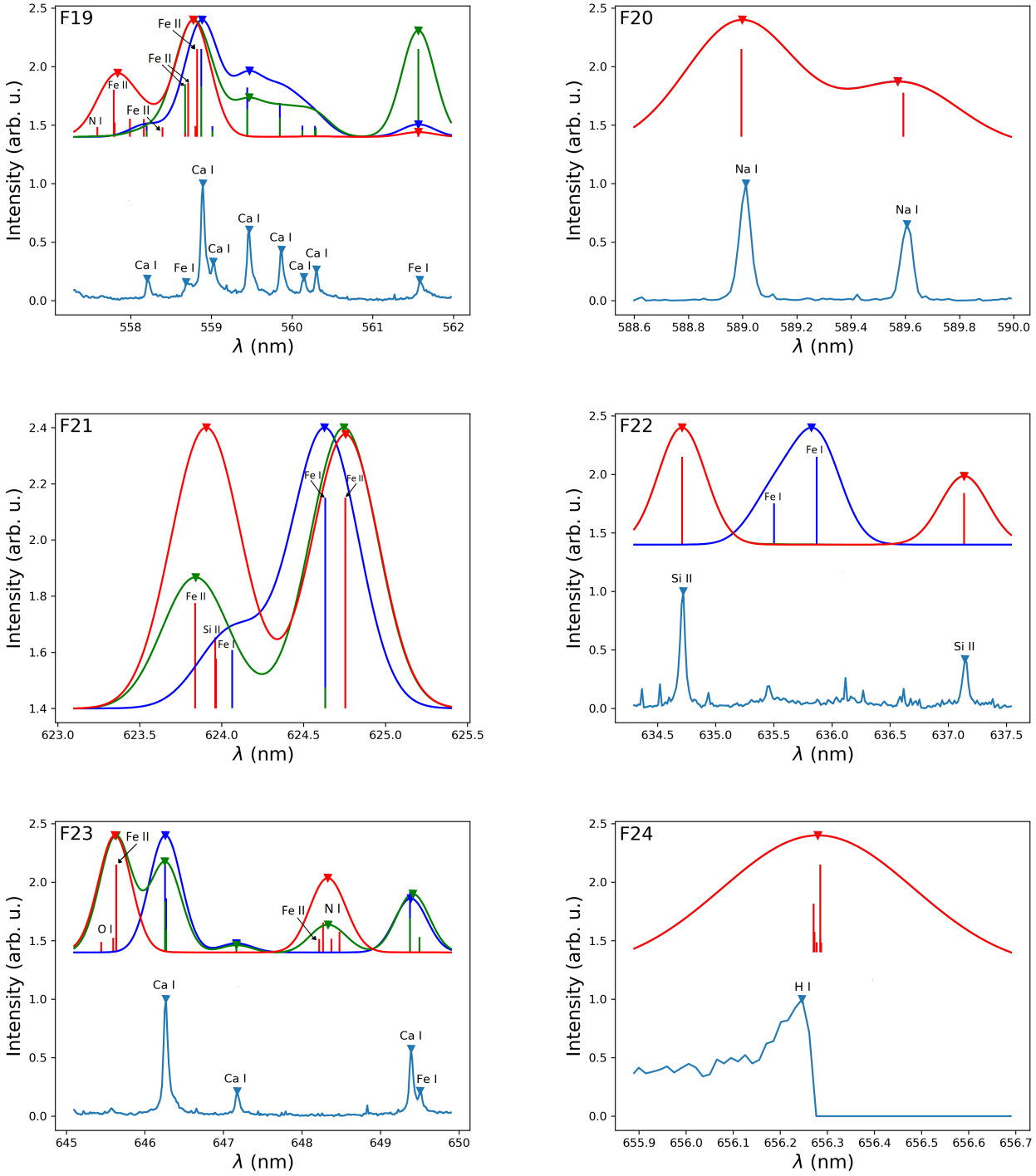

Fig. B.4. Spectral features F19–F24. *Upper part*: synthetic spectra calculated under different temperatures: blue shows 4000 K, green shows 7000 K, and red shows 10 000 K. The intensity of each of these spectra is scaled to 1. *Lower part*: high-resolution emission spectrum of the meteorite laser ablation plasma. Each marked peak is listed in Table A.1

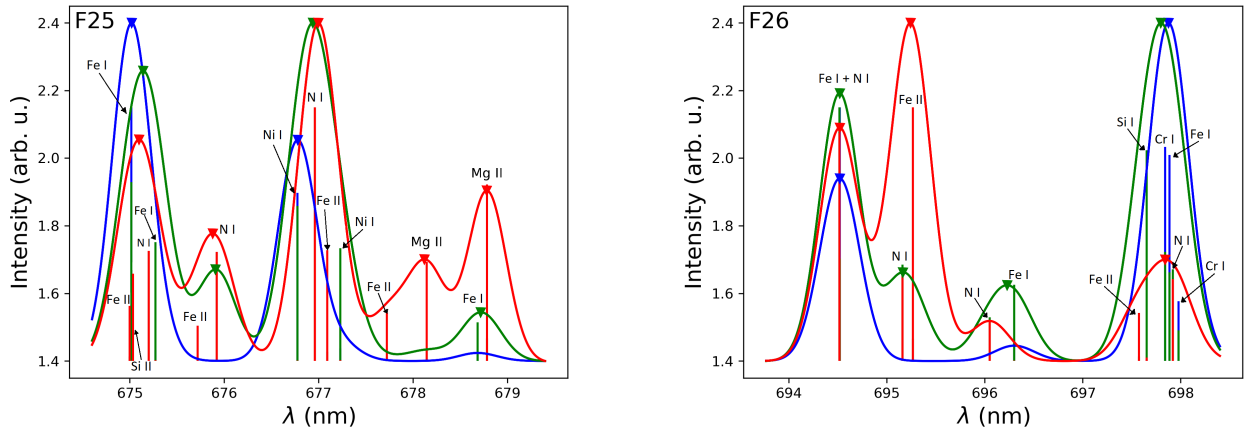

Fig. B.5. Spectral features F25–F26. *Upper part*: synthetic spectra calculated under different temperatures: blue shows 4000 K, green shows 7000 K, and red shows 10 000 K. The intensity of each of these spectra is scaled to 1. *Lower part*: high-resolution emission spectrum of the meteorite laser ablation plasma. Each marked peak is listed in Table A.1

Appendix C: Simulation spectra of chondrite meteorites

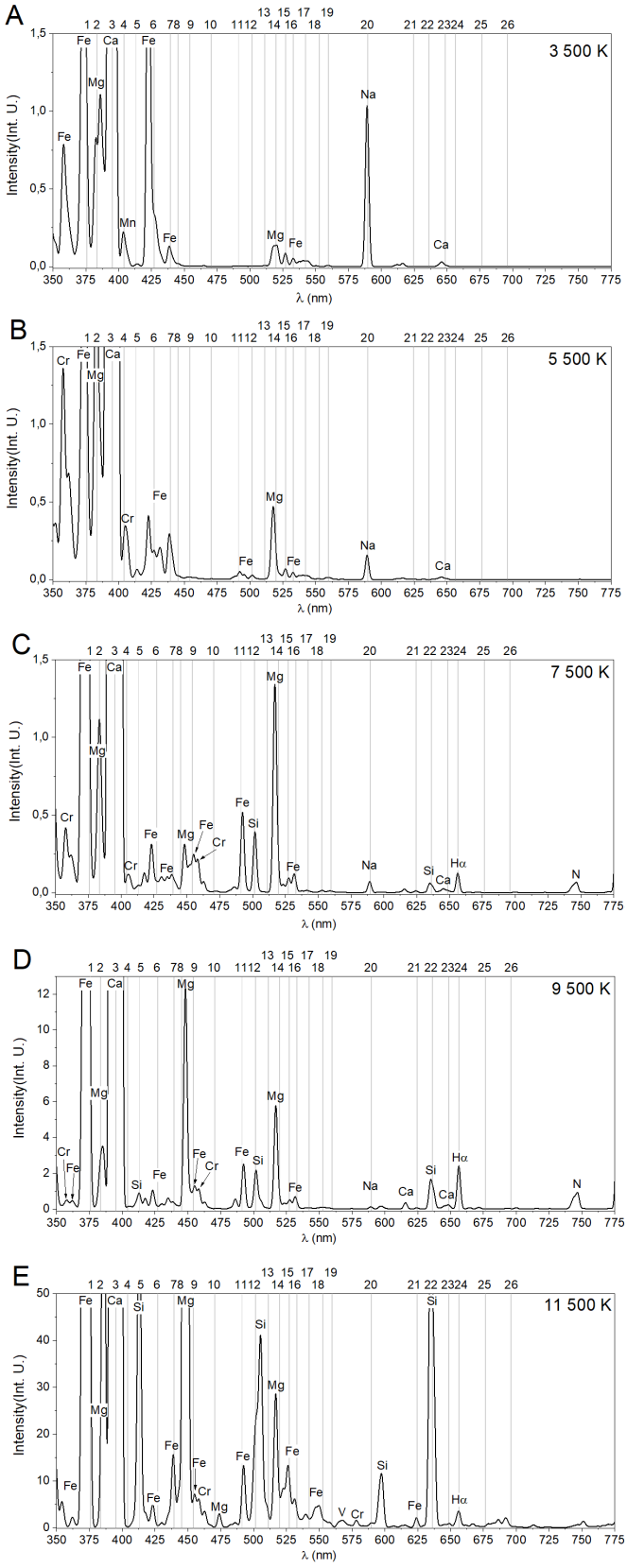

Fig. C.1. Low-resolution simulation spectra of chondrite meteorites for gradually increasing temperatures.